CHALMERS

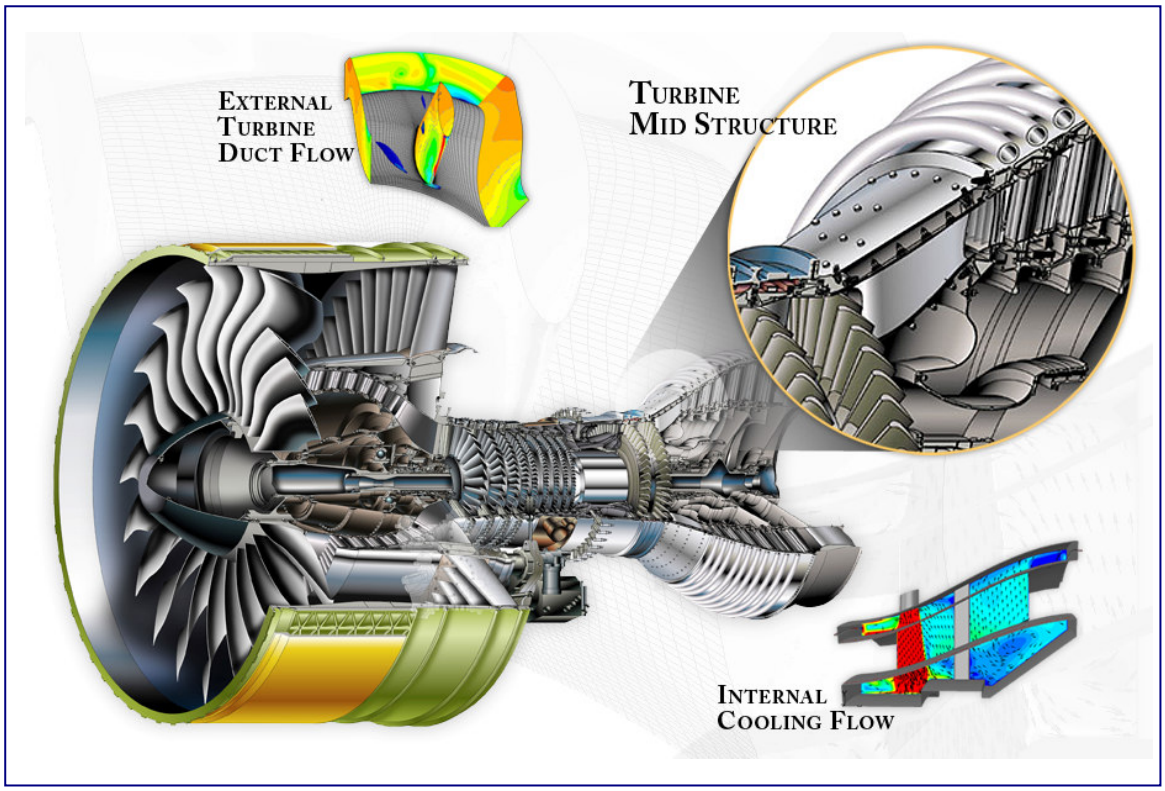

Heat Transfer In Turbine Mid Structures

International Master's programme in Computational and Experimental Turbulence

ABDALLAH ABOU-TAOUK MOHAMMAD EL-ALTI

Department of Applied Mechanics
Division of Fluid Mechanics
CHALMERS UNIVERSITY OF TECHNOLOGY
Gothenburg, Sweden 2006

Master's Thesis 2006:88

MASTER'S THESIS 2006:88

Heat Transfer In Turbine Mid Structures

Master's Thesis in the International Master's programme in Computational and Experimental Turbulence

ABDALLAH ABOU-TAOUK MOHAMMAD EL-ALTI

Department of Applied Mechanics
Division of Fluid Mechanics
CHALMERS UNIVERSITY OF TECHNOLOGY
Gothenburg, Sweden 2006

Heat Transfer In Turbine Mid Structures

Master's Thesis in the International Master's programme in Computational and Experimental Turbulence

Master's Thesis 2006:88
ISSN 1652-8557
Department of Applied Mechanics
Division of *Fluid Mechanics*
Chalmers University of Technology
SE-412 96 Gothenburg
Sweden
Telephone: + 46 (0)31-772 1000

Cover:
The picture on the front page is the GP7000 engine. The design of the picture is modified by Fadi Tobela.

Coor Print Service
Trollhättan, Sweden 2006

This master thesis work is performed at the department of Aerothermodynamics, 7161, at Volvo Aero Corporation in Trollhättan, Sweden. The supervisor at Volvo Aero is Dr. Hans Abrahamsson.

Heat Transfer In Turbine Mid Structures

Master's Thesis in the International Master's programme in Computational and Experimental Turbulence

ABDALLAH ABOU-TAOUK & MOHAMMAD EL-ALTI

Department of Applied Mechanics
Division of Fluid Mechanics
Chalmers University of Technology

ABSTRACT

In order to estimate the life time of a cooled gas turbine component, knowledge of the heat transfer is essential in order to predict the material temperature. Usually, a gas turbine has a hot turbine structure in between the high and low pressure turbines, which here is called the Turbine Mid Structure (TMS). The TMS has a complex design consisting of a hot aerodynamic and a cold load carrying structure. The TMS is usually cooled in order to limit the material temperature. To understand the heat transfer and to predict the material temperature in a TMS, a numerical study is performed. The FLUENT CFD tools are used to study the external gas path as well as the internal cooling flows. The CFD tools are validated to different fundamental heat transfer correlations. This numerical method is applied to the external turbine duct flow in both 2D and 3D analyses. For the internal cooling flow investigation, a simplified configuration is studied for different inlet conditions. In order to predict the wall temperature, a conjugated CFD model is built and compared to the thin shell conduction capability in FLUENT. In general, the predicted heat transfer for the external duct flow is in reasonable agreement with standard heat transfer correlations. The flow and heat transfer in the turbine duct is very complex and highly three dimensional with regions of separated flow. The internal cooling flow is also highly complex, governed by the feeding system, is non-uniform and shows a very strong coupling between the velocity field, air and metal temperatures. It is very demanding to build a conjugated CFD model and to model a realistic seal leakage. The preferred method to obtain the wall temperatures is the thin shell method with convective boundary conditions.

Key words: Heat Transfer, Computational Fluid Dynamics, Numerical Methods, Turbine Ducts and Turbine Mid Structure

Contents

Preface

This thesis work is performed as a Master's Thesis project in the International Master's programme in Computational and Experimental Turbulence (CEMAS).

The project is approved by the Department of Applied Mechanics, Division of Fluid Dynamics, Chalmers University of Technology, Sweden. The examiner at Chalmers is Associate Professor Gunnar Johansson.

The master thesis work was carried out at the department of Aerothermodynamics, 7161, at Volvo Aero Corporation in Trollhättan, Sweden. The supervisor at Volvo Aero is Hans Abrahamsson.

We would like to express our appreciation and gratitude to our supervisor Dr. Hans Abrahamsson for all the help and professionalism which we have received during the work. We also thank all the employees at the department of the Aerothermodynamics. Especial thanks to Dr. Lars Ljungkrona and Martin Nilsson for good guidelines during the work process.

Finally, it should be noted that the thesis work could never have been done without the help and encouragement from our wonderful families which always supported us and gave us love.

Trollhättan, November 2006

Abdallah Abou-Taouk & Mohammad El-Alti

Nomenclature

Latin Symbols

A	Area
C_p	Specific heat at constant pressure
D, d	Diameter
k	Turbulent kinetic energy
Nu	Nusselt number
P	Time-averaged pressure
P_k	Production term
Pr	Prandtl number
q_w	Surface heat flux
Re	Reynolds number
T	Time-averaged temperature
U_i	Time-averaged velocity in x_i-direction
y^+	Dimensionless distance from a wall

Greek Symbols

ε	Dissipation
λ, k	Conductivity
μ	Dynamic viscosity
μ_t	Dynamic turbulent viscosity
ρ	Density
σ_ε	Constant in the ε-equation
σ_k	Constant in the k-equation

Abbreviation

AITEB2	Aerothermal Investigations on Turbine Endwalls and Blades
AR	Area Ratio
BC	Boundary Condition
CTH	Chalmers Tekniska Högskola (Chalmers University of Technology)
HPT	High Pressure Turbine
HTC, h	Heat Transfer Coefficient
LPT	Low Pressure Turbine
LSLS	Large Scale Low Speed
TMS	Turbine Mid Structure

Subscript

w	Wall
s	Static
t	Total

Turbulence models

rke	Realizable k-ε model
rngke	ReNormalization Group k-ε model
RSM	Reynolds Stress Model
sa	Spalart-Allmaras
ske	Standard k-ε model
skw	Standard k-ω model
sstkw	Shear Stress Transport k-ω model

1 Introduction

The aim of this thesis work is to build up knowledge and experience about heat transfer in cooled turbine structures in order to predict wall temperatures.

The current turbofan engines needs to be improved to satisfy the conditions of higher efficiency due to today's demands. Turbofan engines usually contain different structures that transfer loads between different shafts and bearing to the outer case of the engine. The high pressure turbine (HPT) and the low pressure turbine (LPT) are connected by a structure that, in this thesis work, is called the Turbine Mid Structure (TMS). The TMS transfers loads between the high pressure turbine shaft and the outer shell of the engine. Usually a TMS consists of two parts, a load carrying cold structure and an aerodynamic hot gas flow structure. Since the gas path temperatures out of the HPT are high, the cold structure requires some cooling. This is done using the compressor air that is guided between the cold and the hot structure.

The current knowledge of the flow and heat transfer within the TMS is very limited. This is concluded from the literature study performed in the beginning of this thesis work. To be able to design the cooling system and estimate the life time of a TMS, a thorough understanding of the external hot gas flow, the internal cooling flow pattern and the coupled heat transfer rates is essential.

This thesis work starts with a literature study where a lot of papers and books concerning this subject are studied. The next task is to validate the CFD method to some basic heat transfer correlations that are connected to the TMS flow pattern. Further, the work is split up into an external duct flow and an internal cooling flow analysis. The external part considers the AITEB2[1]-duct geometry, which is a fluid flow optimized duct developed at Chalmers University of Technology and Volvo Aero Corporation. The external part includes turbulence model and mesh sensitivity studies, fluid flow and heat transfer analysis. The internal part concerns analysis of cooling flow within the TMS. It includes building up a simplified configuration, mesh sensitivity studies and investigation for different inlet feed conditions. The final step in this thesis work is to build up a conjugated model where internal and external parts are coupled together. Since the conjugated model showed complexity and some difficulties, an internal model with thin shell conduction and convective boundary conditions is implemented.

Chapter 2 deals with basic theory required in this work followed by some basic case studies presented in chapter 3. The main work performed is presented in chapter 4, 5 and 6 and deal with external duct, internal cooling flow and the conjugated model respectively. Appendix A contains extended theory part, Appendix B includes the validation cases and Appendix C complements the 3D cases considered in the thesis, e.g. external duct flow in real conditions and the mesh sensitivity study of the internal cooling model.

---

[1] Aerothermal Investigations on Turbine Endwalls and Blades. This is a FP6 European project.

This thesis work is split up according to the scheme shown in Figure 1:

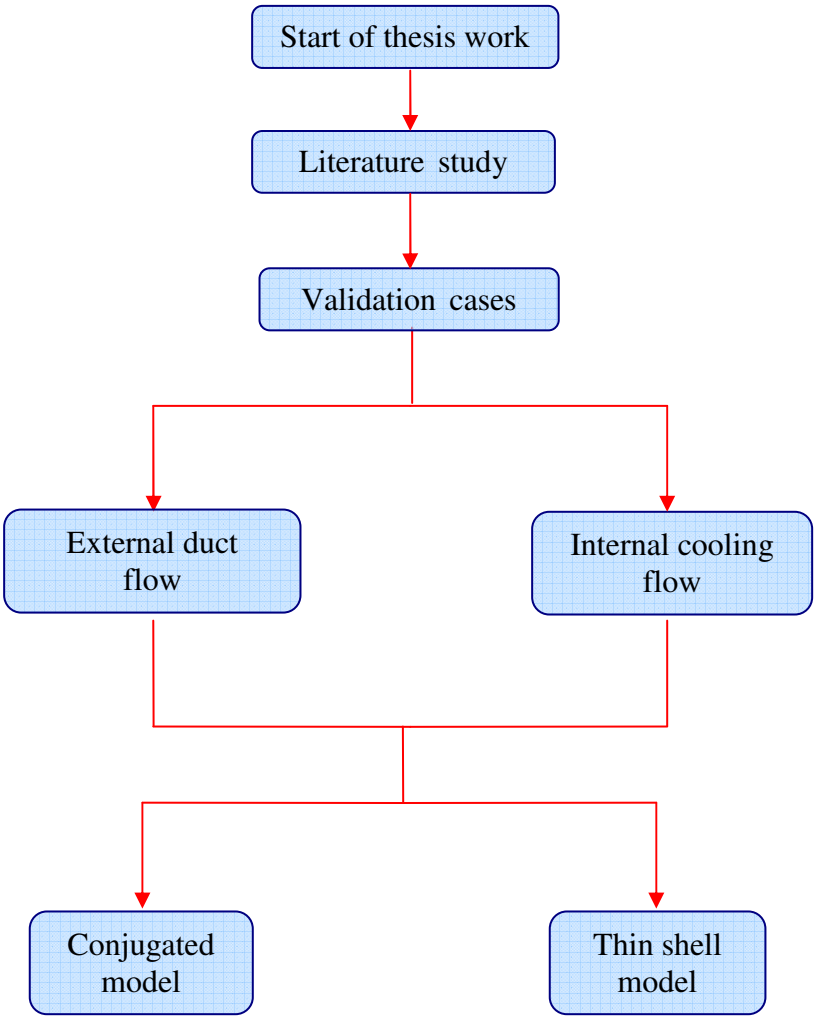

Figure 1: Working scheme.

The investigation of the external duct flow and the conjugated model is performed by Abdallah Abou-Taouk. The internal cooling part followed by the thin shell model is performed by Mohammad El-Alti.

The CFD-code which is used in this project is FLUENT (v6.2.16) and the meshing software is both Gambit (v2.2.30) and ICEM (v10.0.0). The choice of the code is due to our previous experience and due to its simplicity.

Several restrictions are made in order to focus on essential issues. All calculations are considered in steady state conditions. The work is not aimed to optimize any geometry or other parameter. This work is only an investigation of the heat transfer and the fluid flow of already optimized geometry. Considering the meshing studies, all boundaries are not resolved.

2 Theory

The physics of fluid flow is governed by the Navier-Stokes equations. These are further discretized to be solved computationally. The computational fluid dynamics (CFD) is an iterative simulation method to solve fluid flow and heat transfer problems. This section includes the governing equations for fluid flow and heat transfer. The most used turbulence model in this thesis work is also described below.

2.1 Governing equations

For steady incompressible 3D fluid flow motion, where the Reynolds decomposition and Boussinesq hypothesis are applied, the continuity and momentum equations in tensor notation read

$$\frac{\partial}{\partial x_i}\left(\rho U_i\right) = 0$$

$$\frac{\partial}{\partial x_j}\left(\rho U_i U_j\right) = -\frac{\partial P}{\partial x_i} + \frac{\partial}{\partial x_j}\left[\left(\mu_t + \mu\right)\frac{\partial U_i}{\partial x_j}\right]$$

These equations are explained and derived in Appendix A1.1 and A1.2.

2.2 Turbulence modeling

To be able to solve turbulent flows, Reynolds averaging is applied to divide the motion in an average part and in a fluctuating part. The well known closure problem arises and thus the Reynolds stresses have to be modelled in order to close the systems of equations. The turbulence model which has been mostly used is the realizable k-ε model. The motivation for the choice, derivation and further details can be found in Appendix A3. The k-ε model reads

$$\frac{\partial}{\partial x_j}\left(\rho k U_j\right) = \frac{\partial}{\partial x_j}\left[\left(\frac{\mu_t}{\sigma_k} + \mu\right)\frac{\partial k}{\partial x_j}\right] + P_k - \rho\epsilon$$

$$\frac{\partial}{\partial x_j}\left(\rho \epsilon U_j\right) = \frac{\partial}{\partial x_j}\left[\left(\frac{\mu_t}{\sigma_\epsilon} + \mu\right)\frac{\partial \epsilon}{\partial x_j}\right] + \frac{\epsilon}{k}\left(c_1 P_k - c_2 \rho\epsilon\right)$$

2.3 Heat transfer

To be able to solve the temperature field or other heat transfer related quantities, the energy equation has to be solved together with the continuity and momentum equations. The energy equation reads

$$\frac{\partial}{\partial x_j}\left(TU_j\right) = \left(\frac{k}{\rho C_p}\right)\frac{\partial}{\partial x_j}\left[\frac{\partial T}{\partial x_j}\right]$$

Often, the heat transfer results (q_w) are presented in a non-dimensional way, the Nusselt (Nu) number, which reads

$$Nu = \frac{hD}{\lambda} = \frac{q_w D}{\lambda \Delta T}$$

where q_w is the surface heat flux, D is a characteristic length depending on the considered case, λ is heat conductivity and ΔT is the temperature difference between the fluid and the wall considered. Further detailed heat transfer theory is included in Appendix A5

2.4 Numerical method and meshing strategy

A commercial finite volume code, FLUENT (v6.2.16), is used throughout the work. The pressure-based implicit segregated solver is used with the implemented k-ε realizable turbulence model. The gradients are node-based calculated. The numerical scheme is second order upwind and almost all under-relaxation factors are set non-conservative. The residuals are set to 10^{-4}. More details are included in Appendix A4.

The meshing software used are both GAMBIT (v2.2.3) and ICEM CFD (v10.0.0). The former one is used for the internal cooling and the conjugated model, the later one for the external model. The choice of GAMBIT meshing software is due to the flexibility of building up a mesh which contains a mix of structured hexa-mesh and unstructured tetra-mesh. Regarding volume meshing, GAMBIT offers a semi-structured approach using the Cooper tool in which an unstructured quad mesh could be swept into a semi structured hexa mesh. In order to reduce the number of cells and minimize the discretization errors a hexa-mesh is preferred. To obtain that, the volume is carefully split into smaller volumes and meshed with hex-cells. Some faces were pre-meshed with an unstructured quad-mesh and coopered. However for the volumes which cannot be either mapped or coopered, tetra-meshes are used. This is explained in Figure 2 below.

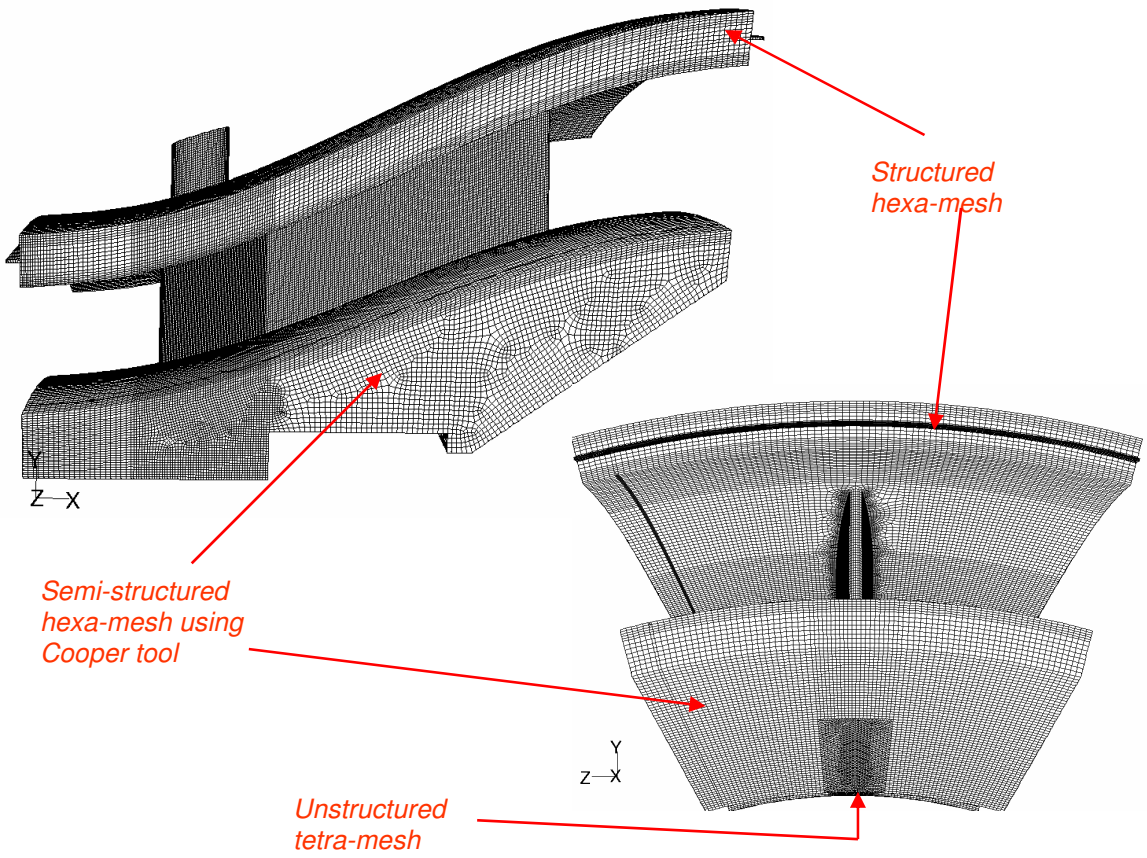

Figure 2: Mesh generated in GAMBIT using the Cooper tool.

Typical dimensions and approximate boundary conditions (BCs) for the TMS used in this work are presented in Table 1 below.

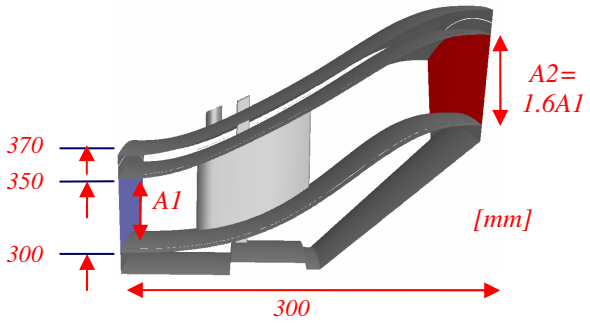

BC	Magnitude ≈
Pressure	6 bar
T-cold structure	900 K
T-hot structure	1200 K
Cooling flow	700 K
dm/dt cooling	0.3-2 % of gas path
dm/dt gas path	90 kg/s

Table 1: Typical dimensions (left) and BC (right) used in this work.

The mass flow rate of the gas path is based on the compressible equations found in Appendix A2.

3 Validation

The literature study did not identify any good test cases for the turbine duct heat transfer. Due to this, the numerical CFD method is validated to some basic test cases such as; flat plate, pipe flow and diffusers. The objective of the validation study is to choose a numerical method for the following TMS analysis and to get an estimate for the resultant accuracy.

3.1 Flat plate

A thermal boundary layer is obtained when the wall and the free stream temperature differs in magnitude and this creates a heat transfer from or to the wall. The considered flat plate has a length of 1.25[m] and the size of the domain is 1.5[m]*0.35[m]. The inlet is placed 0.25[m] in front of the flat plate where the inlet BCs are $P_{tot}\approx6$[bar] and V≈100[m/s]. The BC for the flat plate is set to a wall with a constant temperature of 1200[K] and the outlet is set to a pressure outlet BC with a static pressure of 5.9[bar]. The rest of the walls are set to symmetry BC. The fluid is set to air with a temperature of T_{tot} ≈1300[K].

To obtain low y^+ values, a well resolved boundary layer mesh along the flat plate is used. The y^+ values for the flat plate ended up with a value below 0.5, which gives rise to a mesh of 18000 cells. The results can be found in Appendix B1. The conclusion made for the flat plate case is that the prediction of the Nu number is in agreement with the correlations 7.37 and the proposed one by Petukhov, which can be found in Appendix A5, Table 1.

3.2 Pipe flow

The second validation case is a straight annular duct. The length of the duct is 5[m] (L/D_h=100). The length is chosen to be long since a fully developed flow is desirable since most of the correlations are developed for fully developed flow. The inlet BCs are set to $P_{tot}\approx6$[bar], Ma≈0.6 and V≈200[m/s]. The BC for the duct walls is set to a wall with a constant temperature of 1200[K]. Outlet is set to a pressure outlet BC and the fluid is set to air with a temperature of $T_{tot}\approx1300$[K].

The y^+ values are below 0.3 and the mesh reached about 12 000 cells. A comparison of different correlations together with the CFD result is presented in Table 2. The correlations stated in the table are presented in Appendix A5. One can observe that the correlations yield a similar average Nu number. The maximum difference between the correlations is around 10%, which is quite acceptable since the correlations are based on different parameters. The CFD results (rke-model) gives a slightly lower value of the Nu number than the standard heat transfer correlations. For more results and settings, see Appendix B2.

Correlations	Nu number (Fully developed)
Colburn [8.59]	971
Dittus Boelter [8.60]	981
Petukhov [8.62]	860
[8.63]	925
CFD–results	835

Table 2: The average Nu number for different correlations.

3.3 Diffusers

The third validation case considered is diffusers. First a mesh dependence check is done which ended up with a mesh of about 11 000 nodes with resolved boundary layers and y^+ below 1. Then several design parameters are investigated in order to study the influence on the heat transfer (Nu number). The dependence on boundary layer thickness is checked through varying the inlet channel prior to the diffuser wall. The boundary layer thickness varied between 10-32% of the inlet duct height. Further the dependence of area ratio (AR) or the diffuser angle is checked and finally the dependence on different turbulence models is investigated.

The BCs are constant throughout the case work. The mass flow rate is 58[kg/s] and the temperature of the walls considered is set to 1200[K]. The outlet static pressure is varied in order to achieve a constant inlet total pressure of 6[bar].

There is a reasonable agreement, with a difference of about 10-20%, in the prediction of heat transfer by different turbulence models. This is shown by the turbulence dependence check in the Appendix B3. The heat transfer on the diffuser wall is lower when the boundary layer thickness is increased, which is expected. The heat transfer is increased when the AR is increased. These results are presented in Appendix B3.

3.4 Conclusion of validation cases

The overall conclusion from the above validation cases is that the chosen CFD method (Fluent, rke) predicts the heat transfer within 10-20 % of the standard heat transfer correlations.

4 Turbine Mid Structures - External Part

4.1 Introduction

TMS is an important structural component since it connects the high pressure turbine (HPT) and the low-pressure turbine (LPT) in a gas engine, were the LPT has a larger radius than the HPT. The flow in a turbine duct is very complex since the flow is unsteady, highly turbulent and strong secondary flows arise. The TMS has often structural vanes passing through them, which usually are unloaded, meaning that they don't perform any aerodynamic turning to the flow. Figure 3 shows the different parts that are included in a TMS. Periodic BCs have been considered and the benefit it is that the calculations are performed only at one sector, which implies an enormous reduction of CPU time and complexity.

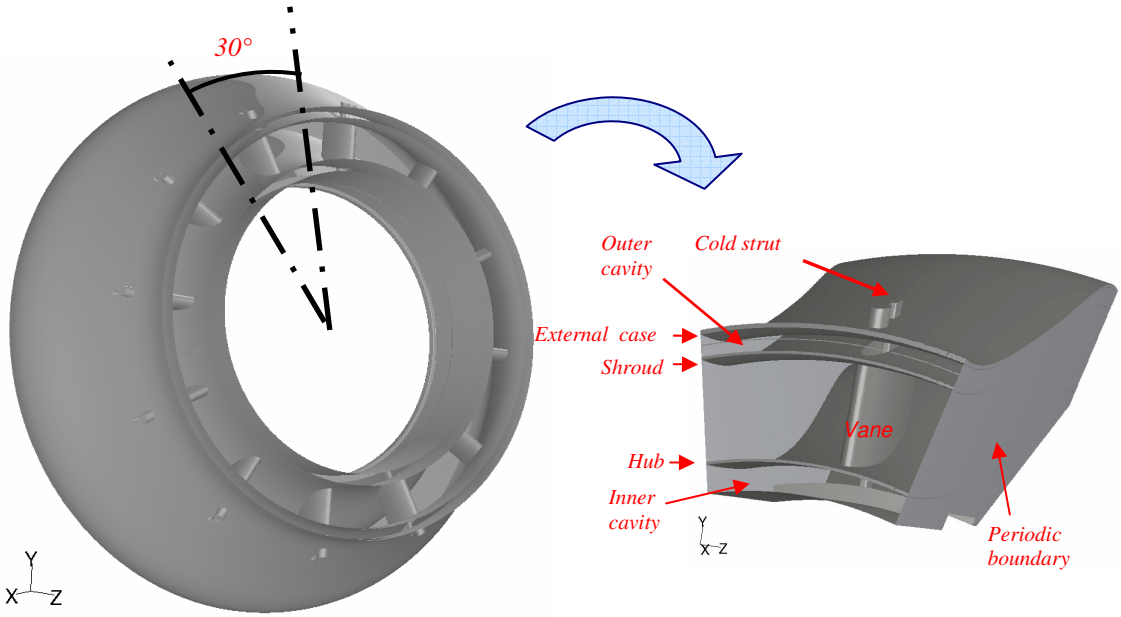

Figure 3: Full scale TMS to the left and one sector of the TMS to the right.

4.2 Analysis of the 2D-AITEB2-duct

Along the hub surface, the velocity of the flow first decelerates close to the inlet and then accelerates close to the outlet due to curvature effects. A similar behaviour is found for the shroud where the acceleration of the flow occurs close to the inlet and deceleration close to the outlet. The regions where the adverse pressure gradient is large are those where the risk for separation is highest. These regions, which can be observed from the computed results, represent the first curvature for the hub and the second curvature for the shroud.

Two different types of calculations are done for the 2D-duct. The first represents the "low speed" duct that is used in the AITEB2 project at Chalmers University. This is a Large

Scale Low Speed (LSLS) facility for intermediate turbine ducts. The second case represents high speed "real" conditions in an engine. Only the settings and the result from the "low speed" AITEB2 duct is presented below. The other results can be found in Appendix B4.2.

4.2.1 Geometry and mesh

The geometry used in the 2D-turbine duct analysis is presented in Figure 4. The geometry is a 2D optimized duct similar to the 3D AITEB2 duct. The 2D-turbine ducts cases do not include any blockage effects due to vanes.

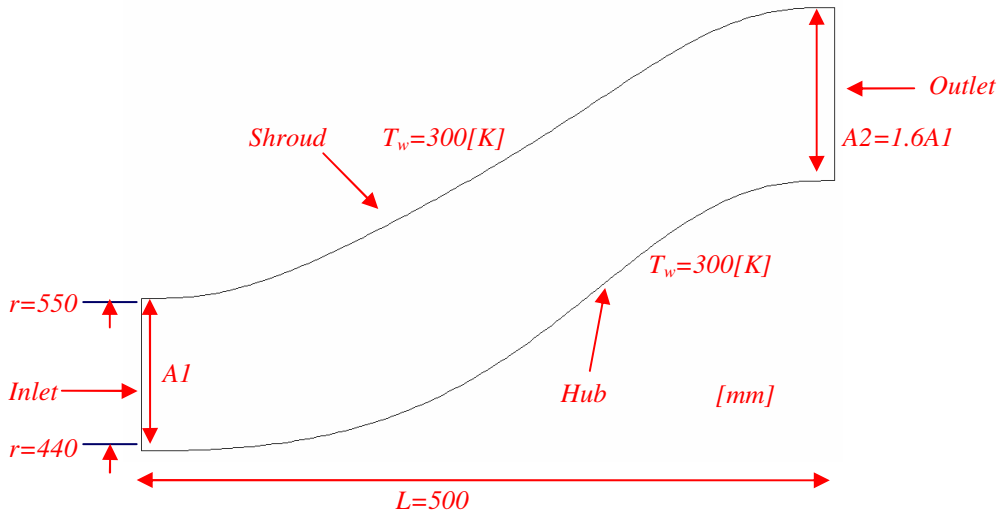

Figure 4: The duct geometry.

The resolved mesh contains around 24000 cells, where the shroud and the hub walls are well resolved. The skewness ended up with a value below 0.48. The sizing function near the wall consists of 20 rows, a grow factor of 1.35 and the first node is placed at a value of 0.01[mm]. This yielded y^+ values below 1.

4.2.2 Boundary conditions

Predefined inlet profiles for the swirl, temperature and total pressure are used as BCs, see Appendix B4.1. For the outlet BC, a profile for the static pressure is used. The 2D-duct case are solved by the 2D-axisymmetric solver with swirl in FLUENT. The remaining BC can be seen in Figure 4.

4.2.3 Results and discussion

Contours and profiles of the static pressure are shown in Figure 5. As mentioned earlier, the regions with adverse pressure gradient are along the first curvature for the hub and the second curvature for the shroud. It's obvious that the risk for separation is close to these regions.

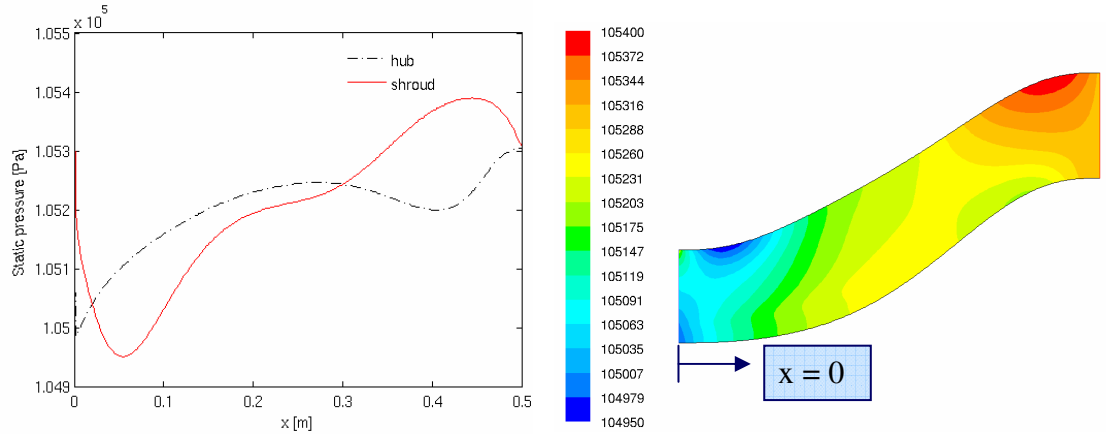

Figure 5: Left: Static pressure profiles. Right: Contour plot of the static pressure [Pa].

Figure 6 shows the comparison between the CFD-results and the turbulent plate heat transfer correlation, which are in good agreement. The correlation predicts the heat transfer coefficient (HTC) poorly only close to the inlet. The explanation of this is probably due to the inlet BC, since a swirl profile that corresponds to the 3D turbine duct is used for the 2D case. There is also a velocity magnitude plot in Figure 6. It's clear that the velocity increases close to the inlet and decreases close to the outlet along the shroud due to the curvature effects. The similar behaviour is for the hub but with opposite events. This is of course the reason why the pressure changes in these regions since the pressure and velocity are strong connected with each other.

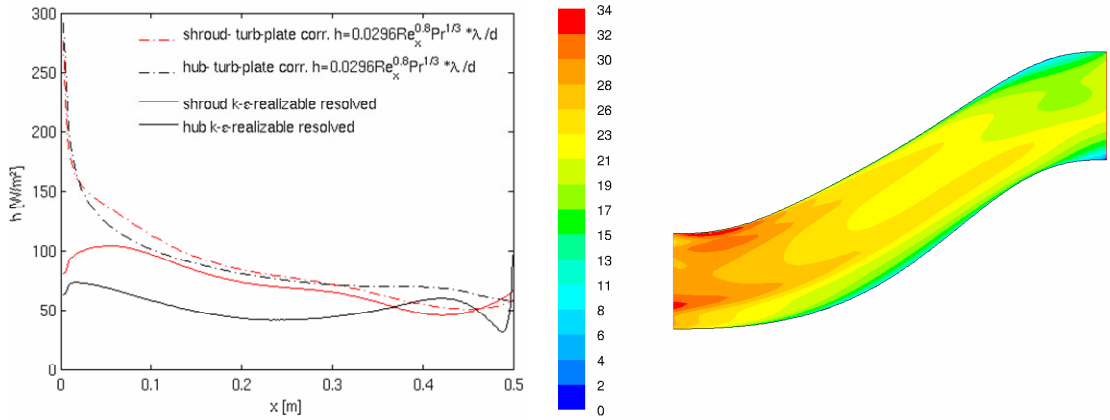

Figure 6: Left: HTC for the hub & shroud. Right: Contour plot of the velocity magnitude [m/s].

4.3 Analysis of the 3D-AITEB2-duct

Two different types of calculations are done for the 3D-turbine duct. The first one represents the "low speed" duct which is used in the AITEB2 project. The second one represents a typical "high speed" real engine condition. The settings and the result from the "low speed" AITEB2 duct is going to be presented below. The second one can be found in Appendix C1.2.

4.3.1 Geometry

The geometrical configuration is similar to the 2D duct. The 3D-duct cases are investigated with 9 vanes included. Since periodic BC is used the calculations are performed only in one sector which represents 40 degrees of the duct and one vane.

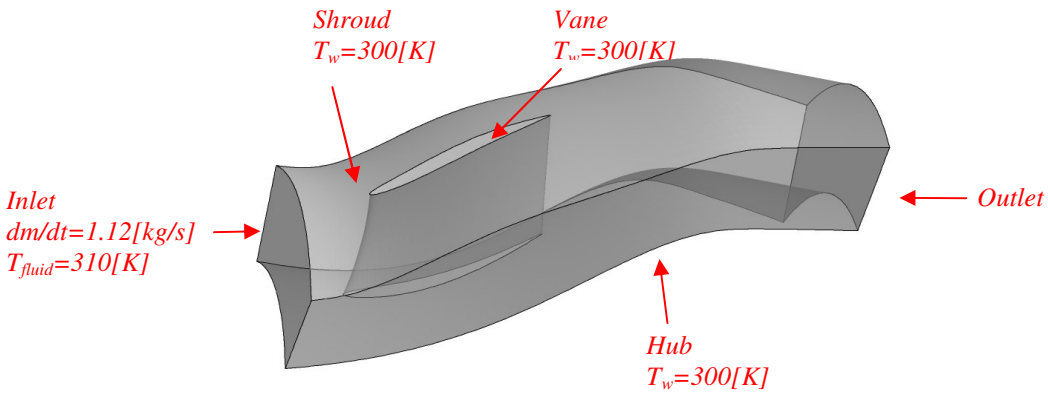

Figure 7: The 3D duct geometry.

4.3.2 Boundary conditions and mesh

Inlet profiles for the swirl, temperature and total pressure are used as BCs, see Appendix B4.1. To satisfy the mass flow condition an iterative process is done for the static pressure at the outlet to achieve the correct mass flow through the duct. The hex mesh is generated in ICEM CFD and contains around 1.300.000 cells and is found in Figure 8. One can observe that the cells are tighter close to the vane and thinner out towards the periodic faces. The minimum angle of the cells is above 25° and the determinant, which is a quality parameter that measures the deformation of a cell, is above 0.6 [9]. The y^+ values are between 10 and 50 which require the use of wall functions.

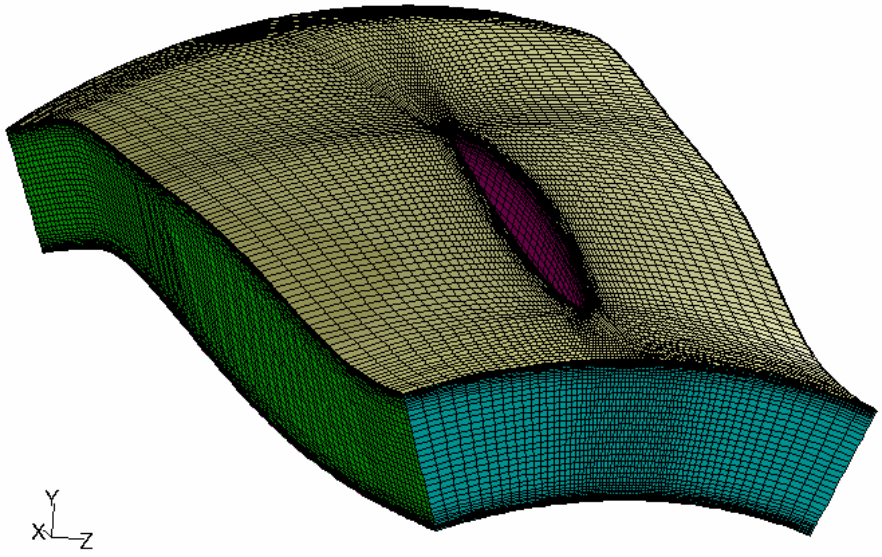

Figure 8: The hex-mesh used for the 3D-AITEB2 duct.

4.3.3 Results and discussion

The HTC

Contour plots and profiles of the HTC along the hub and shroud are shown in Figure 9. The maximum value of the HTC along the hub is at the trailing edge. The reason why the HTC is so high behind the vane is due to the creation of a big vortex, which is initialized from the vane. The vortex gets bigger behind the vane and hits the hub and gives rise to higher HTC, see Figure 10. The remarkable issue is that the shroud has low HTC where the hub has its biggest one. One can also observe that the HTC on the shroud is equally smoothly widespread while for the hub it varies locally.

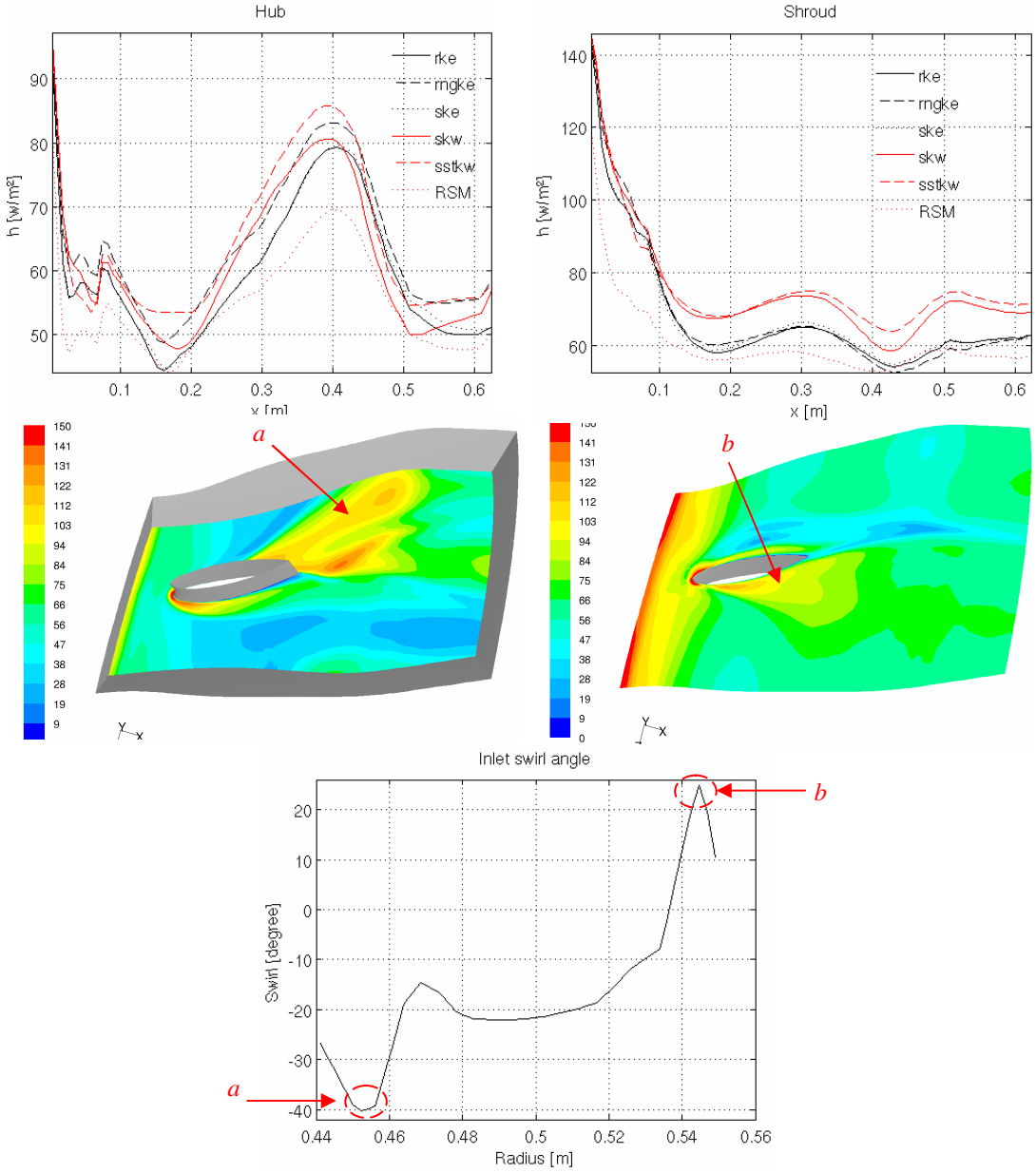

Figure 9: Circumferential averaged and contours of HTC [W/m^{2}K] for the hub and shroud.

Figure 9 shows also the average HTC at different axial positions obtain with different turbulence models. The turbulence models show quite good agreement except the RSM model. The average HTC is relatively constant for the shroud surface and is higher close to the inlet. It results in a value of around 60-70[W/m^{2}K]. For the hub surface, one has more variation of the average HTC due to the above mentioned vortex. The value is around 50-80[W/m^{2}K]. The high values of HTC close to the inlet are due to absence of a thermal boundary layer.

The vane is designed for a constant swirl profile of -17° whereas the used profile is a radial varying one. Therefore the high heat transfer region, marked "a" in the above figure, appears due to the low swirl angle (-40°). The second high region, marked "b" appears due the positive swirl angle (≈20°). Since the flow is swirled, it must accelerate along the leading edge of the vane and hence the creation of a pressure gradient.

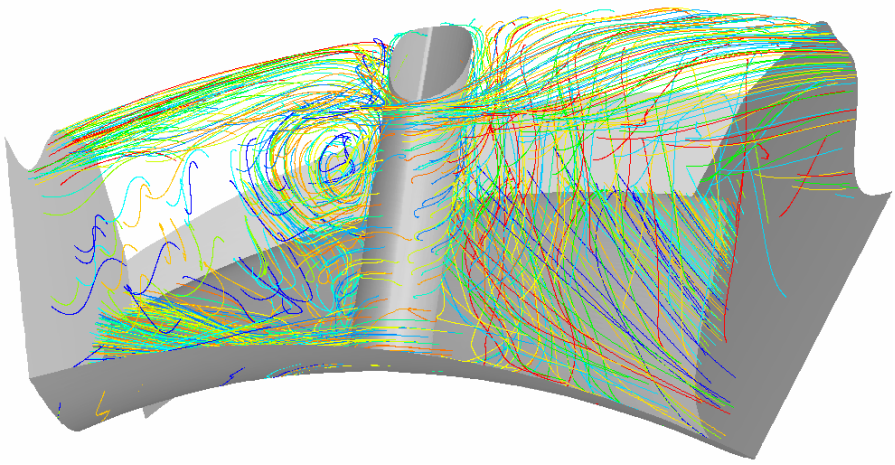

Figure 10: Pathlines showing the vortex to the left of the vane.

Contour plots of the HTC along the suction- and pressure side of the vane are shown in Figure 11. One big difference in the HTC for the two sides is in the middle region, close to the back of the vane, marked "a" in Figure 11. The suction side has very low HTC in this region. This is actually the same area where we have a region of negative axial velocities, see Figure 12. One can also observe that the highest HTC occurs in the leading edge region. This is obvious since one have a stagnation point region along the leading edge and zero axial velocities which consequently lead to the highest HTC.

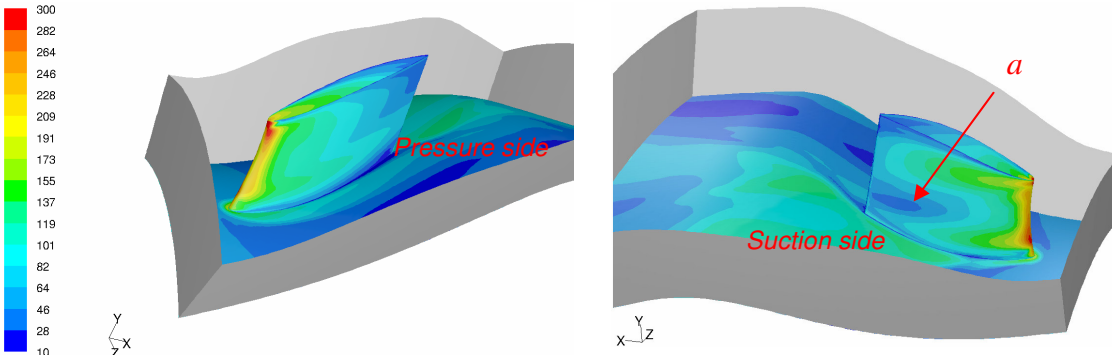

Figure 11: HTC [W/m^{2}K] along the pressure and suction side of the vane.

Static and total pressure

Figure 12 shows a contour plot of the total pressure on the outlet, the static pressure along the vane, the periodic surfaces and finally the iso-surfaces with negative axial velocities. The Figure shows a couple of interesting regions. Firstly, one can see regions, so called iso-surfaces, with negative axial velocities. It's absolutely a disadvantage to have these regions since they increase the pressure losses through the duct and therefore decreases the performance of a gas turbine engine. They also make the flow field very complex and increase the demands on the structures since they gives rise to higher HTC. Secondly, one can see that the total pressure increases in the axial direction. Of course the static pressure decreases due to e.g. friction, but since the AR increases along the duct, the overall picture of the static pressure increases.

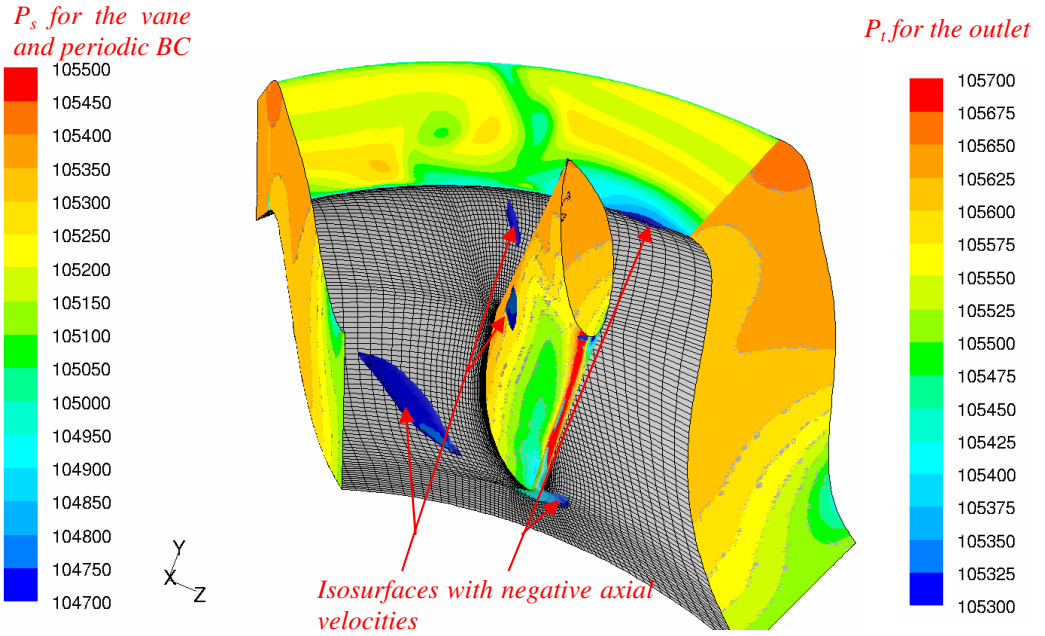

Figure 12: Static pressure along the vane, total pressure along the periodic faces and outlet [Pa].

Contours of the static pressure and its profiles along the hub and shroud are shown in Figure 13. Considering the hub, the static pressure increases slightly to the axial position 0.3[m], this follows by a decrease and finally an increase close to the outlet. The explanation of this behaviour is due to the curvature effects which give rise to acceleration and retardation of the flow and consequently changing the pressure field. Considering the shroud, the static pressure profile is similar as for the hub despite the front of the vane. Here the static pressure begins with a decrease until axial position 0.05[m] and is followed by a similar behaviour as for the hub. The interesting conclusion from these contour plots is that the static pressure distribution is very similar if one considers the radial direction. This means that the similar results are obtained for the 2D and 3D cases if similar radial pressure distribution is used.

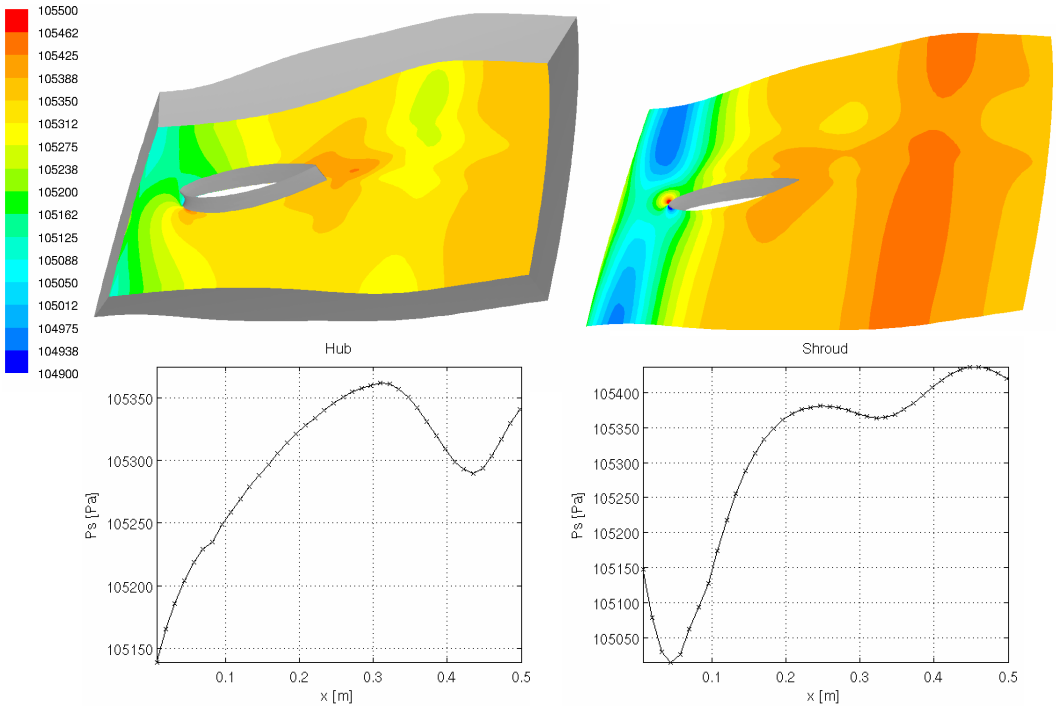

Figure 13: Static pressure profiles and contours plot of the hub (left) and shroud (right) [Pa].

Velocity magnitude

The last interesting result in this section is presented in Figure 14. It shows contour plot of the total pressure and the velocity magnitude vectors in five different planes, i.e. the axial positions 0.05[m], 0.15[m], 0.25[m], 0.35[m] and 0.45[m]. The big vortex mentioned earlier in this section is clearly visible behind the vane to the left. The vortex seems to increase in size downstream. The pressure and velocity fields are tightly coupled together as mentioned earlier. One can observe that regions of low total pressure occur close to the vortex.

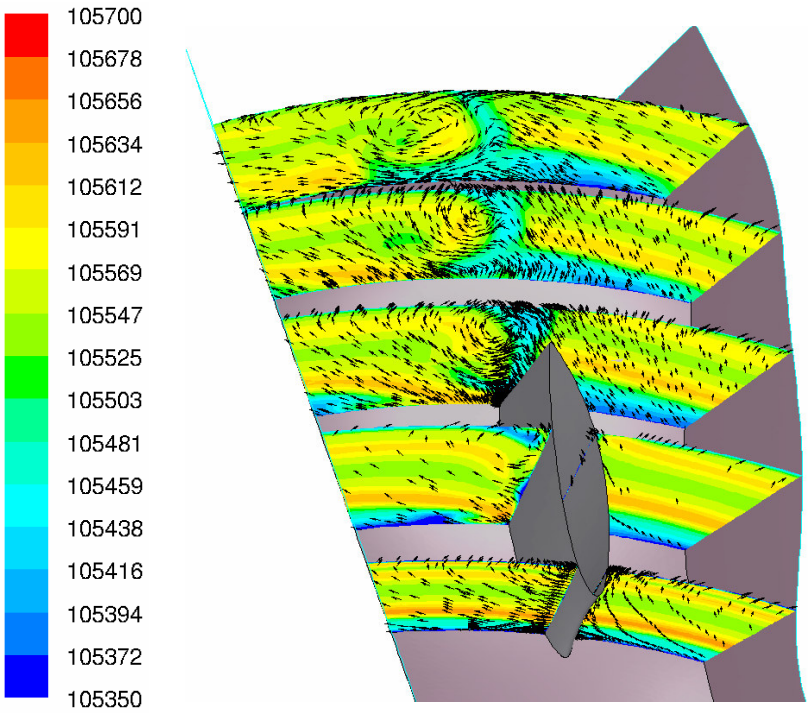

Figure 14: Contour plot of the total pressure and velocity vectors in five different planes [Pa].

4.4 Comparison between 2D and 3D

The comparison between the HTC considering 2D vs. 3D AITEB2 duct flows is shown in Figure 15. Exactly the same BCs are used in both cases. The results agree relativity well except the region close to the inlet which differs a lot, both for the hub and shroud. One conclusion which can be made is that the 2D calculations give an idea about the magnitude of HTC. The 2D case predicts relatively well the axial positions of the maximum and minimum points of the HTC.

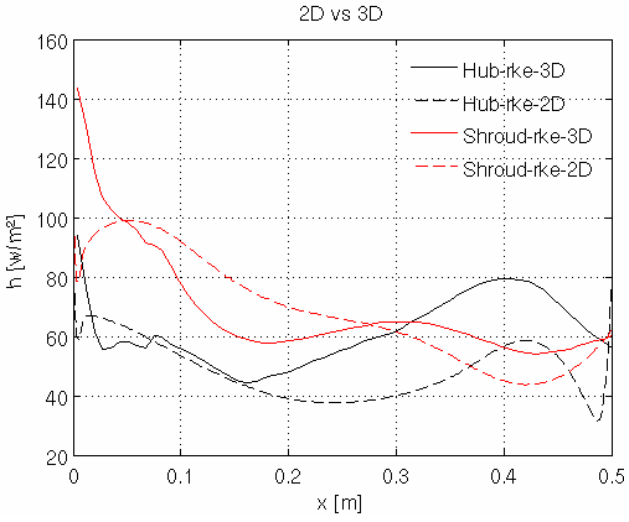

Figure 15: Comparison of HTC for the 2D and 3D ducts.

5 Turbine Mid Structure – Internal Part

5.1 Introduction

The internal cooling flow within a TMS must be studied in order to understand the flow structure and heat transfer levels. The flow is very complex and three dimensional and is driven by the pressure difference between the inlet and different leakages (outlets). The cooling flow level is set in order to limit the material temperature and to avoid that hot gas path air is ingested into the internal cavity.

5.2 One sector analysis

5.2.1 Configuration

The geometry of the model is a very simplified typical representation of the flow domain in between the cold and the hot structures of a TMS. The cooling flow inlet is a circular cylinder and the leakages are modelled as narrow outlets, see Figure 16. Further the number of vanes is chosen to be 12 so a sector of 30 degrees is enough for analysis due to periodicity. The chosen dimensions of the model are typically for TMS components.

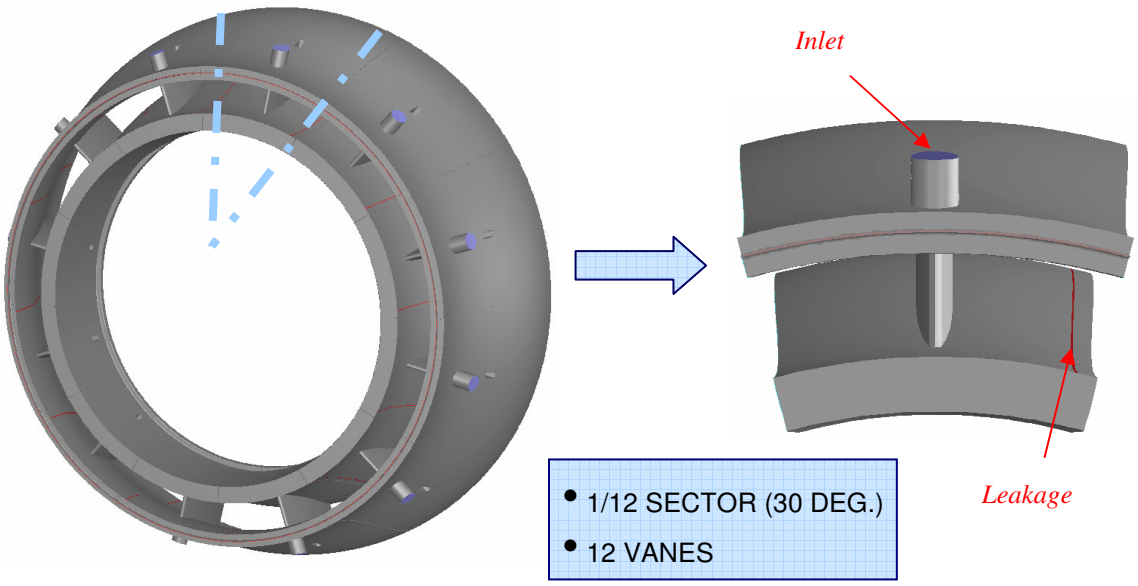

Figure 16: Internal structure of the TMS, full model (left) and one sector (right).

5.2.2 Mesh

Meshing the model is one of the most challenging and instructive tasks during this thesis work. However the net product is a qualitative mesh shown in Figure 17 below.

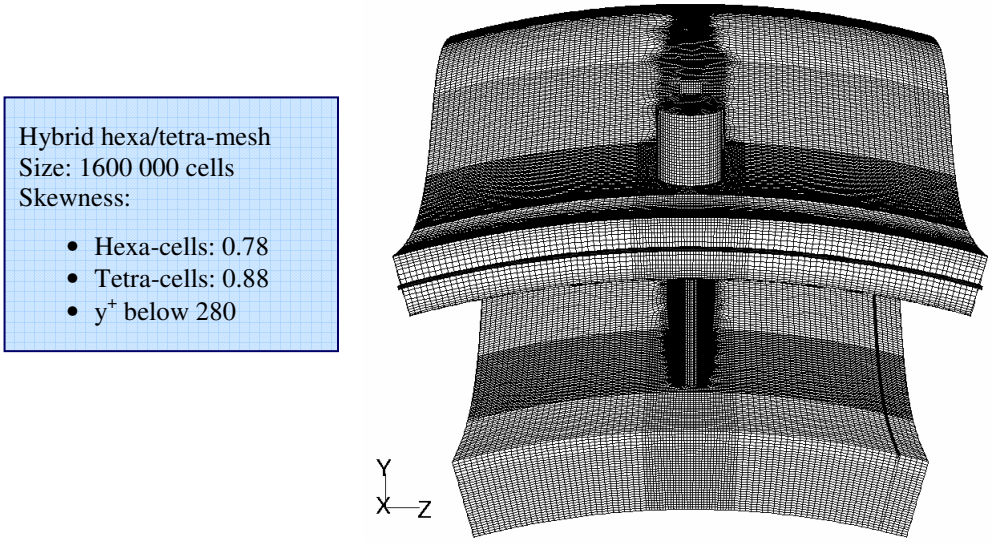

Figure 17: The mesh of the internal cooling CFD model.

To ensure that the solution is mesh independent, a mesh study is done due to both fluid flow and heat transfer. The solution seems to be mesh independent. All results and further information about the mesh study can be found in the Appendix C2. All specifications of the used mesh sizes are presented in table 3 below.

Part	Sizing function [mm]
External case	1
Shroud	0.8 + (grading 1.15)
Vane	0.5 - 1
Hub	0.5
Global interval size	2

Table 3: The sizing function of the mesh, grading is the ratio between adjacent cells.

5.2.3 Boundary Conditions

For simplicity, typical and reasonable values are chosen as BCs. The inlet pressure is set to 6.5[bar] and the outlets to 6.0[bar]. These settings yield a mass flow of about 2% of the external duct flow. The hot structure is set to 1200[K] and the cold one to 900[K]. The cooling flow has a temperature of 700[K]. This yields a heat transfer from the wall to the flow, see Figure 18. The periodic BC is of course set to rotational with rotation-axis direction towards positive x.

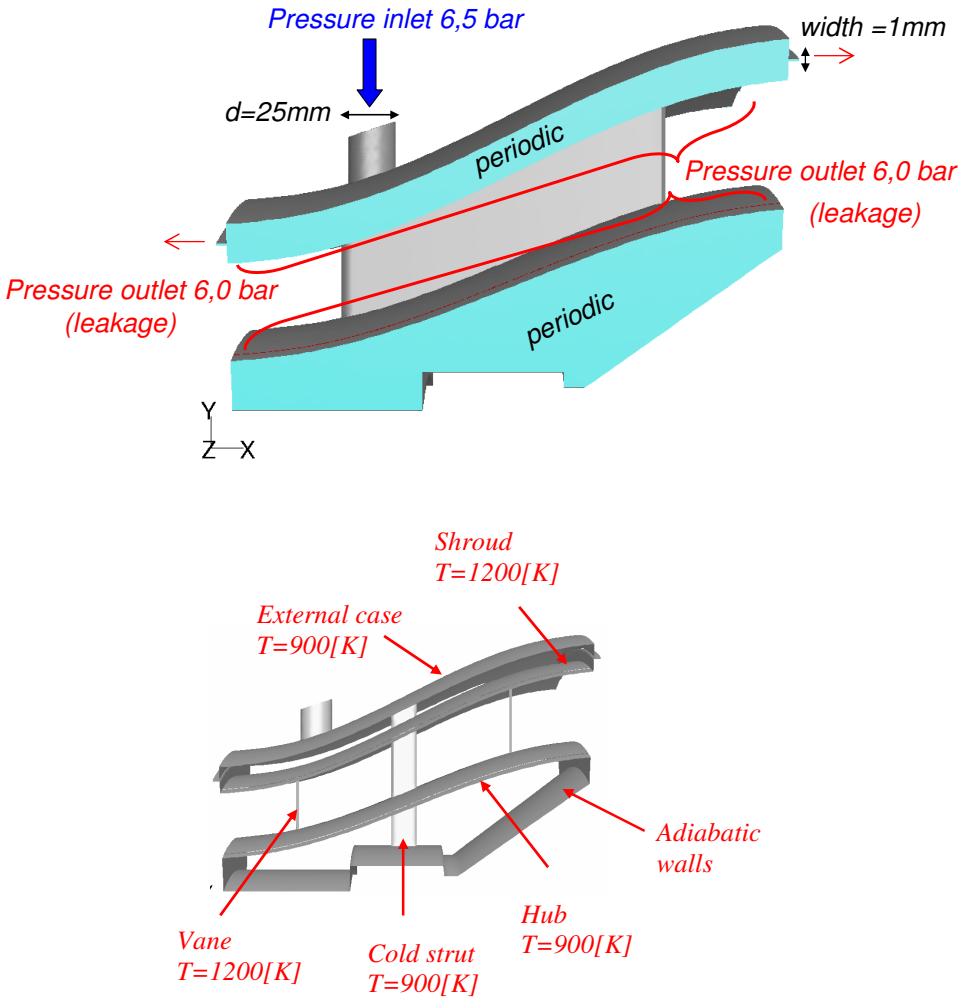

Figure 18: Geometry and BCs for the internal cooling model.

5.2.4 Evaluation surfaces

It is quite important to consider how to evaluate the results before creating the mesh and doing any calculations. It is easiest to define evaluation surfaces in the meshing generator. The surfaces chosen are close to the interesting walls at shroud and hub, see Figure 19. The advantage is that one gets the desirable quantities calculated at the nodes of the evaluation surfaces. Otherwise if these are defined in the postprocessor, the quantities are interpolated between adjacent nodes.

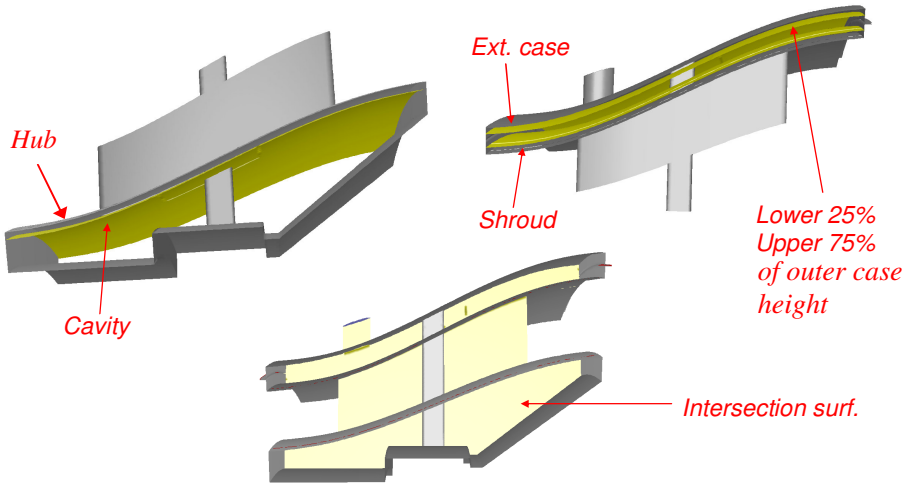

Figure 19: Evaluation surfaces at the intersection and close to external case, shroud and hub.

5.2.5 Results and discussion

The results are divided up in two sections, one for the fluid flow and the other presents heat transfer results. These two sections are also divided in two subsections. One that deals with globally obtained results and the other is concentrated on locally obtained ones.

Fluid flow - global consideration

To get an idea of how the flow is distributed in the sector, a check of the total mass flow rate through the different leakages in comparison with the inlet mass flow rate can be done. These results are schematically presented below in Figure 20. It's quite clear that the sector-sector leakages are of big concern in comparison to the other two. One of the causes is that almost all fluid flow is guided down through the vane and thus finds it easy to leave through these leakages.

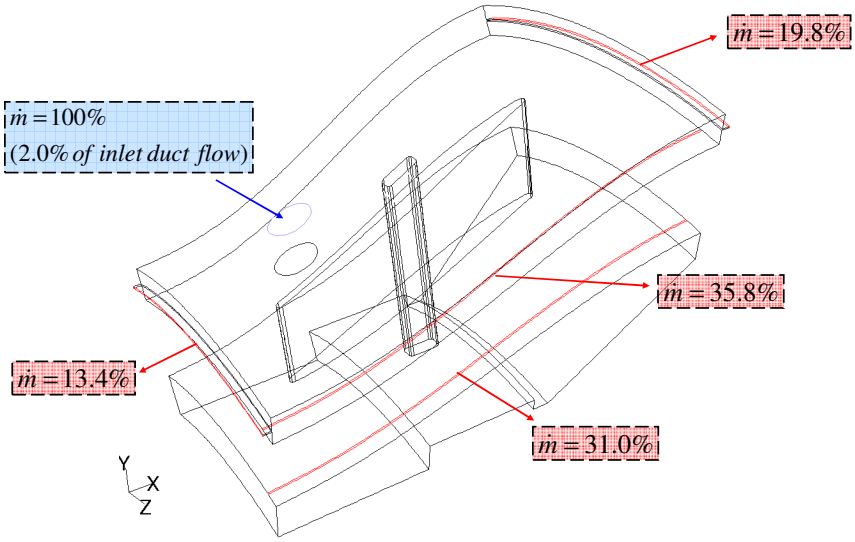

Figure 20: Distribution of mass flow rates [%] of inlet cooling flow.

This is further visualised through the path lines released from the inlet and outlet of the vane and is presented below in Figure 21.

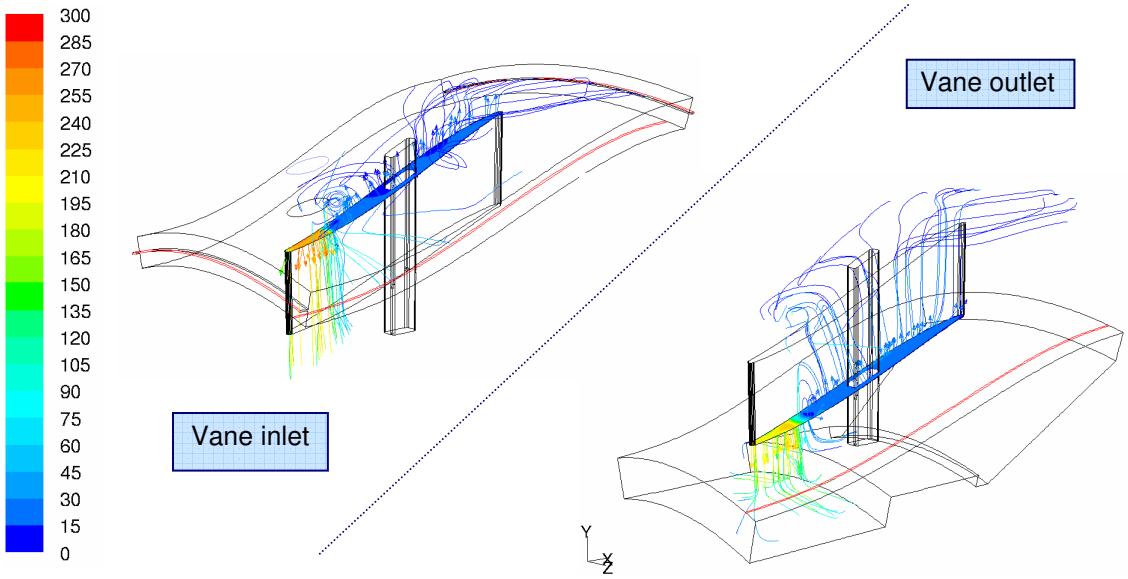

Figure 21: Path lines released from the inlet and outlet of the vane [m/s].

The fluid is going back into the outer cavity through the vane and out through the leakages, this is however at very low velocity in comparison with the main flow through the vane. There are several vortices observed. One is inside the vane and is generated due to opposite meeting flows. There is also a vortex in the inner cavity. In the outer cavity prior to the inlet, near the front leakage, is also a vortex created. The velocity is clearly quite low in the inner and the outer cavity near the rear leakages. This is shown in Figure 22 below.

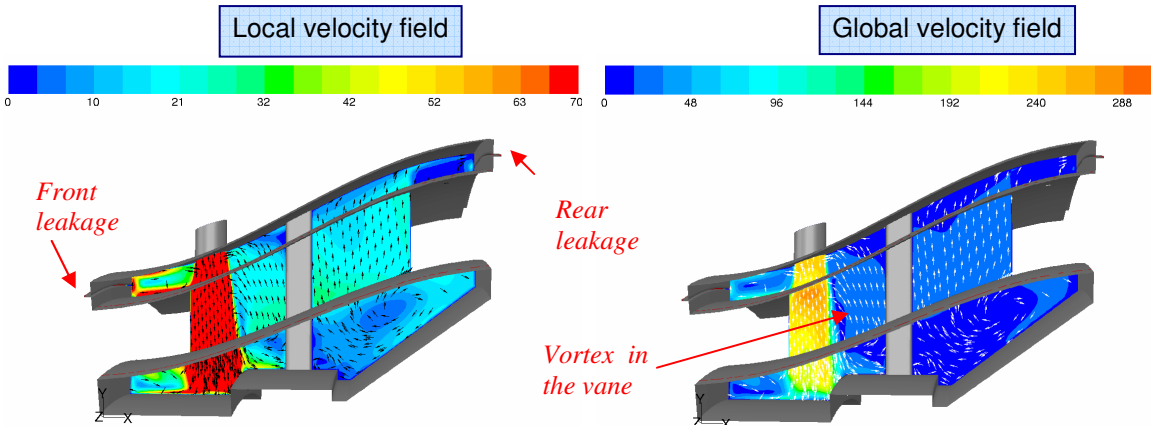

Figure 22: Local and global velocity field [m/s] at the intersection evaluation surface.

Fluid flow - local consideration

To continue the investigation of the flow field within the sector, the velocity contours together with velocity vectors pointing in the direction of the flow and projected in the plane of consideration is plotted below in Figures 23 and 24. The vectors have fixed length in order to only show the direction of the flow. Different axial positions are chosen both in the inner cavity below the hub and in the outer one, above the shroud. The velocity fields are presented below. In order to observe any periodic phenomenon, three sectors are plotted together only for visualisation. It is quite important to note that these three sectors are identical because it is copied two times to obtain the three sectors plots.

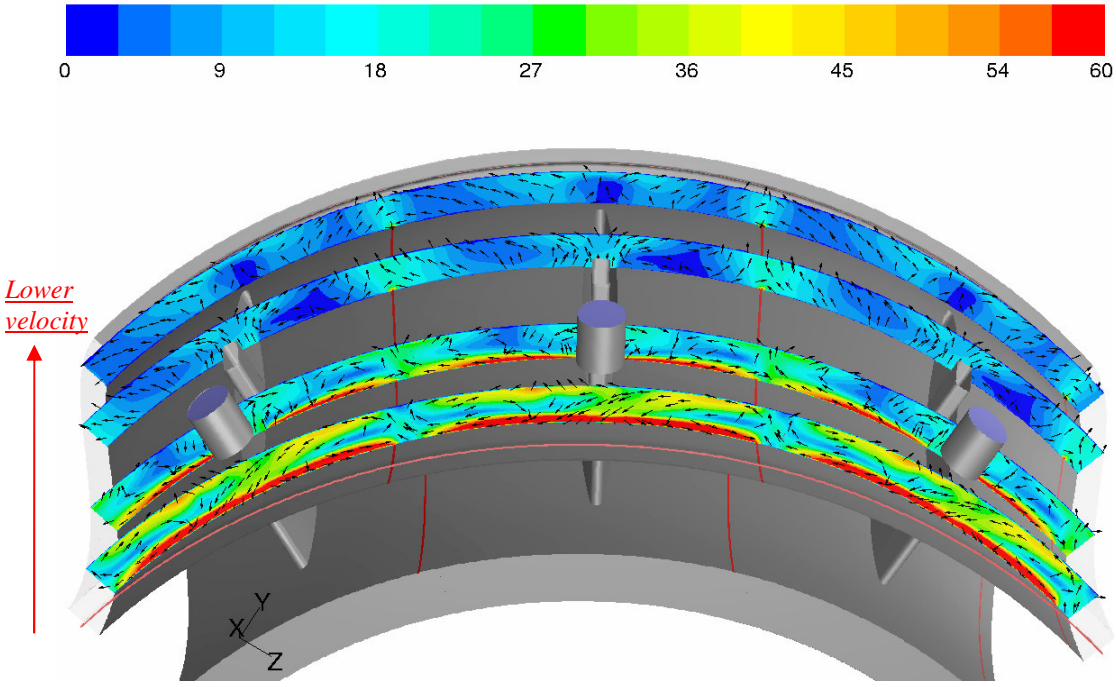

Figure 23: Velocity fields [m/s] at different axial positions in the outer cavity.

The impinging cooling flow is now fully guided through the vane. Some of it hits the shroud and goes out through the leakages.

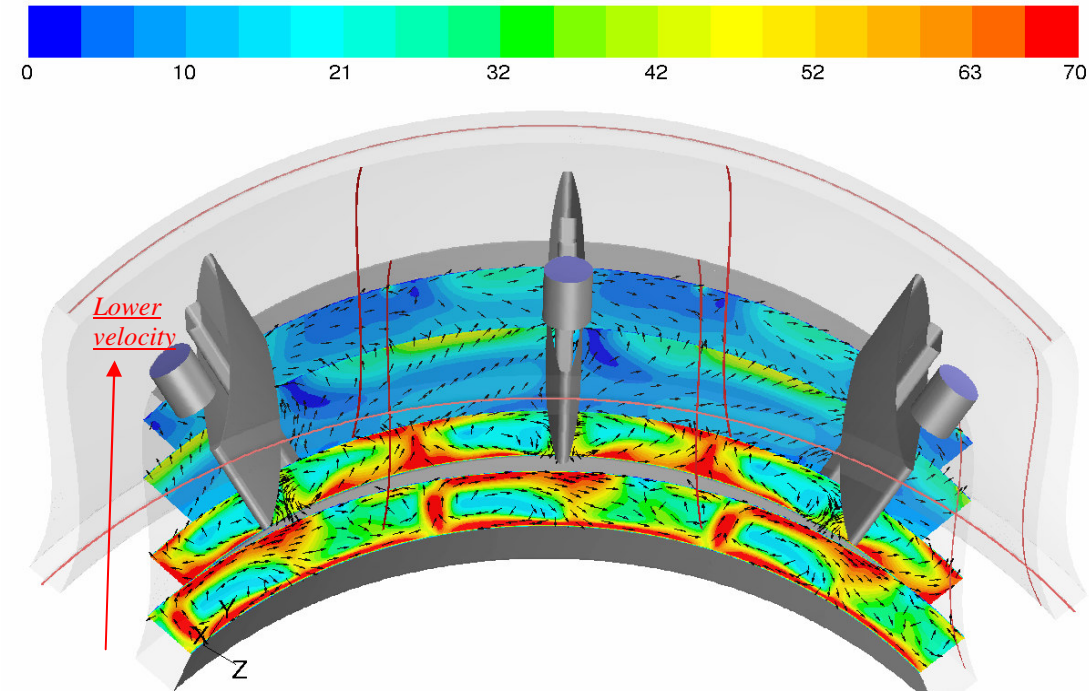

Figure 24: Velocity fields [m/s] at different axial positions in the inner cavity.

It's clear that the flow field has a lot of complexity. It's also clear that the high velocity region is where the cooling flow is impinging. The impinging jet creates two big vortices that are smeared out axially and flows back into the vane. There are actually regions with almost zero velocity and this is harmful to the fairing hub in regard to heat transfer.

Heat transfer - global consideration

The heat transfer is closely related to the velocity. At high velocity the heat transfer is high and vice versa. It's quite interesting to see what temperature on average the fluid have when it leaves the outlet. Below a schematic picture of these heated outlets is presented in Figure 25.

To further globally analyze the heat transfer within the sector, area average heat flux and temperature are calculated on each interesting wall and its corresponding evaluation surface. It's expected that the hot structure shows high heat transfer rates because heat flux is proportional to the temperature difference. This is actually the case. It's obvious that heat transfer has occurred from the hot walls to the cold fluid. Table 4 below shows average values of the surface heat flux of different interesting parts.

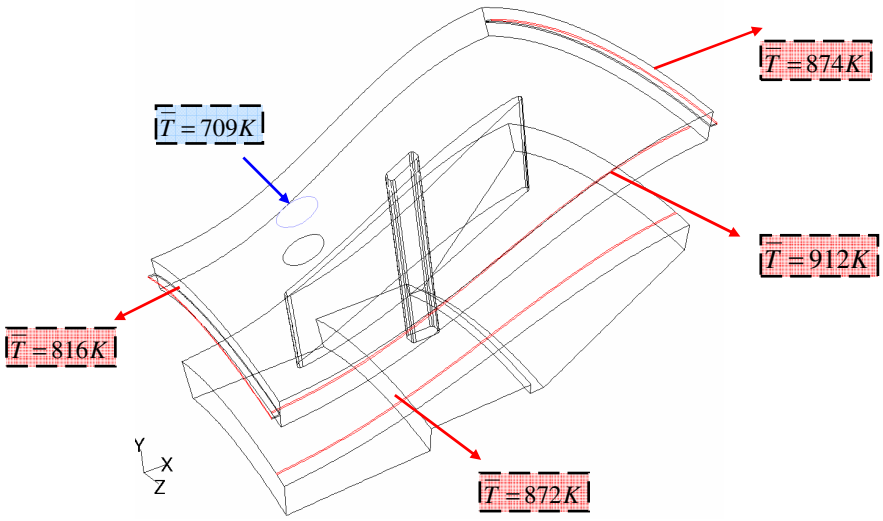

Figure 25: Heated inlet and outlets.

Figure 25 above is very similar to the one for mass flow distribution, Figure 20. It shows that highest mass flow rate through an outlet gives highest heated outlet.

Wall	Temp (K)	Av. qw (kW/m^2)
External case	900	15.8
Shroud	1200	159.7
Vane	1200	178.9
Cold strut	900	20.9
Hub	1200	150.7

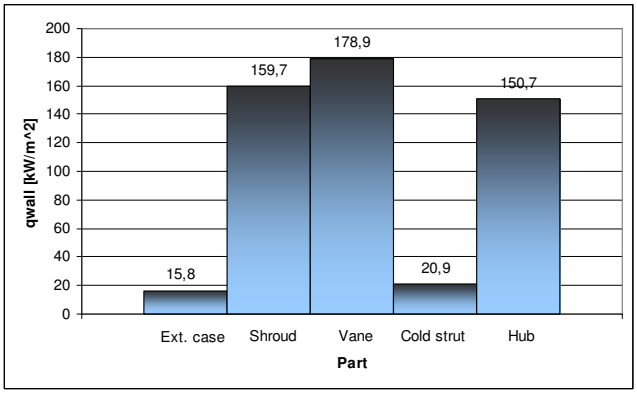

Table 4: Average heat flux at the walls in the TMS.

As expected, there are high heat transfer rates on the hot structure due to the large temperature difference.

Heat transfer – local consideration

The local heat transfer investigation of different walls is of high importance. First of all it is important to ensure that the material has an even distribution of temperature. If there are large differences the material can be damaged. It is also quite important to know the location of maximum and minimum temperature on the wall. This local study is performed on every part in the hot and cold structure of the TMS. In the previous section the flow field became quite obvious through the analysis done. In this section the flow field is plotted at the evaluation surface of the considered wall. This surface is also used for the temperature contour plot so that one achieves the air temperature above or below

the considered wall. Finally a contour plot of surface heat flux on the wall is presented. The results of the external case are presented below in Figure 26.

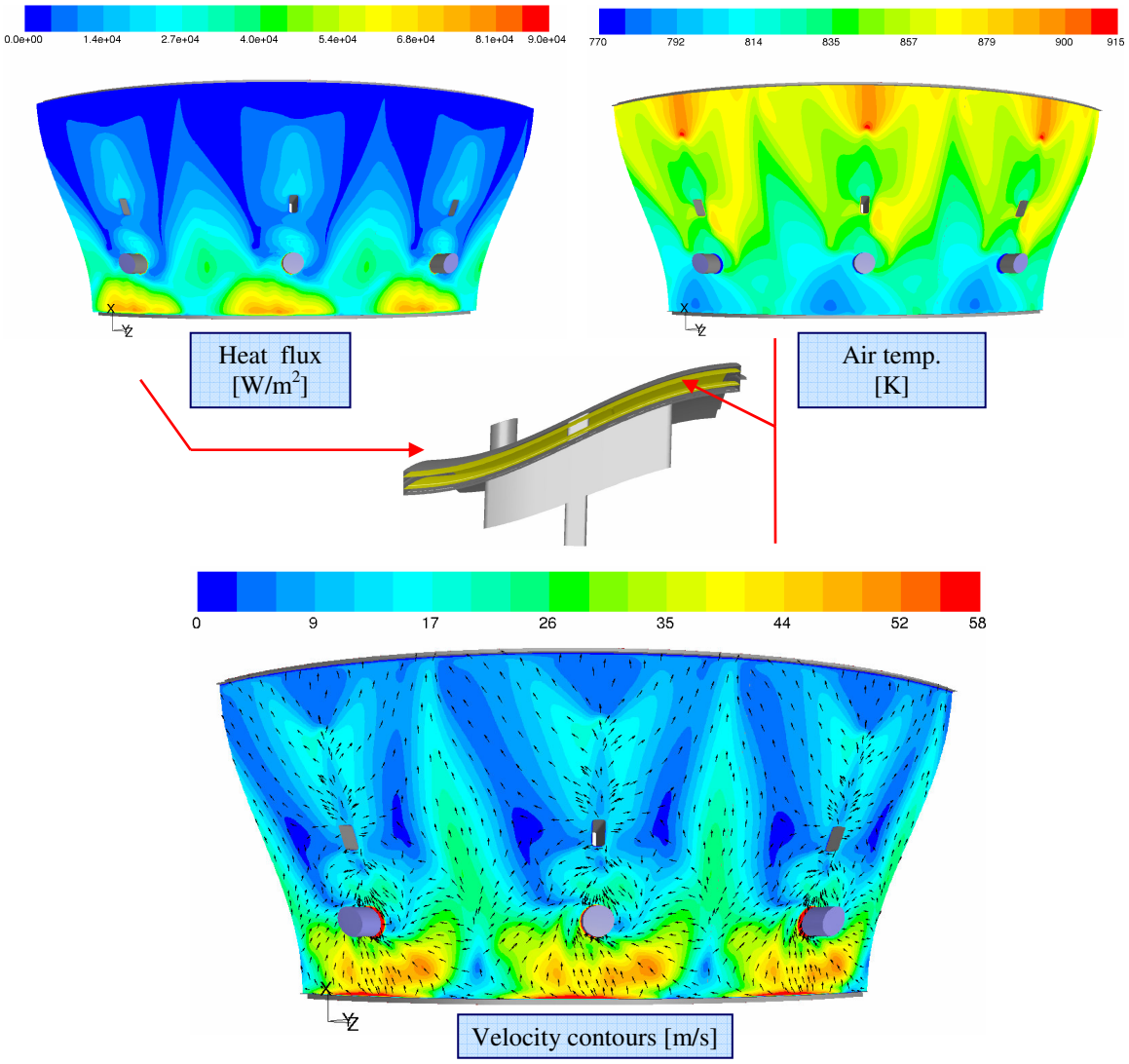

Figure 26: Heat flux, air temperature and velocity field for the external case.

The results are quite interesting. There are large differences in heat flux and in the air temperature below the wall. The velocity field shows that there is a large low velocity region in the sector which yields a low heat flux and therefore high temperature on the considered wall. It's also obvious that at high velocity the cooling performance is high and the heat flux is large. This yield low temperature on the material.

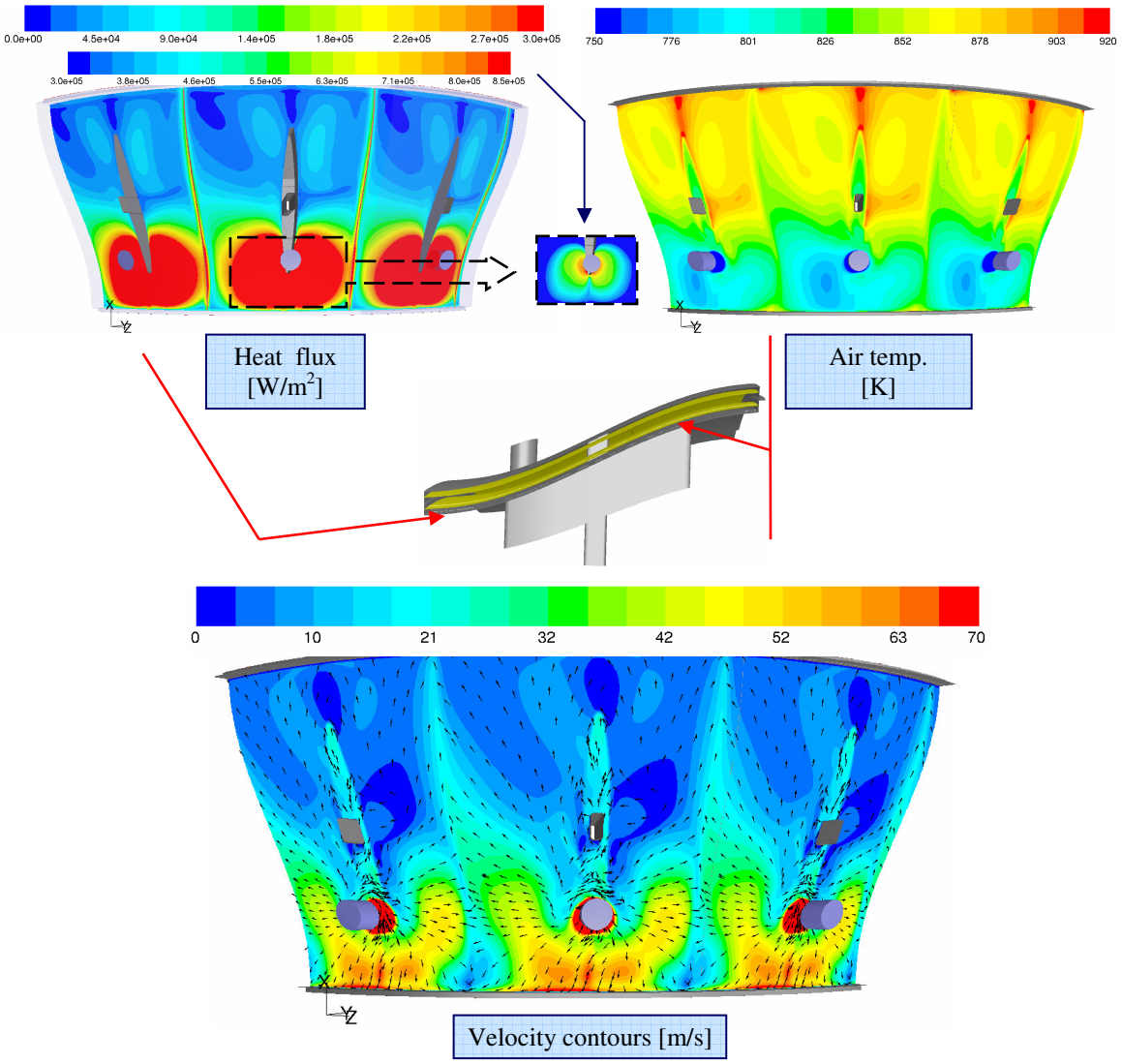

Figure 27: Heat flux, air temperature and velocity field for the shroud.

The discussion for the external case is also valid for the shroud shown above in Figure 27. There are actually higher differences and also higher velocities. There is high heat flux where the jet impinges and cools a big area. The cooling spreads throw the material but not everywhere, so as mentioned earlier, the distribution is really not even for this considered wall. The next wall to investigate is the hub and the results are presented below in Figure 28.

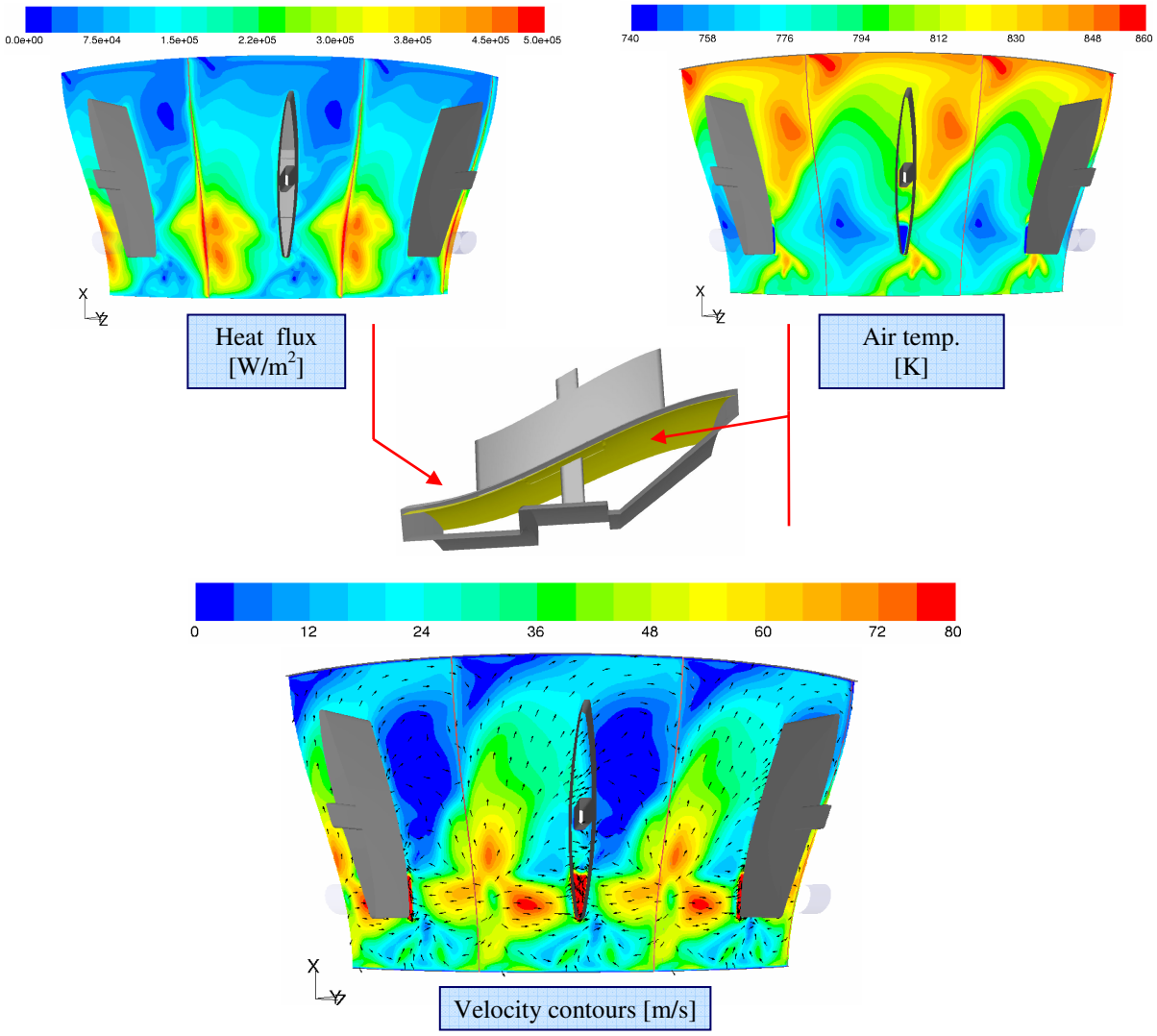

Figure 28: Heat flux, air temperature and velocity field for the hub.

For the hub there is a high velocity region, observed previously on the left hand side of the vane. This region is due to the vortex that is generated by the impinging jet. There is also a very low velocity region where the heat flux is low and therefore the temperature is high.

5.3 Three sectors

The study of one sector above is essential for heat transfer analysis of the TMS. It is however important to consider a more realistic case and compare the results. The number of inlet bosses for cooling flow is usually limited in a TMS and is often one per three sectors or even four sectors. This limitation is due to manufacturing concerns. This case study includes building up the geometry, meshing and run it for comparison. The geometry is identical to the previous one considered but the boss in the middle sector only is the inlet of cooling flow. This chapter is divided in two sections. The geometry/mesh and the results obtained. The structure for the results is very similar as in the previous sections.

5.3.1 Geometry and Mesh

The procedure for building up the geometry of the three sectors model is quite easy. It is similar to the one-sector model and is shown in Figure 29 and 30. The time consuming task in this case is to define all BCs and of course run it for a solution. The mesh is shown in Figure 31 and is a high quality one. Basic facts about the mesh are found below. For more information about the mesh, see section 2.4.

The model is quite simplified as described in the previous sections. The leakages have the same positions as before and the only difference is three sectors with one inlet boss instead of three bosses. The inlet boss is located in the middle sector as shown in Figure 29 below.

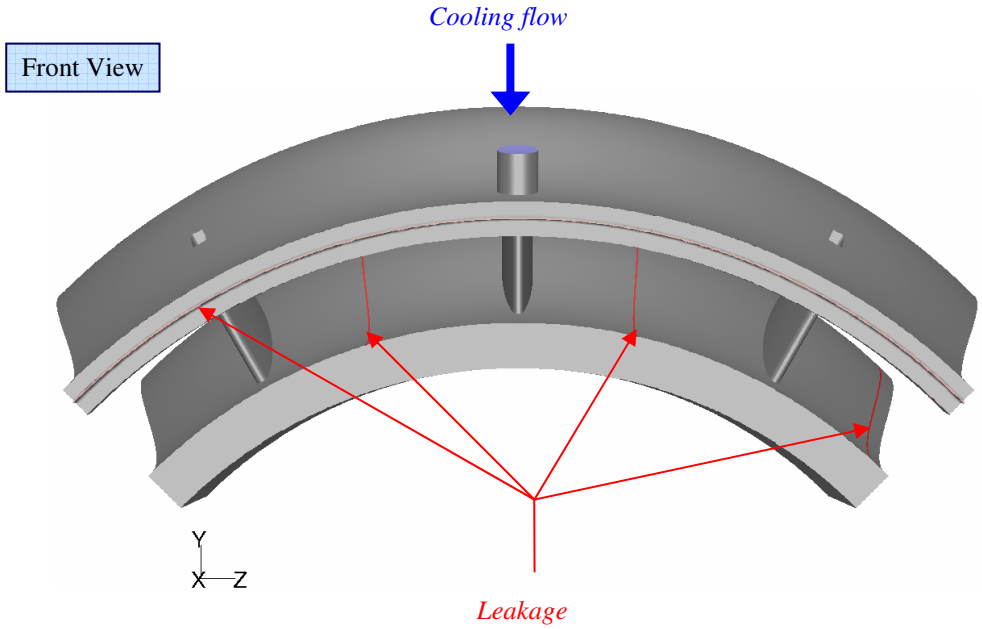

Figure 29: Geometry of the three sector model, front view.

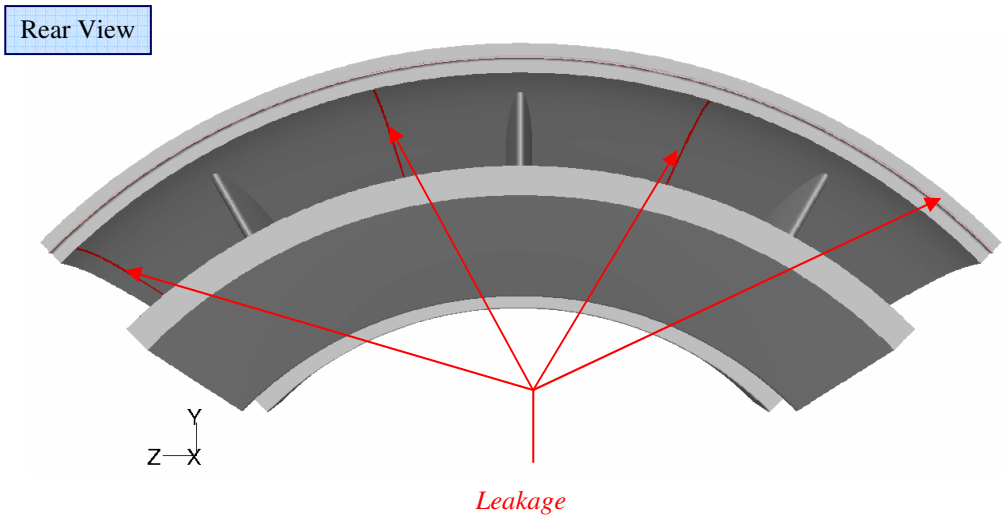

Figure 30: Geometry of the three sector model, rear view.

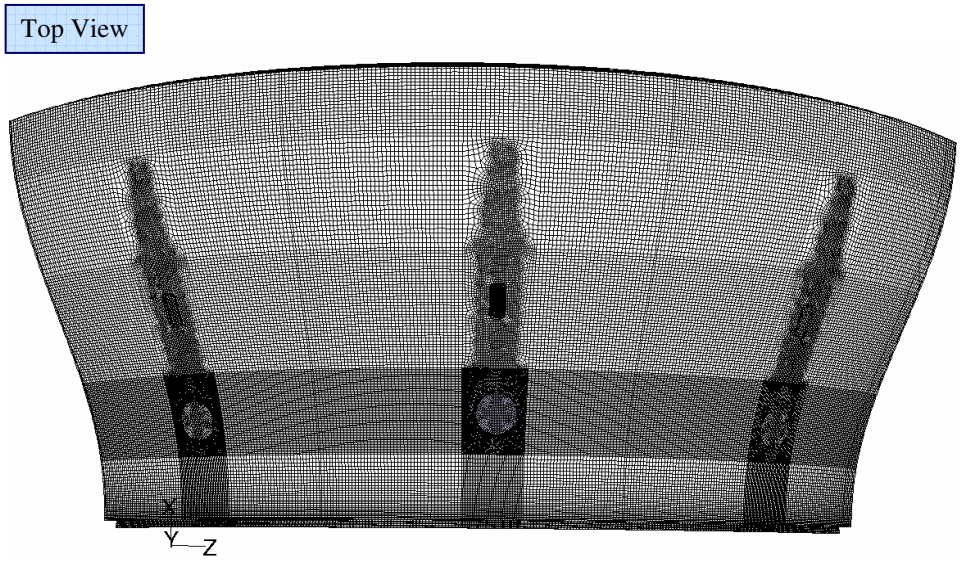

- Hybrid Hex-Tet, generated in Gambit
- About 5 220 000 cells
- Skewness
  - hex cells: 0.78
  - tet cells: 0.88
- Global interval size: 2mm

Figure 31: Mesh of the three sector model, top view.

5.3.2 Results and discussion

This results section follows the same structure as the previous one. It is divided up in two sections, one for the fluid flow and the other for heat transfer. Each section is then divided in two subsections. One which deals with globally obtained results and the other is concentrated on locally obtained ones.

Fluid flow - Global consideration

First it's interesting to check the mass flow distribution through the different leakages. These results are schematically presented below in Figure 32.

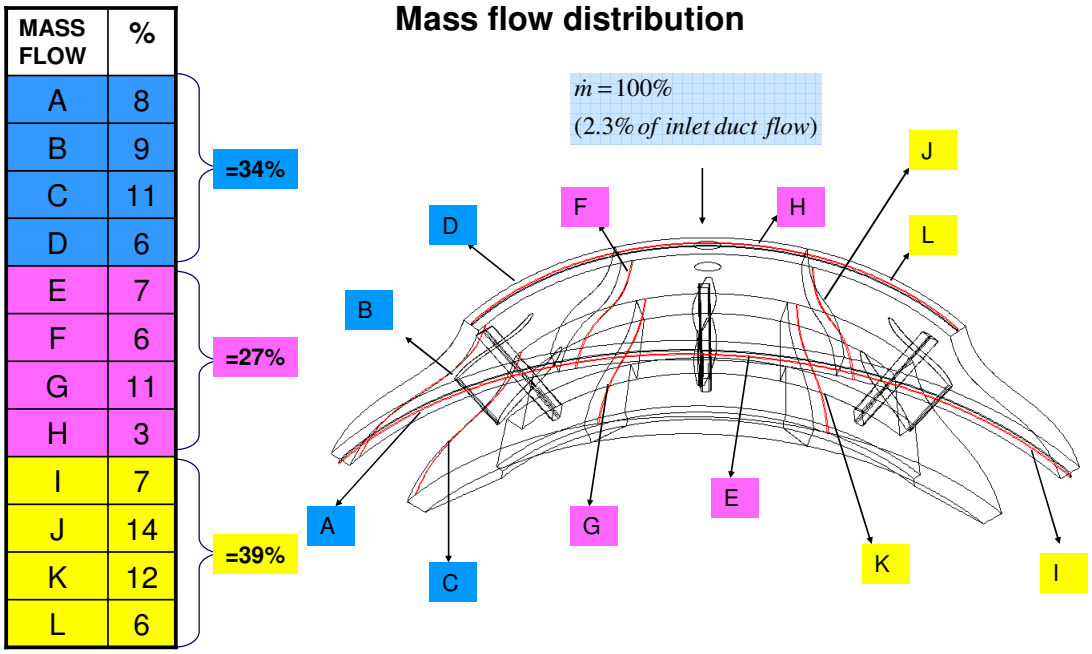

Figure 32: Mass flow distribution.

It's quite clear that the sector-sector leakages are of big concern in comparison to the other two. The flow seems to be asymmetric but this is only because the location of the leakages is not at the sector-sector interface. If the leakages are located there they will probably cause numerical problems because of the periodic BC. However it's clear that the flow seems more likely to leave to the left or to the right than the middle. This global consideration of the flow field is further investigated in the heat transfer section where the flow field is plotted together with the heat transfer quantities. This includes the flow field at the external case, shroud, hub and all the three vanes. To further analyze the fluid flow a local analysis is done below.

Fluid flow - Local consideration

To continue the study, the velocity contours are plotted with velocity vectors that are pointing in the direction of the flow and also projected in the plane of consideration, see Figure 33 below. In order to only visualise the direction of the flow, the vectors have fixed length. The same axial positions, as for the previous one-sector model, are chosen both in the inner and outer cavity. Unlike the previous section, the three sectors there were plotted only for periodic visualisation. Here the three sectors are the whole model which is run for investigation.

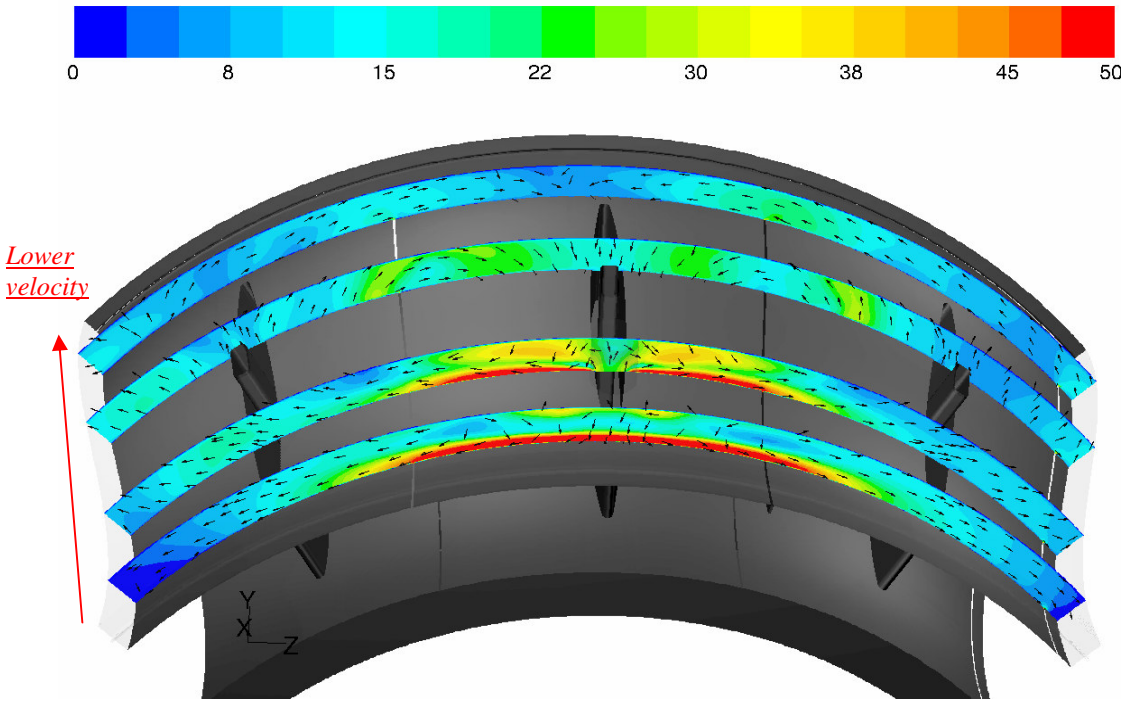

Figure 33: Velocity fields [m/s] at different axial positions in the outer cavity.

It's obvious that the high velocity region is in the middle sector and the low velocity region is near the front side of the other two sectors. The flow seems to be quite symmetric and it is of high importance to observe that the difference is large between the highest and lowest velocity. Further the flow behaves much differently in this model in comparison with the one-sector model. This ensures that it is necessary not to only consider one sector in the analysis. One can also observe that two big vortices are produced. This is further visualised in the heat transfer section. The analysis is continued through plotting the same quantities in the inner cavity in Figure 34.

The flow field seems to be very complex with several high and low velocity regions. It is however clear that the impinging flow hits the cavity and is guided up through the left and the right vane. This is due to the impinging jet where the flow velocity is zero in the middle and accelerates to the neighbouring regions.

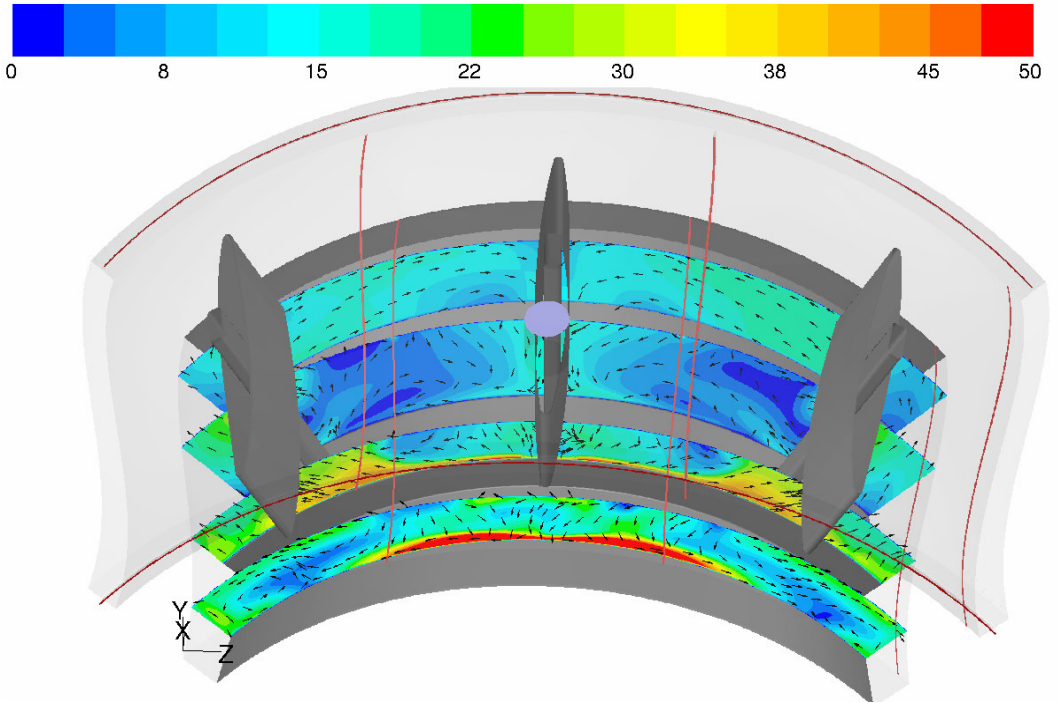

Figure 34: Velocity fields [m/s] at different axial positions in the inner cavity.

As previously observed in the one-sector model there are regions with almost zero velocity that is harmful to the hub in regard to heat transfer. However the flow field is very complex which cause non-uniform heat transfer and has to be analyzed further.

Heat transfer - Global consideration

Following the same pattern as for the one-sector case, it's quite interesting to see what temperature on average the fluid has when it leaves the different outlets. Below a schematic picture of these heated outlets is presented in Figure 35.

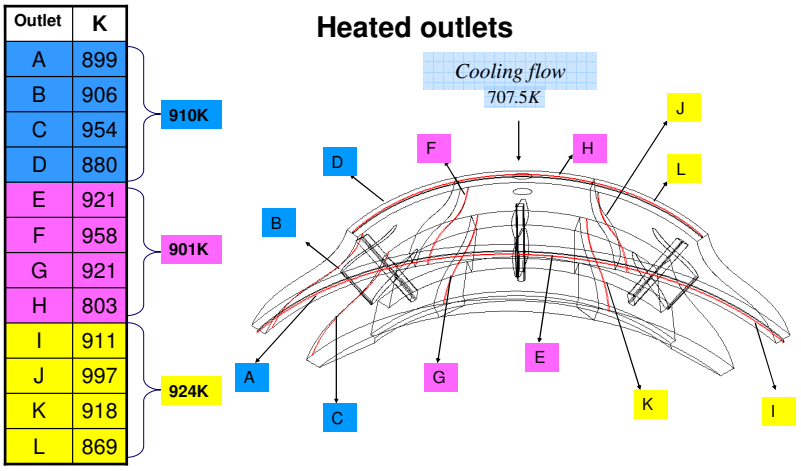

Figure 35: Heated inlet and outlets.

The result in Figure 35 is very similar to the one for the mass flow distribution in Figure 32. It shows that highest mass flow rate on an outlet yields the highest heated outlet. Further not the same outlet in each sector possesses the highest temperature.

To further globally analyze the heat transfer within the three sector model, the area average heat flux and temperature are calculated on each interesting wall and its corresponding evaluation surface. Table 5 and the diagram below shows the average values of the surface heat flux for different interesting parts.

Wall	Temp (K)	Av. qw (kW/m^2)
External case	900	3.46
Shroud	1200	67.2
Vane centre	1200	126.9
Vane left	1200	49.5
Vane right	1200	46.1
Cold strut centre	900	6.1
Cold strut left	900	10.7
Cold strut right	900	9.2
Hub	1200	62.8

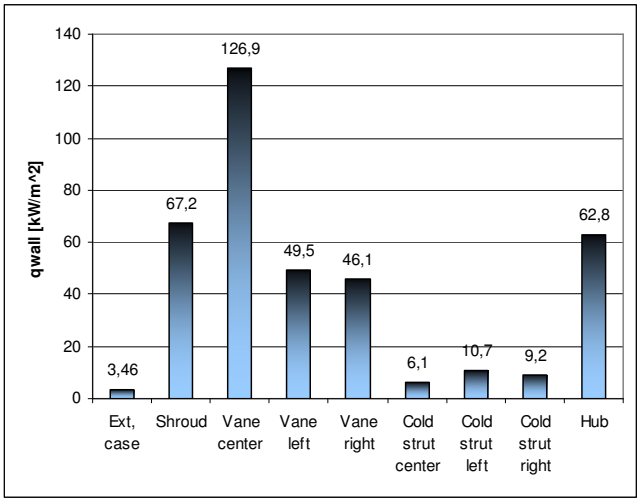

Table 5: Average heat flux of different parts in the TMS.

The centre vane is dominating the heat flux and this is expected because the flow is firstly guided through it. This is due to the impinging jet which hits the front part of the vane wall. Further the hot structure has much larger heat flux than the cold one which is also expected. The values on the external case, the shroud and the hub are not divided into three sector-values. These are the net values of all the three sectors.

Heat transfer – Local consideration

In this section the velocity flow field is plotted at the evaluation surface for the considered wall. This surface is also used for the temperature contour plot so that one achieves the air temperature above or below the considered wall. Finally a contour plot of surface heat flux of the wall is presented. The results of the external case are presented below in Figure 36.

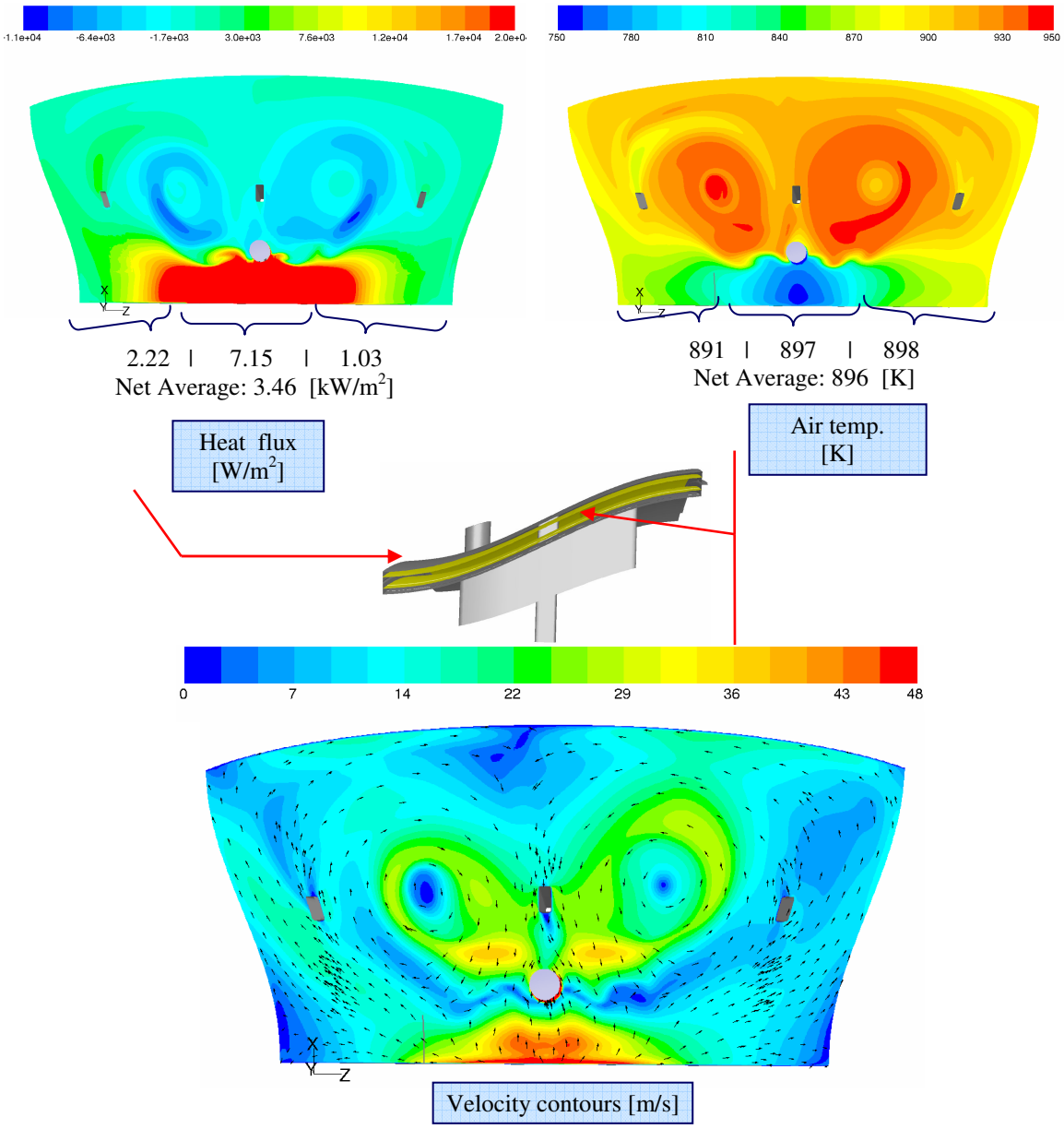

Figure 36: Heat flux, air temperature and velocity field for the external case.

The results presented above are unlike those for the one-sector. There are two big vortices that create high and low velocity regions. There are also regions where the velocity is almost zero. These differences between the high and the low velocity regions are of concern and are negative for the material. The size of the vortices is not equal due to the position of the leakages. These vortices are created by the impinging jet which hits the shroud and spread in the outer cavity. Much of the flow goes through the vane, but because the inlet boss is large not all the flow goes down through the vane. The spread flow in the outer cavity goes to the front side of the model and creates a complex flow pattern. Some of it goes out through the front leakage.

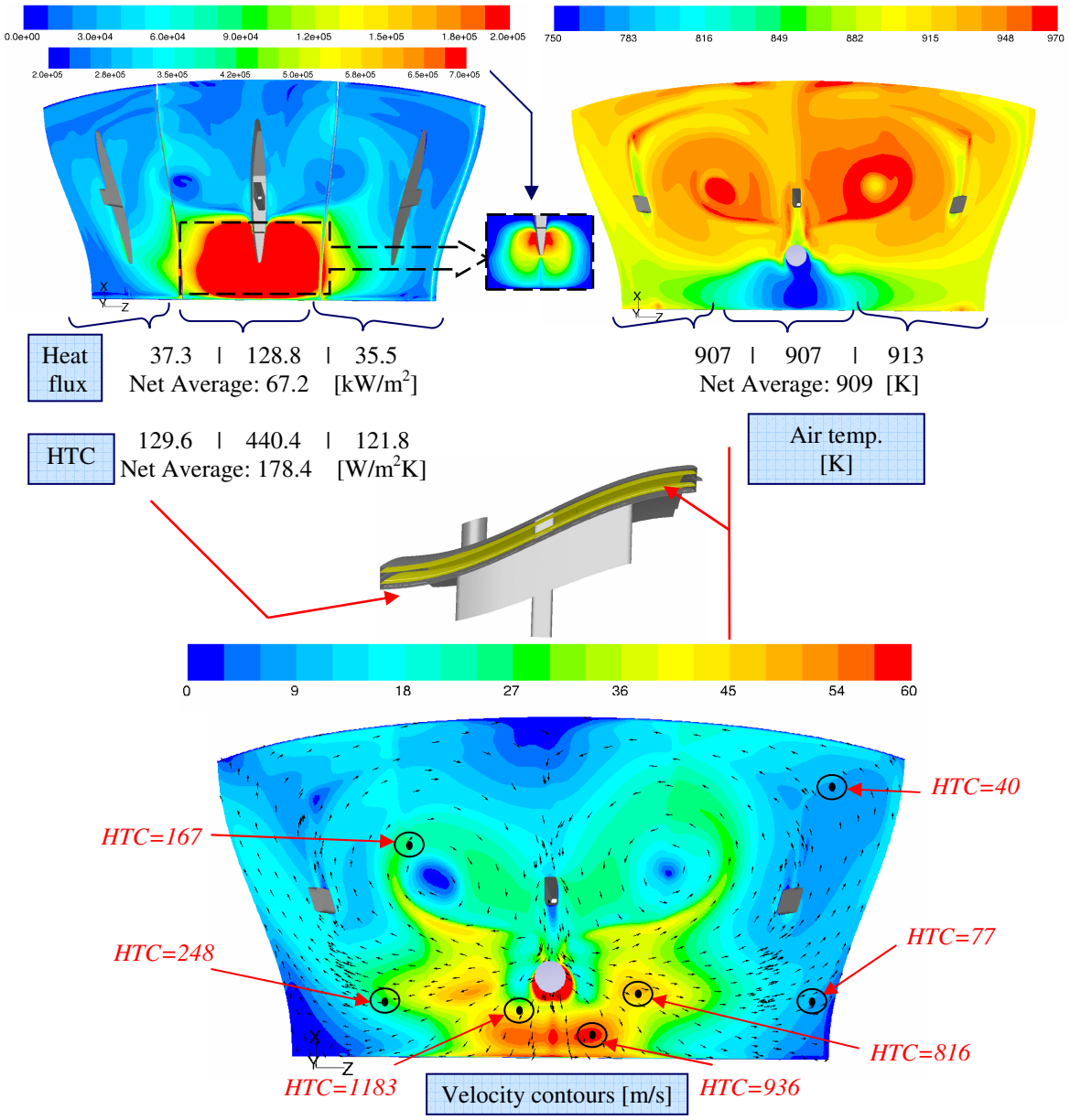

Figure 37: Heat flux [W/m^2], air temp. and velocity field for the shroud, values in red [W/m^{2}K].

The flow spreads also sideways and because of the leakages in the middle sector, the flow goes back and hence one has the two big vortices visualised in figures 37 and 38. Considering the air temperature below the external case, the pattern of high and low temperature regions follows the one for the velocity contours. The fluid is cold where the velocity is high and hot where the velocity is low. The air temperature varies from 750-970[K] so there is a very large difference between the highest and the lowest air temperature. Similarly for the heat flux on the shroud, the range is 0-700[kW/m^2]. Considering HTC marked red in the figure above, there is a wide range between the lowest and the highest. The values are taken at the wall but marked on the velocity surface in order to visualize the order of velocity which corresponds to certain HTC values. These results show that the cooling flow can seriously damage the material

because of these high differences and that it is very important to consider this issue when implementing the cooling flow in reality. The discussion for the external case is also valid for the shroud shown above and one of the obvious differences is that the velocity range is wider. The high heat flux where the jet is impinging is further zoomed in. This is to clarify the heat flux distribution in that area. The cooling spreads on the material but not everywhere, so as mentioned before the distribution is really not even which is negative for the considered wall. The next wall to investigate is the hub and the results are presented below in Figure 38.

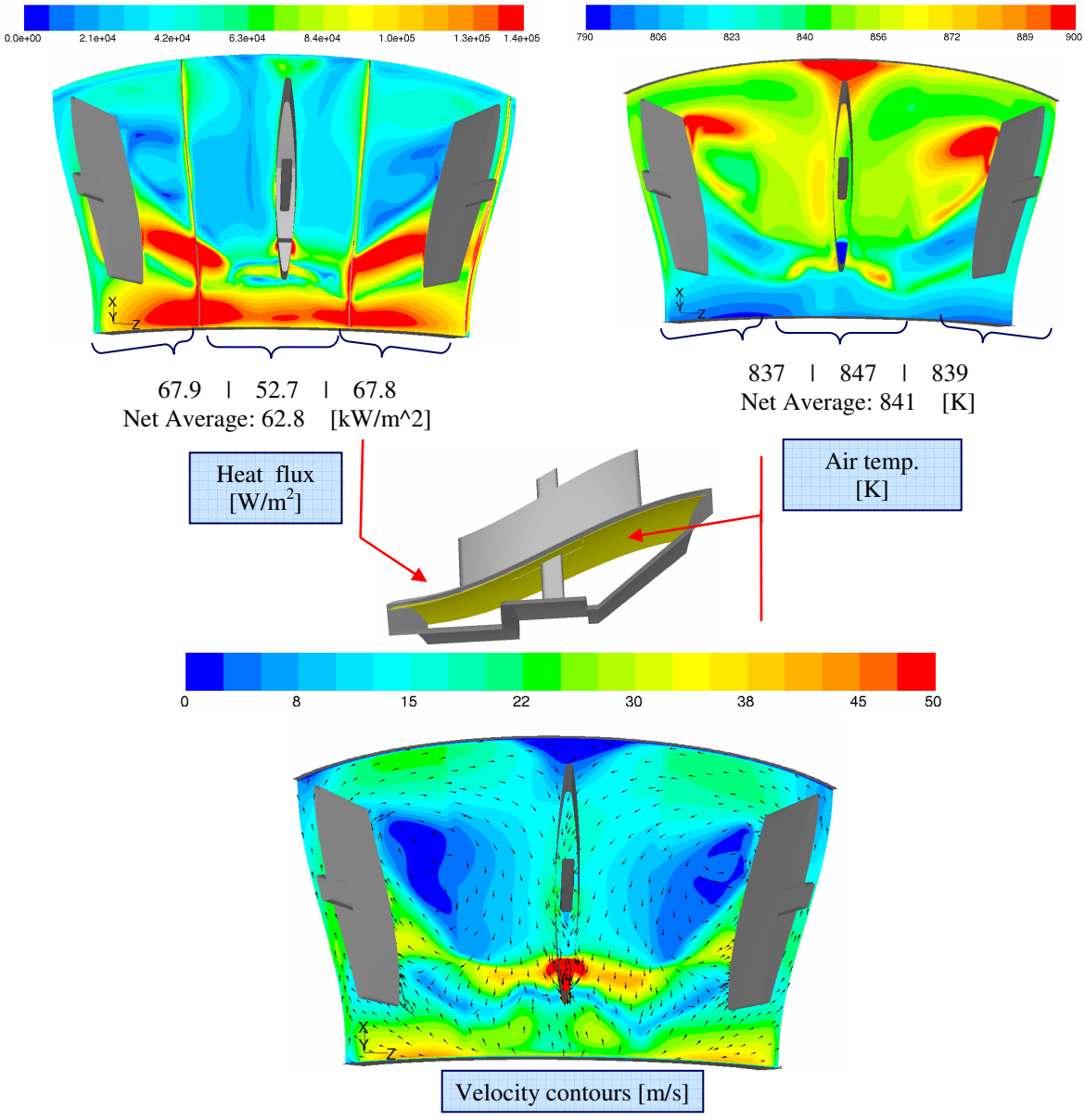

Figure 38: Heat flux, air temperature and velocity field for the hub.

Considering the hub there are two large low velocity regions. The velocity is below 8[m/s] and there are regions where the heat flux is almost zero and therefore the temperature is high. It's obvious that the flow is complex but one can observe that a high

velocity region exist near the side vanes, there the flow goes up and is driven by the pressure difference. The impinging jet and how it spreads is observed in the velocity plot above in Figure 38. Much of the flow is spread to the front side of the model which causes cold fluid to be present in that area, and also gives rise to a high heat flux. However, the two big vortices created in the inner cavity below the hub are causing serious problem in the heat flux. This is observed in the contour plot of heat flux in Figure 38, where large areas of low heat flux exist. Again it is obvious that when considering the plots of heat flux and velocity magnitude one observe a proportional relation between these two quantities which is of course expected.

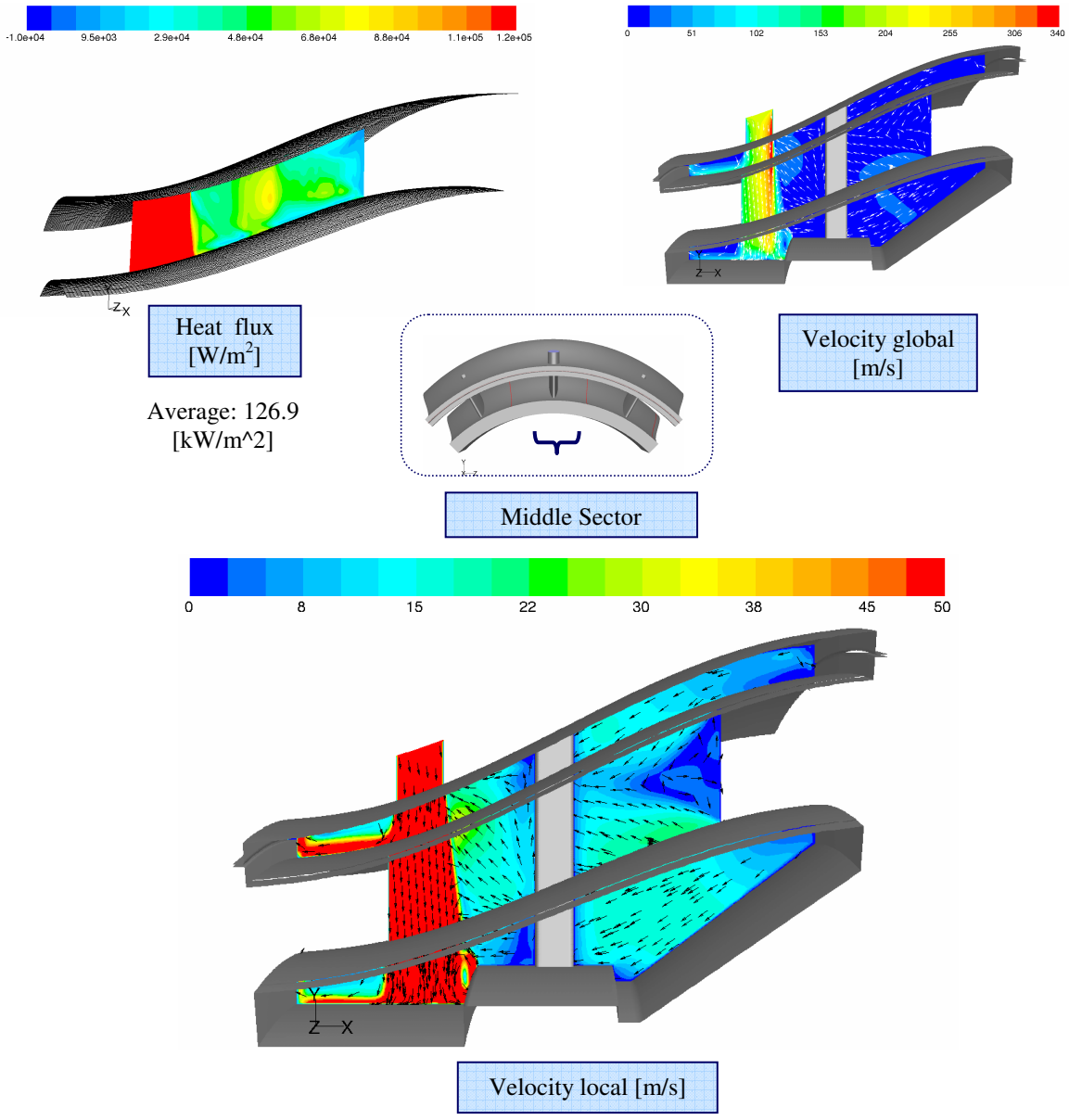

Figure 39: Heat flux, global and local velocity field at the intersection of the middle sector.

Investigating the flow field throughout the vanes plotted in Figure 39 yields a lot of information of how the flow behaves from the top of the inlet boss, through the vane and

down to the inner cavity wall. The observed flow field agrees well as concluded from earlier analysis. The impinging jet is early observed together with the complex flow in the inner cavity. There are regions where the velocity magnitude is almost zero. Away from the impinging jet in the vane, the flow goes upward but there are also regions where the flow goes downward unlike the one-sector case studied above in section 5.2.5. The flow seems to go around the cold strut in the vane. Considering the heat flux only, one side view of the vane is presented because the other one shows a very similar pattern.

The results for the left vane plotted in Figure 40 are quite different. Firstly the heat flux on the vane wall is not symmetric along the centreline as observed below. Further it is obvious that the flow goes up through and along the vane. Still there are large differences in the heat flux which can damage the material.

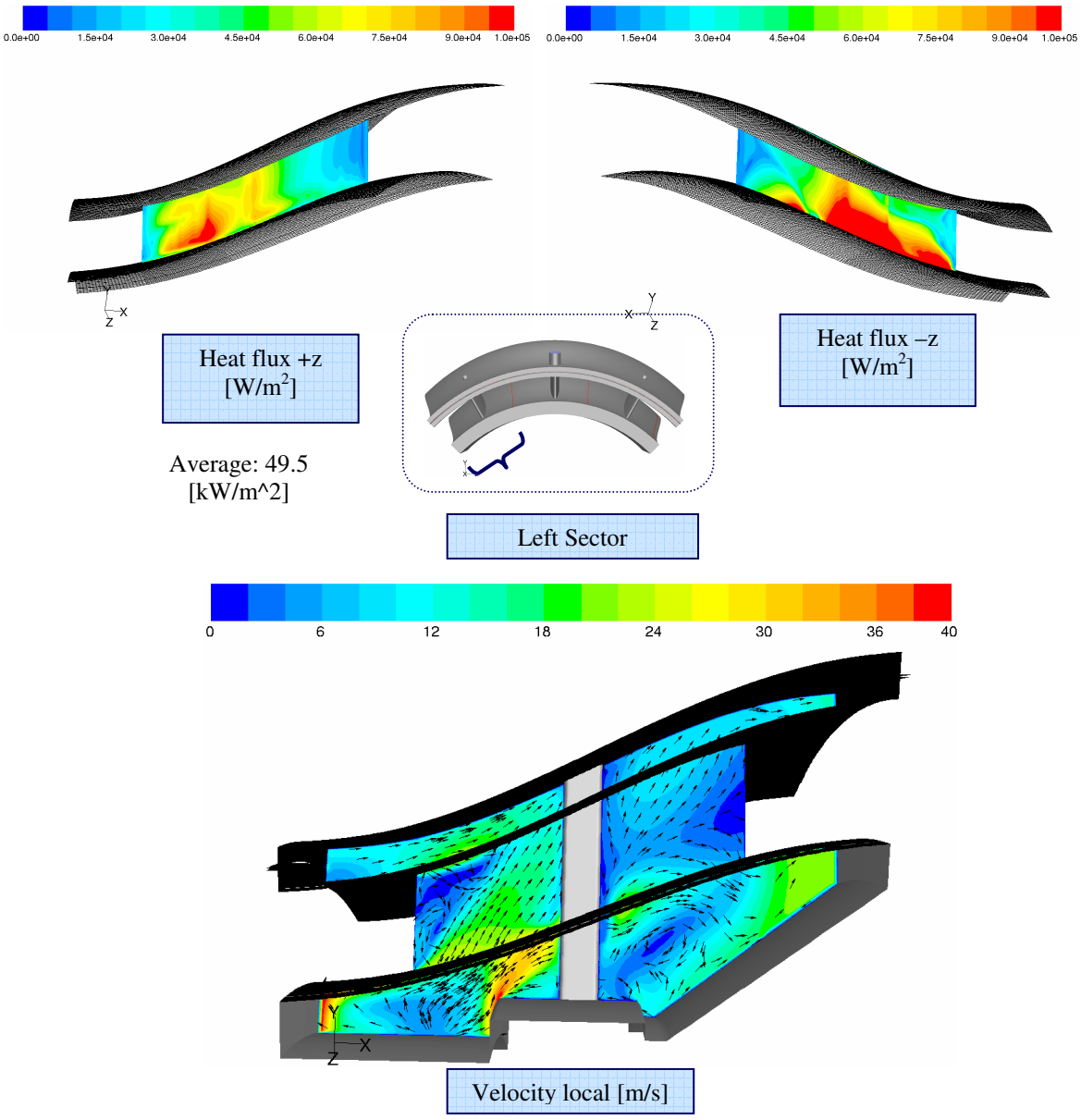

Figure 40: Heat flux and local velocity field at the intersection of the left sector.

The above discussion agrees well with the right sector vane shown below in Figure 41. However the flow is more complex in the inner cavity. The heat flux on the wall of the vane shown in +z view is more intensive than the other side. This is probably because the flow finds it easier to move down to the outer-side leakage than up to the sector-sector leakage between the centre and the right sector in the outer cavity. This is also the case in the left sector but along the corresponding leakages. This analysis has shown many interesting results that have to be included in the design process of the cooling mechanism.

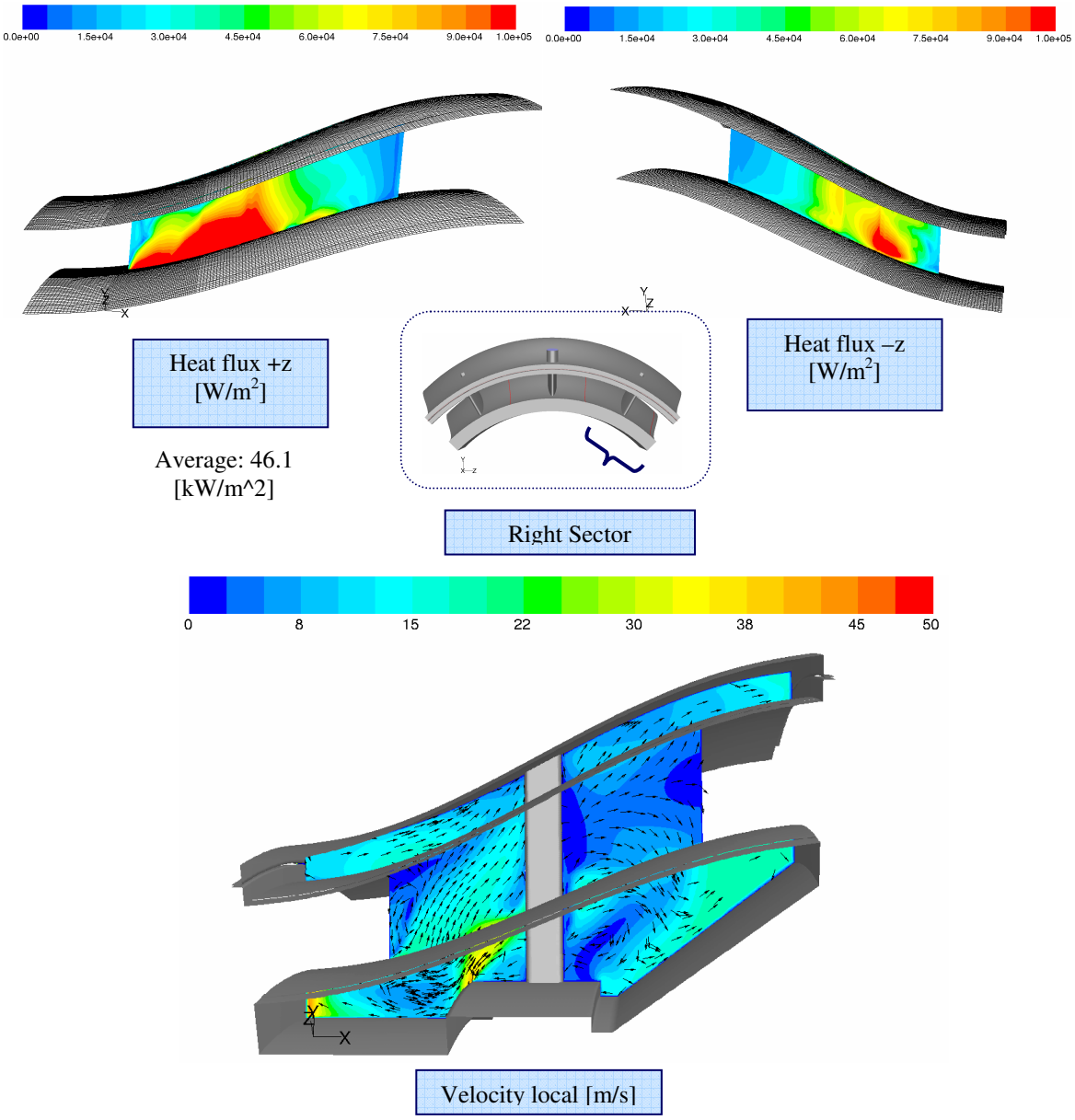

Figure 41: Heat flux and local velocity field at the intersection of the right sector.

5.4 Different cooling mass flows

5.4.1 Introduction

The influence of different cooling mass flow rates through the inlet is of high importance when doing a fluid network for a finite element thermal analysis. It is important that the overall flow pattern is not dependent on the used mass flow rate. In order to investigate this dependence, several cases with different mass flow rates were set up, solved and analyzed. Table 6 presents the different cases, the mass flow rates used and the corresponding area average inlet velocity. The mass flow rate is stated as percentage of the gas path mass flow.

CASE	Mass flux [%]	Inlet vel. [m/s]
A	0,34	106
B	0,61	207
C	0,76	237
D	1,07	336
E	1,44	451
F	1,95	611

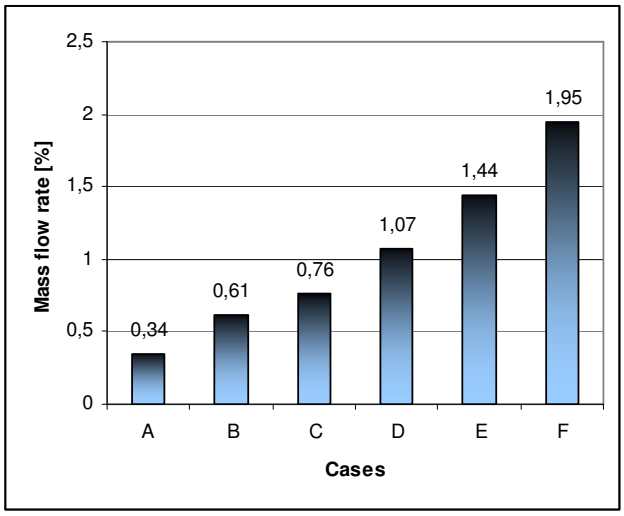

Table 6: Different cooling mass flow rates.

The analysis done includes a comparison of the flow fields in a chosen evaluation surface and computing the average HTC vs. mass flow rate. The HTC is computed as

$$h = \frac{q_w}{\Delta T}$$

where ΔT is the temperature difference between the considered wall and the temperature on the evaluation surface of that wall. The temperature on the wall is set to a constant value and on the surface the mass-weighted average value is used. It is interesting to see if there is a correlation for HTC. This is what one expects and the next section gives the answer.

5.4.2 Results and discussion

The velocity field, air temperature and wall heat flux is used as analysis parameters for this section as for earlier sections. First it is of importance to compare the velocity for different mass flow rates and conclude if the flow is different. Figure 42 below presents the velocity fields for two different mass flow rates, 0.34% and 1.44%. The other ones do not differ so much from these two chosen and consequently are not included in the report.

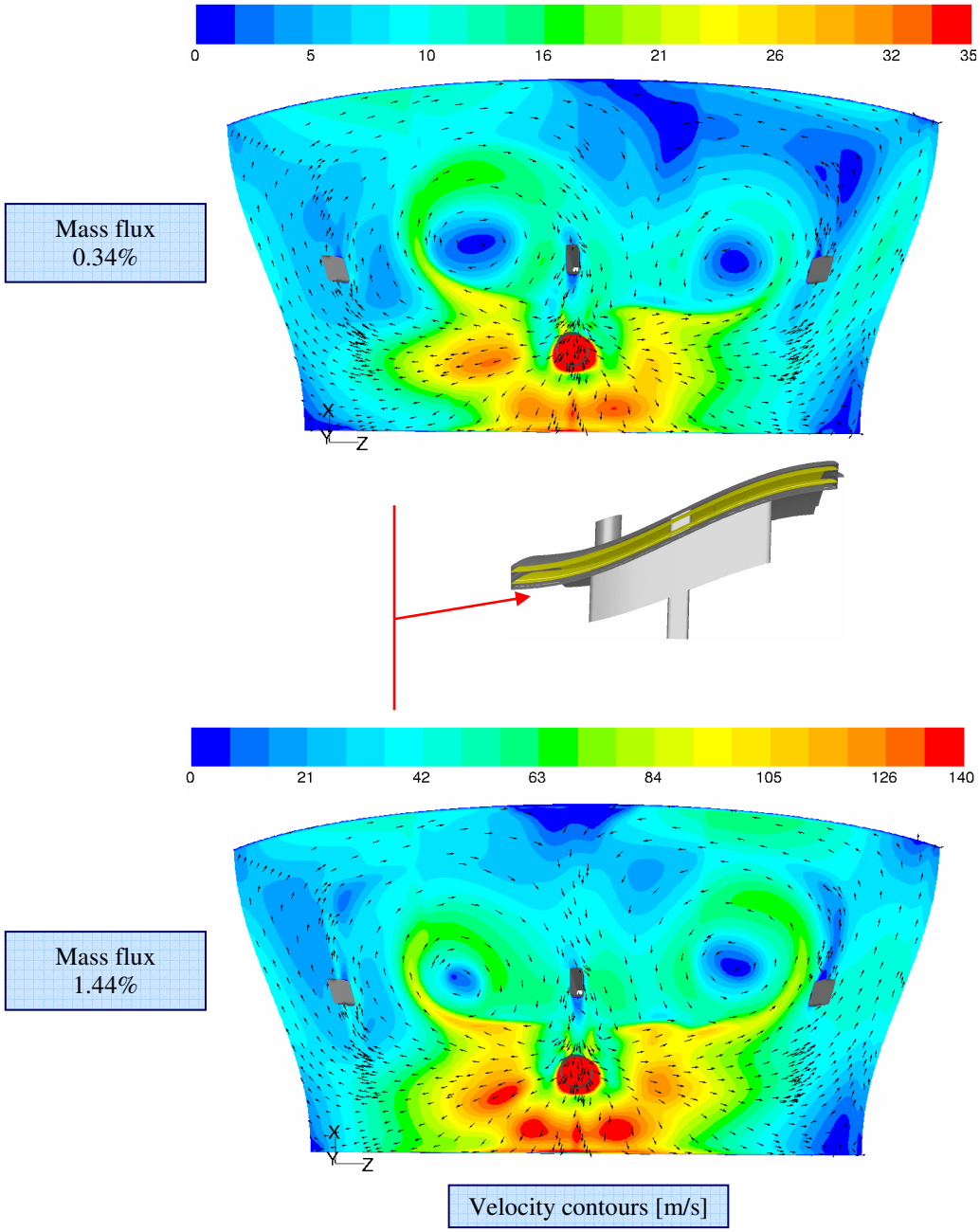

Figure 42: Velocity fields near the shroud at two different mass flow rates.

First let's consider the magnitude of the velocity. There is large difference as expected but the regions where the high velocity exists differ only slightly. Especially the magnitude of the right vortex, for the case of low mass flow rate the vortex is small but it is quite large in the case of high mass flow rate. Further the flow seems to be spread more intensively to the front side of the component for high mass flow rates which is of course expected. Secondly consider the direction of the flow in different regions. Fortunately the flow picture is more or less identical for these mass flow rates and this ensures that one do not need to do a complex thermal analysis which takes care of different mass flow

rates and their different flow patterns. Instead it is enough to have a correlation for HTC that is presented further on.

The temperature field and the wall heat flux for these different mass flow rates are presented below in Figure 43. Considering the net average of wall heat flux, it is more than doubled when the mass flow is about 4 times larger. However the overall picture agrees well with earlier obtained results and this is also valid for the temperature field on the evaluation surface.

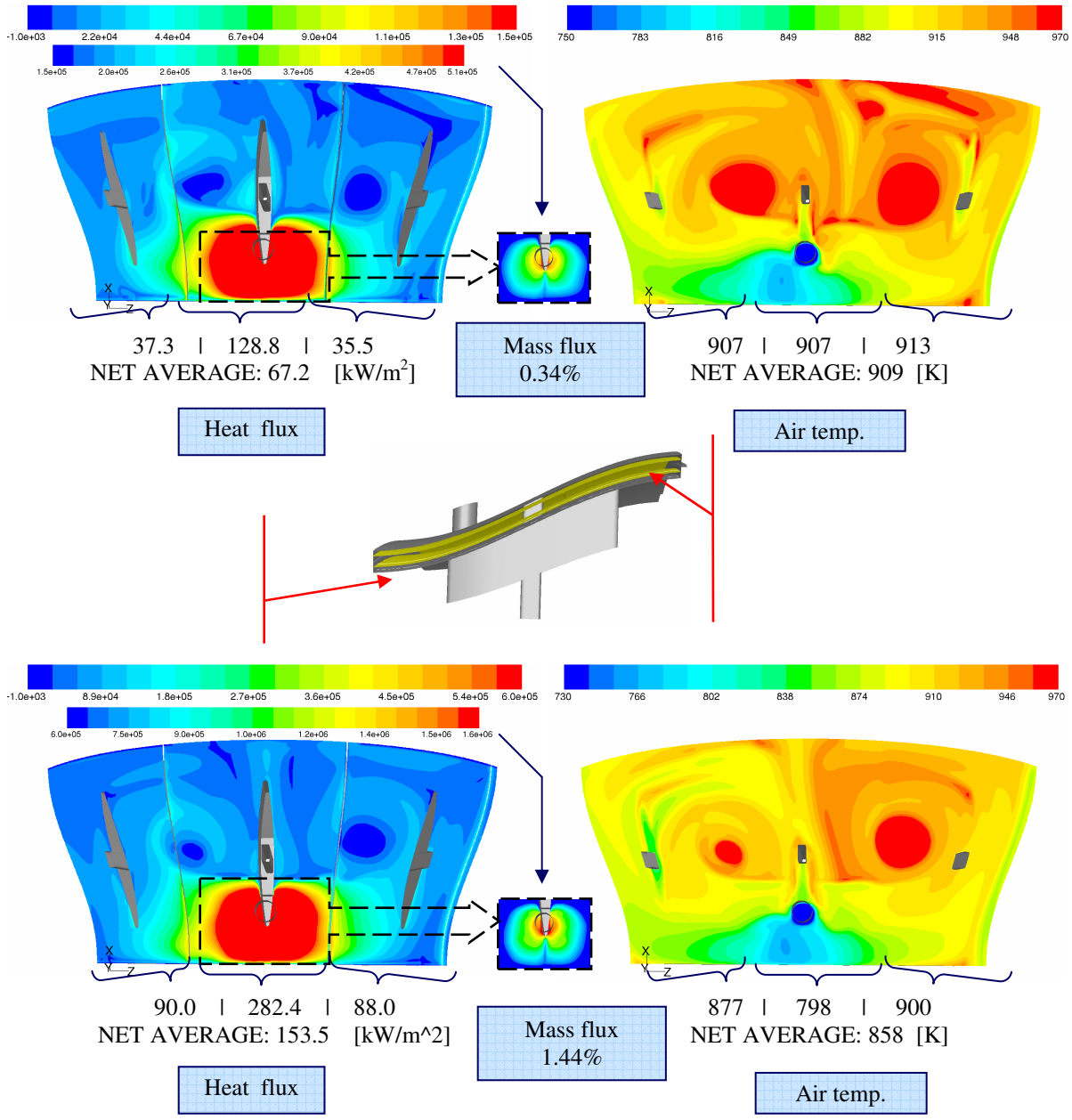

Figure 43: Heat flux and air temperature near the shroud for different mass flow rates.

The average HTC value for the external case, shroud and hub are presented in table 7. A non-linear polynomial fit function is applied to each wall and is plotted in Figure 44.

EXTERNAL CASE	Mass flow rate [%]	HTC [W/m^{2}K]
	0,34	16,09
	0,61	35,18
	0,76	43,63
	1,07	68,14
	1,44	103,69
	1,95	142,02

SHROUD	Mass flow rate [%]	HTC [W/m^{2}K]
	0,34	111,28
	0,61	178,37
	0,76	222,74
	1,07	309,92
	1,44	403,77
	1,95	524,43

HUB	Mass flow rate [%]	HTC [W/m^{2}K]
	0,34	86,38
	0,61	162,75
	0,76	180,82
	1,07	248,92
	1,44	325,14
	1,95	436,06

Table 7: Computed average HTC.

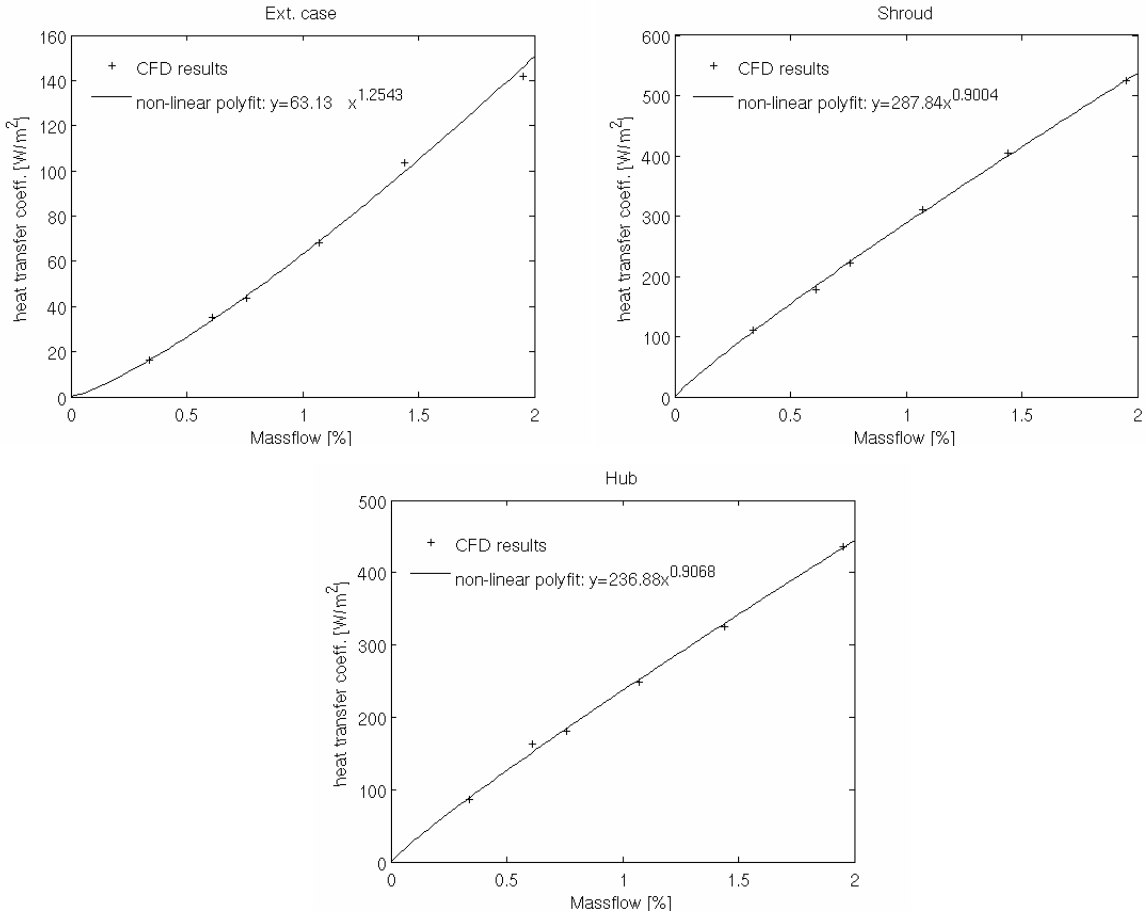

Figure 44: Correlation for HTC vs. mass flow rate for external case, shroud and hub.

The results for the hub and shroud are quite consistent with known standard correlations, for the external case the exponent is larger than 1 which is slightly higher than expected.

5.5 Convective walls with shell conduction

5.5.1 Introduction

The problems during the work with the conjugated CFD model presented in chapter 6 led to finding another easier way to predict the wall temperatures. All the above analysis is done with constant wall temperatures. This assumption is of course not true in a real condition. The wall temperature is varying and depends on both the duct flow and the cooling flow exposed on the wall. Thermal conduction exists in the material which affects the temperature distribution. To further improve the analysis strategy and to be able to predict the wall temperature, walls with shell conduction are applied to the shroud, vanes and the hub with a backside convective BC. This feature allows us to include external heat transfer effects from the hot duct flow. Four different parameters have to be set in the BC of the considered walls in order to achieve heat transfer through it, i.e. heat convection.

1. The HTC
2. The free stream temperature, T_{bulk}
3. The wall thickness
4. The thermal conductivity of the wall material, λ

The first two properties should be given from the external analysis done, however for simplicity average values from the analysis performed in the previous sections are set and the third property is typically chosen. Heat is not only convected through the wall, there is also heat conduction along the wall which is also considered. This feature can also be set in the BC. FLUENT takes also care of heat conduction along connected walls. This is a good property when analyzing the temperature of the vane that is connected to the shroud and the hub.

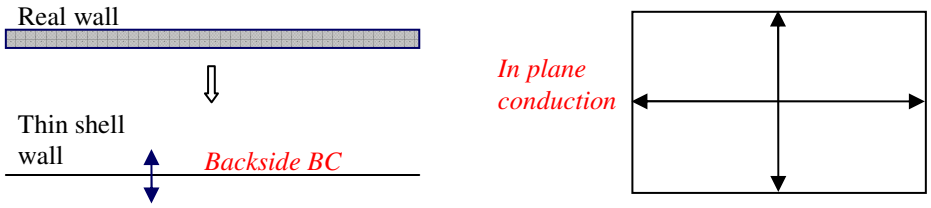

Figure 44: A schematic picture of the used BC for the thin shell model.

5.5.2 Results and discussion

The solution procedure is quite easy for this case. It takes about 1500 iterations for convergence and it can be run over the night. Below in Figure 46 the same pattern of analysis is applied. The air temperature and the velocity field are plotted on the evaluation surface for the considered wall. The wall temperature is plotted below and there is a few interesting things observed. As expected from previous analysis, the wall temperature is non-uniform throughout the shroud wall. The temperature varies between about 900-1180[K] which is a wide range. Further it is observable how the cooling is conducted from the impinging region but does not reach the whole material. The other

two plots is however almost identical with earlier obtained results. The wall temperature is of course high and the existing variations can damage the material.

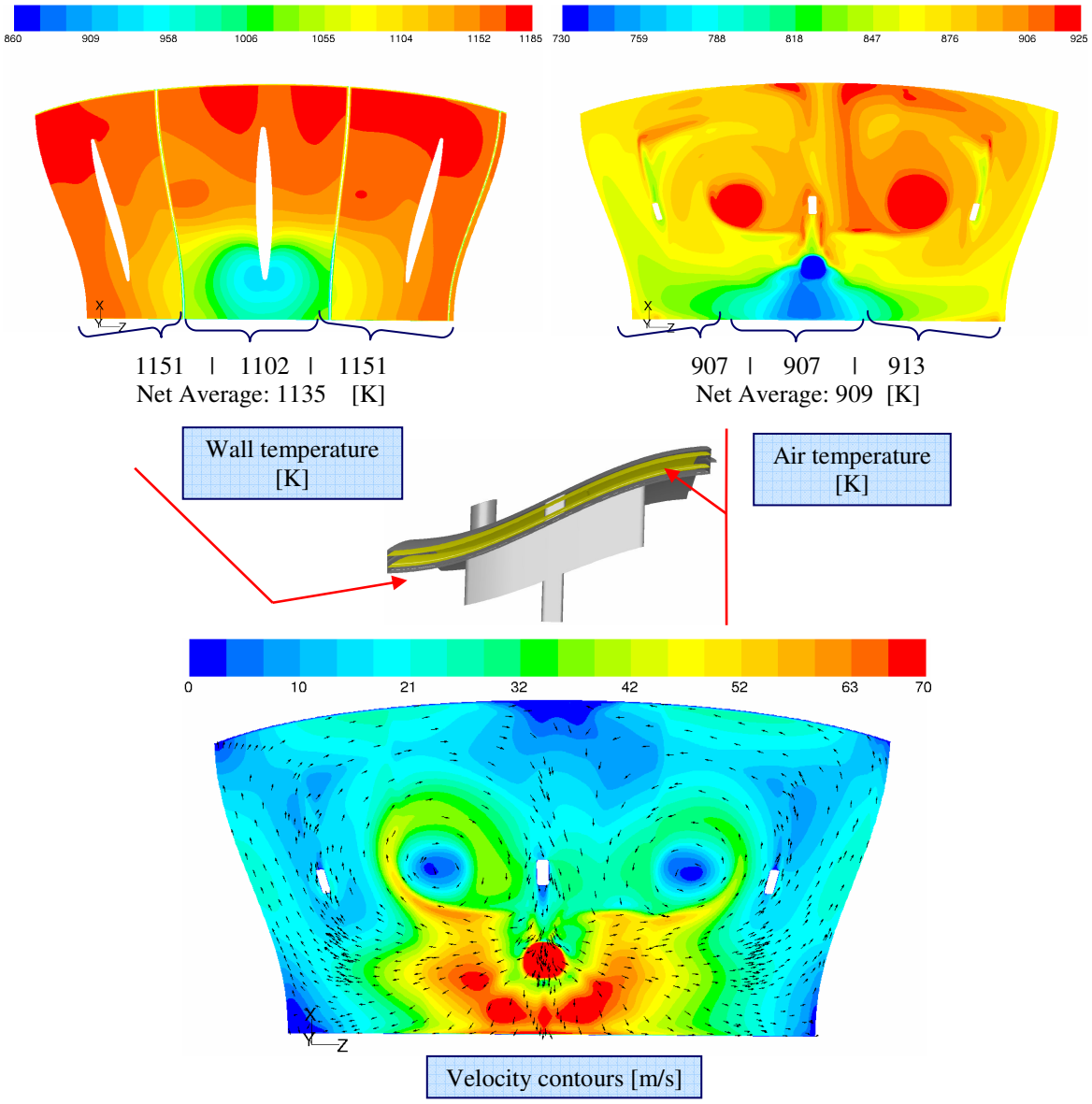

Figure 46: Wall temperature, air temperature and velocity field for the shroud.

Considering the hub in Figure 47, the discussion above is valid. However there is a lower temperature difference, the range is now about 1050-1170[K]. It is noticeable that the area of low temperature is larger than on the shroud and this is of course good. The temperature picture agrees well with corresponding air temperature and velocity field at the evaluation surface.

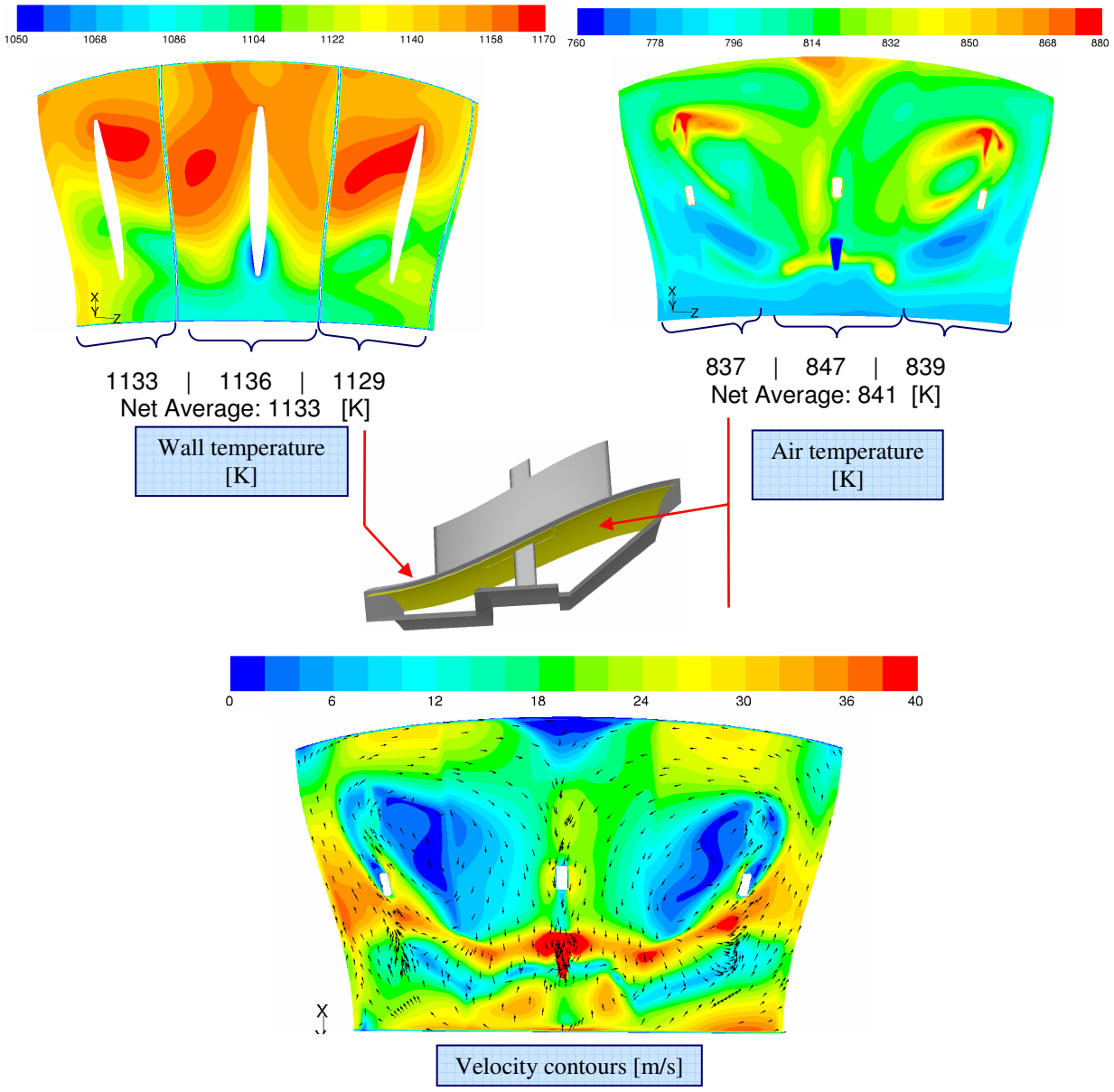

Figure 47: Wall temperature, air temperature and velocity field for the hub.

This discussion completes this section and the conclusions can be found later in this thesis. One important conclusion is that this analysis method is very good and effective for future work.

6 Conjugated model

6.1 Introduction

The last part in this thesis work is the conjugated model which is the external and the internal flow integrated together. Before the start of the building of the conjugated model, we were very sceptical to success with the geometry building and meshing due to the complexity. However it ended with success despite the many difficulties encountered. The aim of this model is to find the relation between the fluid flow, the heat transfer and the temperature of the walls. This is especially interesting since the cooling flow in the internal model gives rise to unequal cooling of the surfaces. Leakage along the hub and shroud are also included. From the beginning it was aimed to have leakage between the external case and the shroud, both along the front and back side. But to achieve a converged solution is extremely time-consuming and therefore these are not included.

6.2 Geometry and mesh

The geometry used is shown in Figure 48.

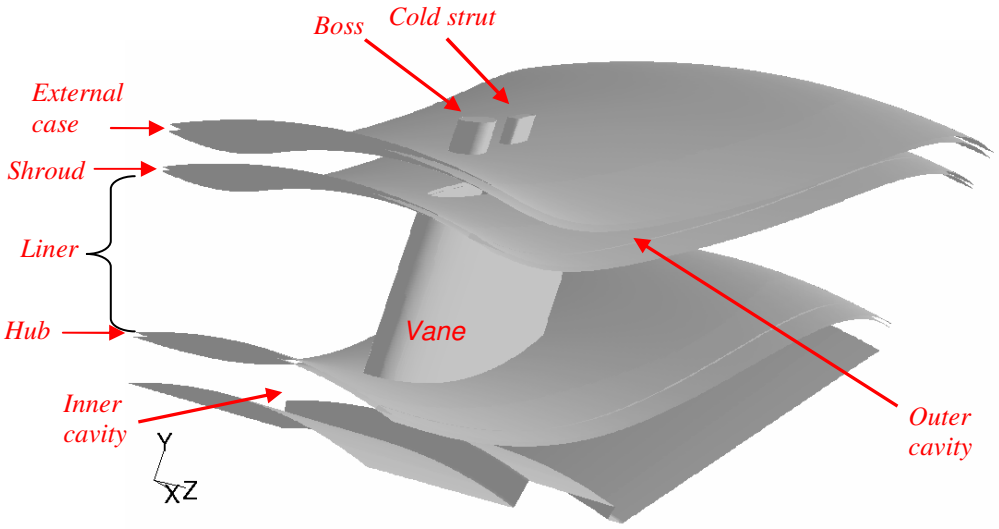

Figure 48: The conjugated geometry.

The duct used is the same as for the AITEB2 configuration. But the difference is due to the vane which has a NACA[2]-4 profile. One of the big challenges of this complex geometry structure is to obtain a fine mesh and simultaneously reduce the number of cells. The final mesh contains 4 400 000 cells, see Figure 49, and the skewness is below 0.86.

[2] National Advisory Committee for Aeronautics

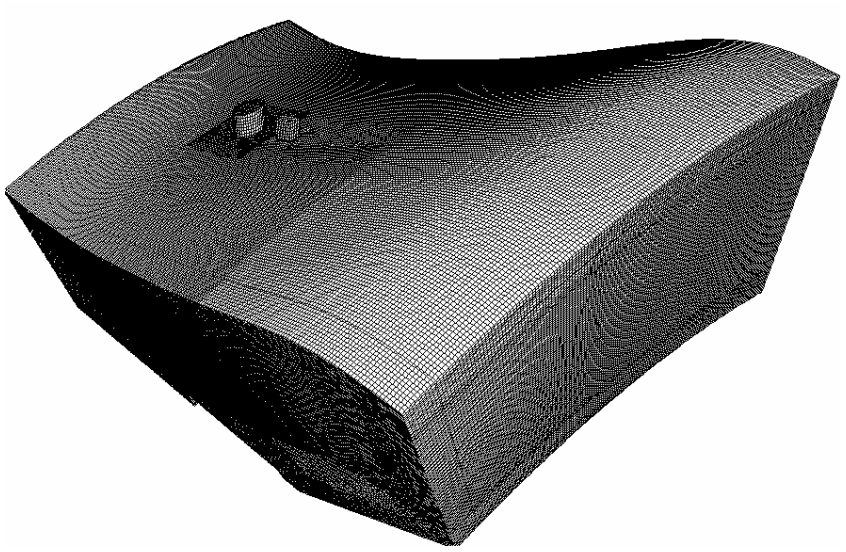

Figure 49: The hybrid hexa- and tetra-mesh.

Figure 50 shows the different parts of the conjugated model. Since the periodic BC is applied, the number of vanes is 12. One sector represents 30 degrees. As is mentioned earlier, the leakage above the inlet and outlet duct isn't included.

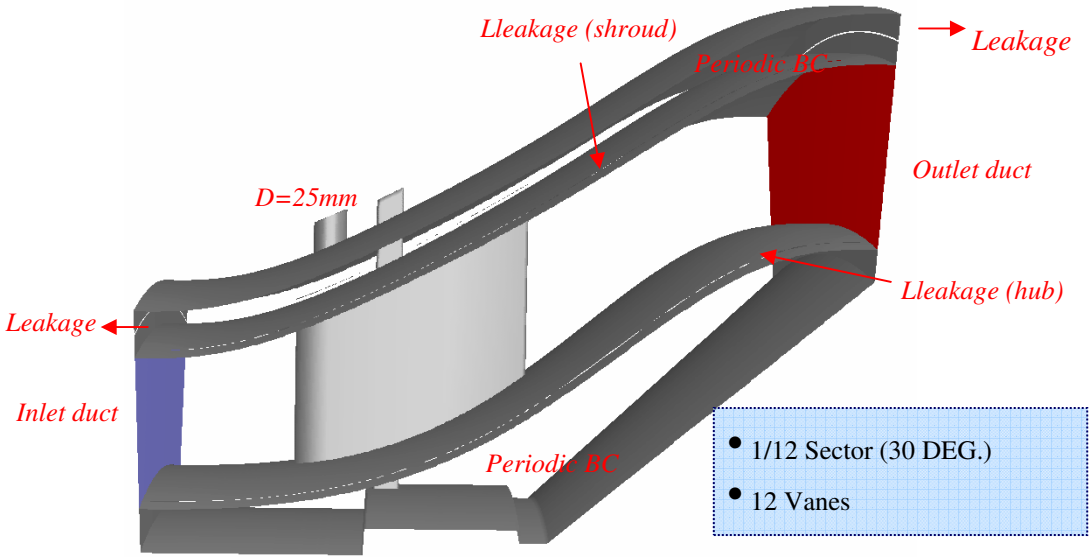

Figure 50: Differents parts of the conjugated model.

6.3 Boundary conditions

The BC for the external case is set to a wall with a constant temperature of 900[K]. The cooling flow from the inlet boss, has a temperature of 700[K] and the duct flow has a temperature of 1200[K]. The rest of the walls are coupled together to achieve the metal temperature and the surface heat flux over the entire domain. In order to achieve a mass flow of around 7[kg/s] for each sector an iteration process is made to adjust pressure difference between the inlet and outlet of the duct. After this iteration process the cooling flow is released and a new iteration process starts to obtain the correct amount of cooling flow, which is 2% (0.135kg/s) of the inlet duct flow.

Figure 51 shows a summation of the used BC. It took around 10 days, with 8 processors, to obtain a converged solution. The problem is that one can't apply all BC settings together from the beginning of the iteration process because of the complexity, and consequently one has to divide up the iteration process in successive steps.

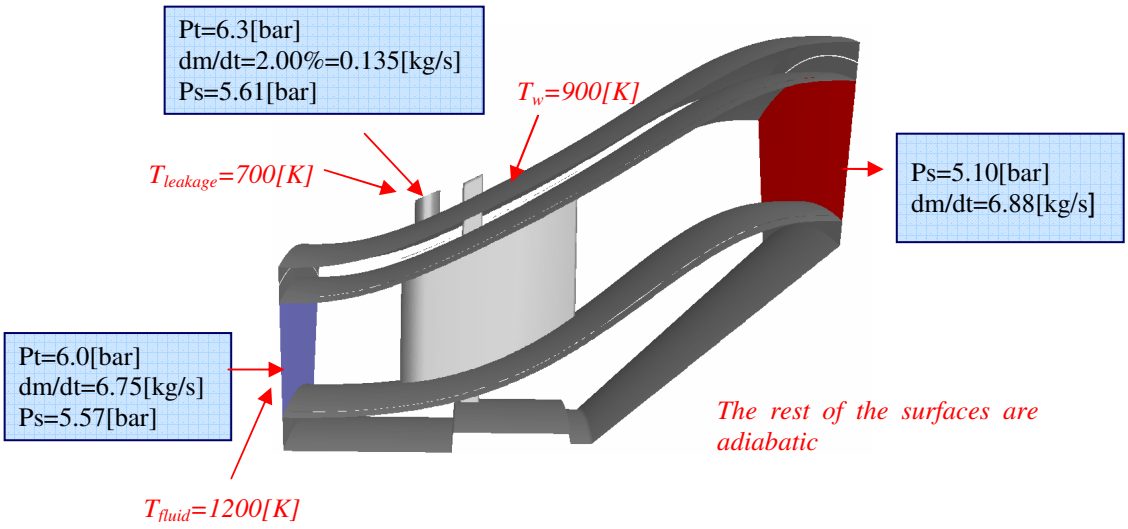

Figure 51: BCs of the conjugated model.

6.4 Results and discussion

From the beginning it wasn't aimed to have so much cooling flow as 2%. The pressure difference and the mass flow are related, which implies that a given mass flow rate yields a given pressure difference. The problem is the fact that the leakage seals are wrongly designed since one loses too much mass flow through them. If using too small amount of cooling flow, the pressure in the outer cavity gets too low, and this causes the hot fluid from the duct to reach the cavity. This is of course very harmful for the material.

6.4.1 Static pressure

Figure 52 shows the static pressure at a periodic surface. The pressure difference along the hub and the shroud surfaces can be observed. Along the hub surface, near the region of the second bend, the static pressure has its minimum value. A similar picture is

obtained for the shroud, but here the static pressure has its minimum value around the first bend. These regions are influenced by an adverse pressure gradient and consequently are the regions where the risk for separation is highest.

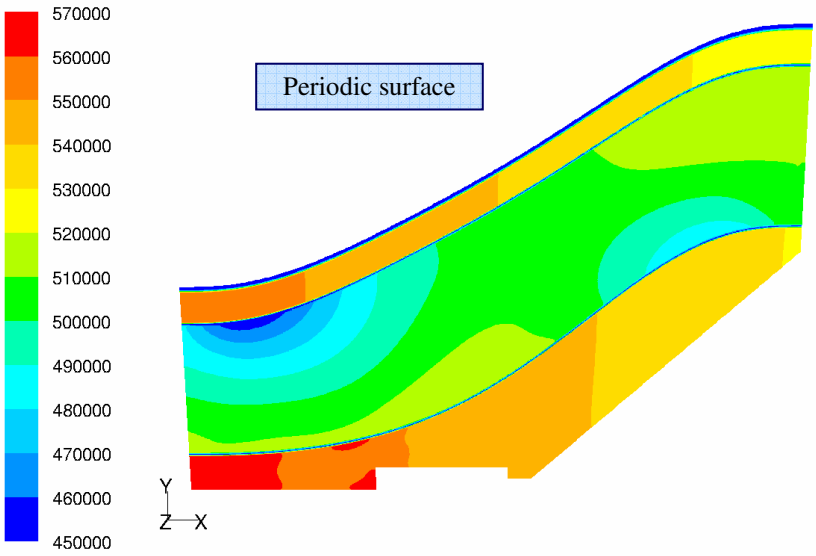

Figure 52: Contours of the static pressure [Pa] at the periodic surface.

Further one can observe that the static pressure in the inner and outer cavity is relatively uniform and independent of the static pressure distribution in the duct. This means that the cooling flow is the driving wheel of the complex and chaotic system within the cavities. One can also see that the inner cavity, close to the inlet, has the highest static pressure. This may be explained from the fact that the cooling flow is acting as an impinging jet and hits the inner cavity close to this region, see Figure 53. This implies that this region drives the flow back to the outer cavity.

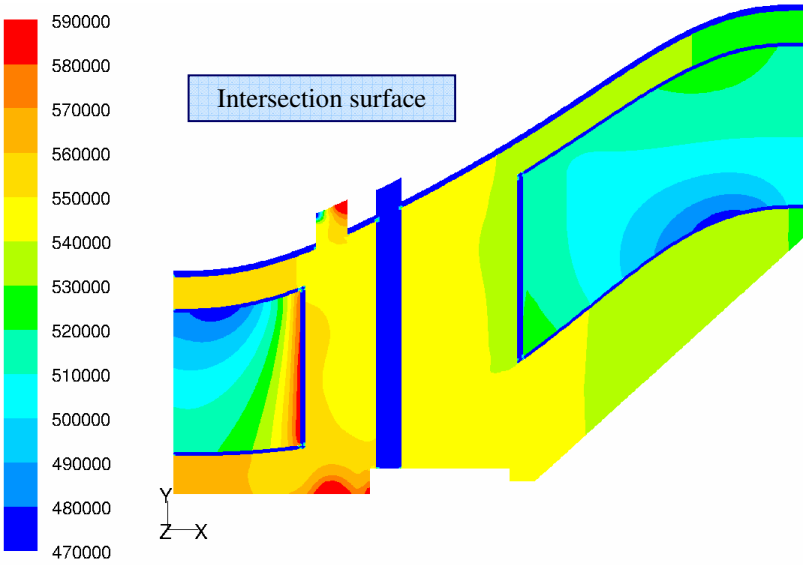

Figure 53: Contours of the static pressure [Pa] at the intersection surface.

6.4.2 Velocity and air temperature in the outer cavity

Figure 54 shows contours of the air temperature and velocity magnitude with velocity vectors included. The two evaluation surfaces are placed in the outer cavity. The temperature difference is very large, about 240[K]. The highest temperature occurs in the region close to the outlet. One can observe from the velocity contours that a vortex is created close to the outlet, which gives rise to the high temperature. It's clear that the flow pattern is very complex and chaotic. It's also clear that the temperature is low around the cold strut since the cooling flow hasn't yet gets mixed.

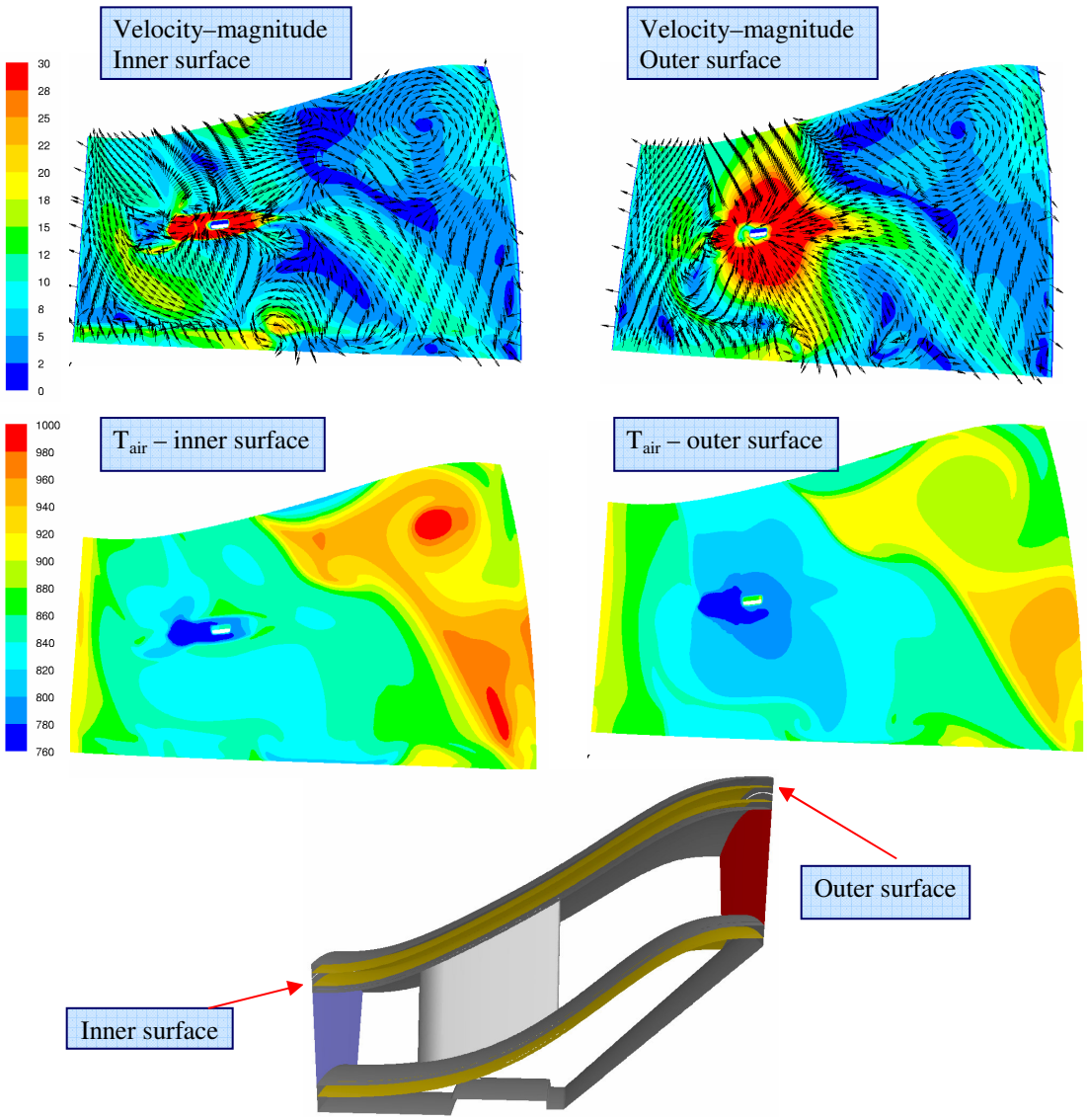

Figure 54: Contours of the wall temperature [K] and velocity [m/s] along the evaluation surfaces.

6.4.3 Velocity and air temperature at the intersection surface

Figure 55 shows contours of the velocity magnitude and air temperature. The velocity vectors show that the flow pattern is highly complex, especially the flow in the inner and outer cavity where a lot of vortices are created. It's also clear from the figure that the cooling flow acts as an impinging jet towards the inner cavity. The contour of the air temperature shows clearly how the cooling flow is propagating out in the domain.

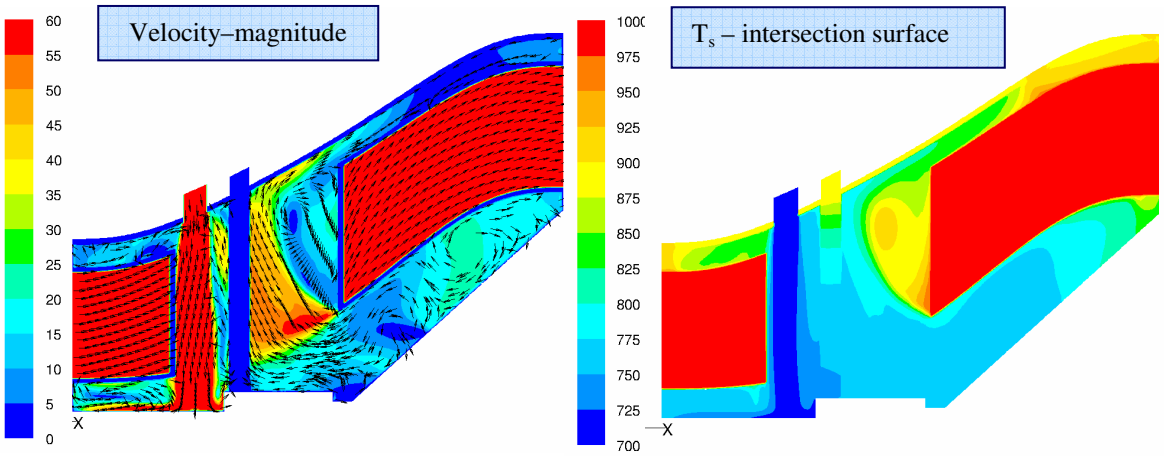

Figure 55: Contours of the air temperature [K] and velocity [m/s] at the intersection surface.

6.4.4 Wall temperatures and surface heat flux

Figure 56 shows the wall temperatures and the heat flux on different walls in the TMS, the external case, the shroud and the hub. The hub possesses quite large temperature differences, around 200[K]. The temperature distribution results are quite obvious, low temperature around the vane and higher temperature along the rest of the surfaces, since the cooling flow is impinging at the inner cavity and then pushes out towards the periodic faces, see Figure 57.

If going further on and looking at the shroud surfaces in the duct, it is obvious that the temperature is relatively uniform except in some regions. Lower temperature is obtained in the leading edge region of the vane. This can be explained from the fact that the inner structure of the vane has a lower temperature due to the cooling flow, which consequently implies that the attached flow along the outer side of the vane gets warmer in the axial direction. One interesting thing to point out is the fact that the cooling flow in the outer cavity reaches the duct, which means that no hot fluid, from the duct, reaches the outer cavity. This is of course of major important since the material in the outer cavity cannot resist the high temperature from the duct.

The plot in Figure 56 shows the wall temperature on the external case. The region around the boss is the coolest one and the cooling flow is propagating out from the boss. The region behind the vane where the vortex is placed to the right has high temperature. The surface heat fluxes are coupled to the temperatures and follow the same pattern. High

temperature implies high surface heat flux and the opposite. This is the case for all surfaces.

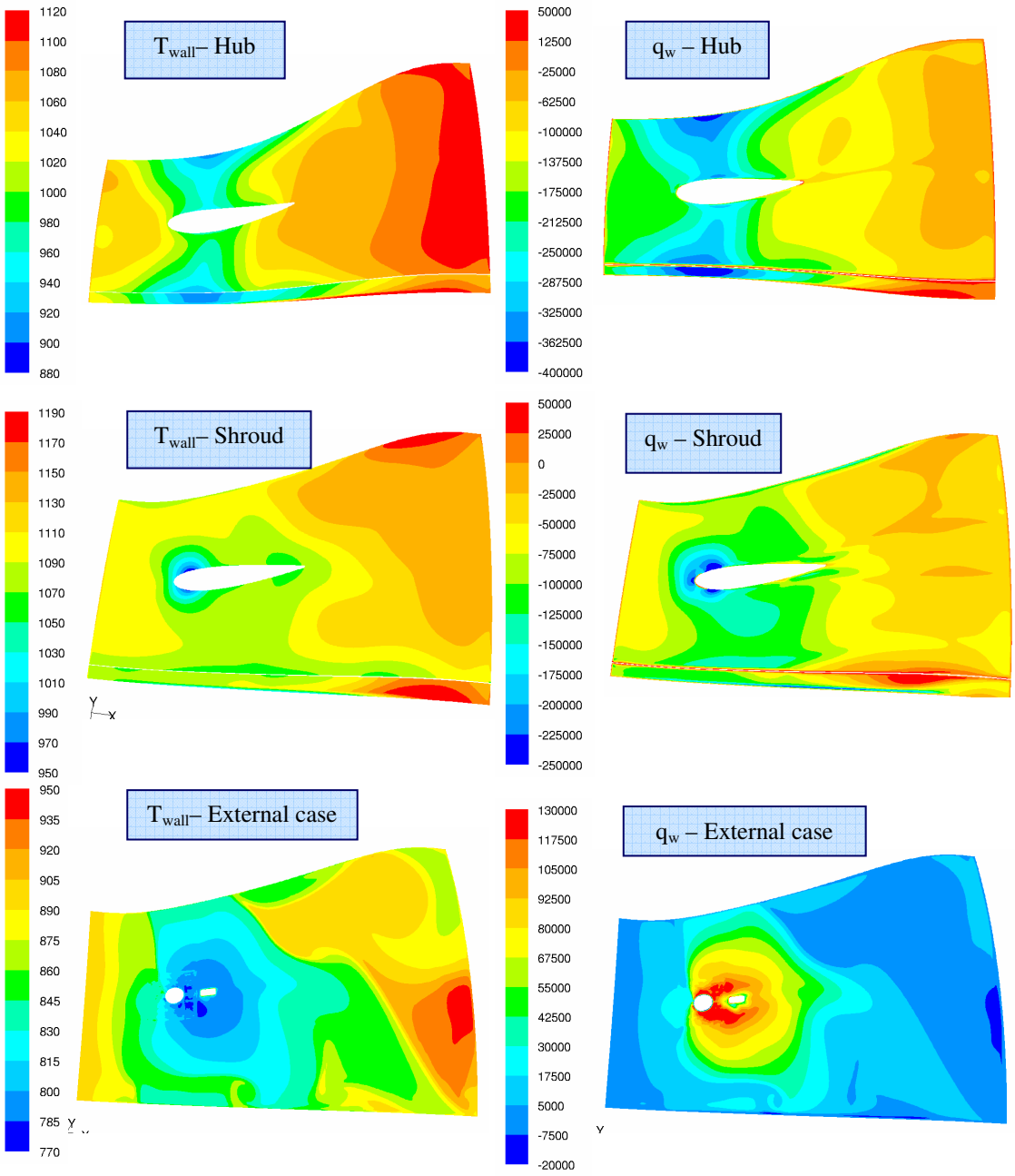

Figure 56: Contours of the wall temperatures [K] and surface heat flux [W/m^2].

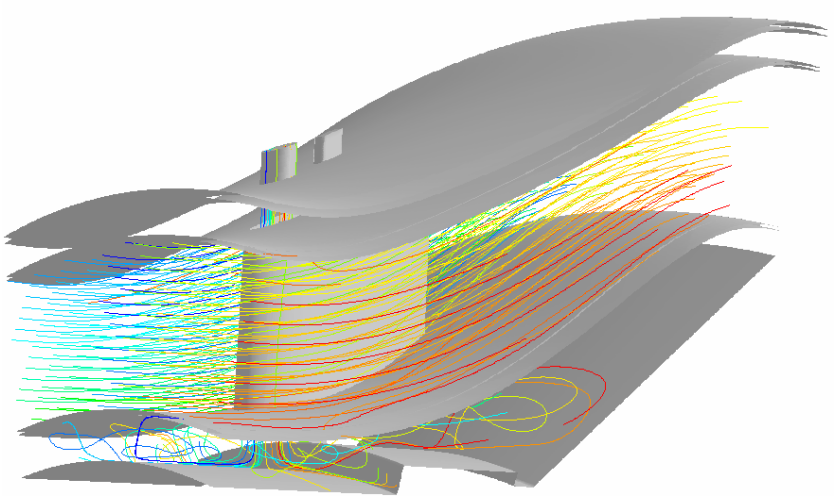

Figure 57: Pathlines released from cooling and duct inlet.

6.4.5 Wall temperature and heat flux for the vane

The contours of the wall temperature and heat flux for the vane can be seen in Figure 58. It's clear that the temperature differs a lot between the leading and trailing edge, i.e. around 200[K]. The temperature distribution is relatively symmetric considering the pressure and suction side of the vane. The heat flux follows the same pattern. The heat flux and the temperature are very high around the trailing edge of the vane.

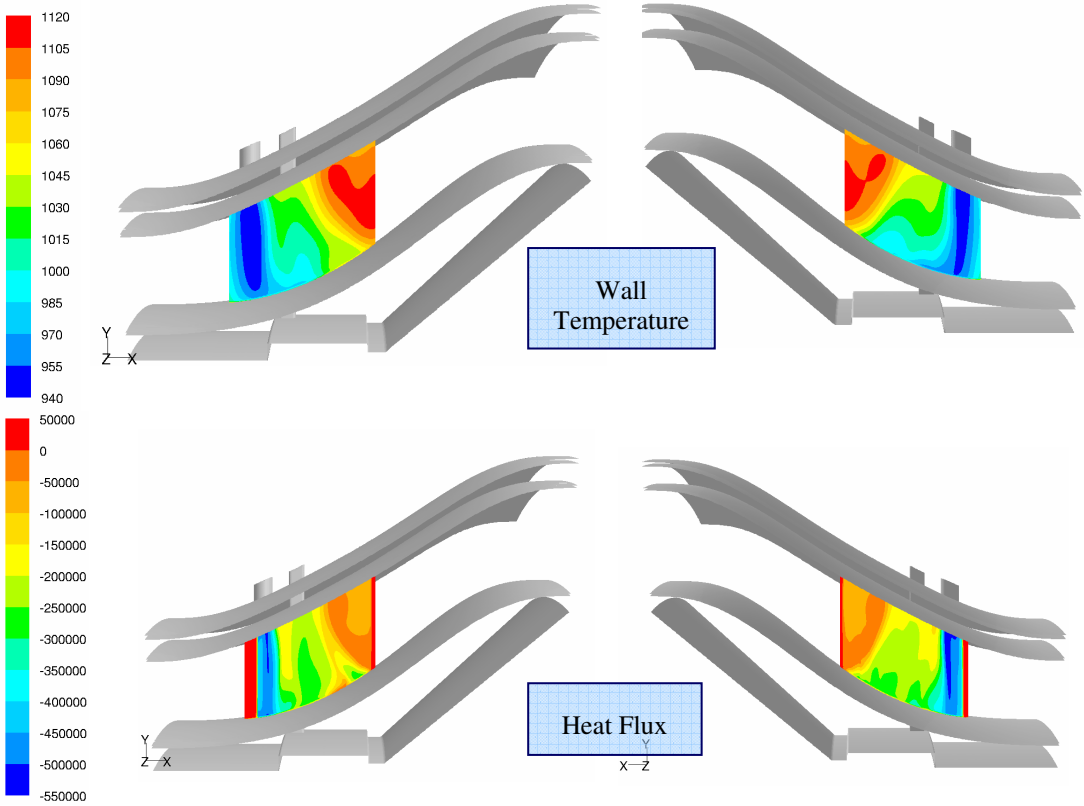

Figure 58: Wall temperatures [K] and heat flux [W/m^2] considering the warm structures of the vane.

7 Conclusions

Considering the external turbine duct, the flow field shows high complexity and strong secondary flow effects. A comparison between 2D and 3D heat transfer results shows that the 3D-effects are significant and the results show no big dependency of the used turbulence model. A comparison of the CFD heat transfer results and a standard flat plate correlation shows reasonable agreement. The leading edge of the vane is the most exposed region of hot gases and consequently has the highest HTC.

The structured approach using the Cooper tool is effective when meshing such complex geometries. This approach is applied to the internal cooling and conjugated model. The mesh sensitivity investigation shows that the results are mesh independent and that the mesh is can be made coarser without losing any information. The internal cooling flow is chaotic and complex. It is further highly dependent of the inlet conditions applied. The heat transfer within the TMS is widely non-uniform and there is a strong coupling between the flow field, air temperature, heat flux and wall temperature. The flow pattern is uniform according to different mass flow rates of the cooling flow applied. The heat transfer is scaled by the used mass flow rate.

The thin shell method is easy to implement and run, it gives also good control of the leakage flows. The conjugated model is even more complex to build up since the gas path is integrated with the internal cooling structure. It is however almost impossible to implement a three-sector model since the mesh becomes too large. It is also difficult to model the seals. The conjugated model captures however the interaction between the internal cooling and external gas flows.

The difficulties encountered in the conjugated model led us to run an internal cooling model with thin shell and convective BC. The later method is highly recommended to use in order to predict wall temperature within the TMS component.

GAMBIT has significant problems to generate unstructured tetra-meshes. It is even impossible if different sizing functions are used at the faces of a volume. Through cooperation with the FLUENT support center, an improved source code of GAMBIT has been implemented by them. The improvement will be included in the next version of GAMBIT.

8 Future work

Recommendations for future study include a validation test case of impinging jet flow. This is in order to validate the internal cooling flow. The chosen inlet feeding system of the cooling flow is obviously not optimized. More sophisticated concepts are needed in order to achieve a uniform cooling.

The modelling of seals towards the turbine duct has to be improved. Varying static pressure on the leakages and realistic pressure losses should be implemented e.g. using the outflow ventilation BC in FLUENT. A varying HTC distribution for the thin shell model should be implemented.

Considering the internal cooling flow model, find an appropriate level of the mesh size and a more effective meshing tool should be used.

References

Books

[1] Frank P. Incropera & David P. Dewitt, (2002), *Fundamentals of Heat and Mass Transfer,* 5th edition.

[2] David C. Wilcox, (2000), *Turbulence Modeling for CFD,* 2nd edition, DCW Industries Inc.

[3] H K Versteeg & W Malalasekera, (1995), *An introduction to Computational Fluid Dynamics,*

[4] Bejan (2003), Adrian & Kraus, Allan D. *Heat Transfer Handbook.*

[5] Frank M.White (2003), *Fluid Mechanics,* 5th edition.

[6] John D.Anderson Jr., (1990), *Modern Compressible Flow,* 2nd edition.

[7] Ira H.Abbott & Albert E.Von Doenhoff (1959), *Theory of wing sections,* New Ed edition

[8] Fluent manual.

[9] Ansys ICEM CFD manual.

Papers

[10] Wallin Fredrik & Wikström Peter (2002), Luleå University of Technology, *Temperature Calculations on a Turbine Center Frame.*

[11] Wallin Fredrik (2006), *Aerodynamik Design and Optimization of Intermidiate Ducts for High By-pass Ratio Jet Engines,* Lic. Chalmers University of technology, Gothenburg

[12] Carlos Arroyo, (2006), *Design of a Large-Scale Experimental Facility for the Study of the Flow in Intermediate Turbine Ducts,* Lic. Chalmers University of technology, Gothenburg

[13] Göttlich Emil, Malzacher Franz, Heitmeir Franz & Marn Andreas, (2005), Graz University of Technology, *Adaption of a Transonic Test Turbine Facility for Experimental Investigation of Turbine Ducts Flows*

[14] G Norris & R G Dominy, (1997), University of Durham, *Diffusion rate influences on inter-turbine diffusers.*

[15] C.R. Wang, C.E. Towne, S.A. Hippensteele & P.E. Poinsatte, (1997), Lewis Research Center Cleveland, Ohio, *Heat Transfer Computations of Internal Duct Flows With Combined Hydraulic and Thermal Developing Length,* National Aeronautics and Space Administration, AIAA-97-2486

[16] Jan A. Visser, (2000), University of Pretoria, South Africa, *A simplified equation to predict heat transfer in an internal duct of a gas turbine nozzle guide vane,* Communications in numerical methods in engineering, vol.16:637-648

[17] R.G. Dominay & D.A. Kirkhamn, (1996), University of Durham, United Kingdom, *The Influence of Blade Wakes on the Performance of Interturbine Diffusers,* Journal of Turbo machinery vol.118:347-352

[18] R.G. Dominay & D.A. Kirkhamn, (1995), University of Durham, United Kingdom, *The Influence of Swirl on the Performance of Inter-Turbine Diffusers,* Von Berichte Nr. 1186:107-122

Private communication

[19] Hans Abrahamsson – Volvo Aero Corporation, Trollhättan, Sweden

Appendix Contents

Appendix A - Theory analysis

A1 - Basic Fluid Dynamics

A1.1 - Conservation of mass

The continuity equation relies on the physical principle of conservation of mass. It states that the time rate of change of mass of a material region (MR) is zero. The mass of a material region is

$$\int \rho dV$$

Conservation of mass requires

$$\frac{dM_{MR}}{dt} = \frac{d}{dt}\int_{MR} \rho \, dV = 0$$

$$= [Leibnitz's\ theorem] = \int_{MR} \frac{\partial \rho}{\partial t}\, dV + \int_{MR} n_i v_i \rho \, dS = 0$$

$$= [Gauss\ theorem] = \int_{MR} [\frac{\partial \rho}{\partial t} + \partial_i(\rho v_i)]\, dV = 0$$

$$= [Arbitrary\ region] = \frac{\partial \rho}{\partial t} + \partial_i(\rho v_i) = 0$$

A1.2 - Conservation of momentum

The momentum equations rely on the physical principle of conservation of linear momentum. It states that the time rate of change of the momentum equals the sum of the total body forces and the total contact forces.

$$\frac{d}{dt}\int\int\int_{V(t)} \rho u_i \, dV = \int\int\int_{V(t)} \rho f_i \, dV + \int\int_{S(t)} t_i^n \, dA$$

$$\frac{d}{dt}\int\int\int_{V(t)} \rho u_i \, dV = [Reynolds\ Transport\ Theorem\ (RTT)] = \int\int\int_{V(t)} \left[\frac{D[\rho u_i]}{Dt} + \rho u_i \frac{\partial u_k}{\partial x_k}\right] dV$$

$$[Product\ rule\ +\ continuity\ eqn.]$$

$$\frac{D[\rho u_i]}{Dt} + \rho u_i \frac{\partial u_k}{\partial x_k} = \rho \frac{Du_i}{Dt} + u_i \frac{D\rho}{Dt} + \rho u_i \frac{\partial u_k}{\partial x_k} = \rho \frac{Du_i}{Dt} + u_i \left(\frac{D\rho}{Dt} + \rho \frac{\partial u_k}{\partial x_k}\right) = \rho \frac{Du_i}{Dt}$$

$$\frac{d}{dt}\int\int\int_{V(t)} \rho \frac{Du_i}{Dt}\, dV = \int\int\int_{V(t)} \rho f_i \, dV + \int\int_{S(t)} t_i^n \, dA =$$

$$= \frac{d}{dt}\int\int\int_{V(t)} \rho \frac{Du_i}{Dt}\, dV = \int\int\int_{V(t)} \rho f_i \, dV + \int\int_{S(t)} T_{ij} \cdot nj \, dA$$

Suppose we imagine a volume fixed in space, say V_s that instantaneously coincides with our material region

$$\int\int_{S(t)} T_{ij} \cdot nj \, dA = \int\int_{S_s} T_{ij} \cdot nj \, dA_s = [Divergencetheorem] = \int\int\int_{V_s} \frac{\partial T_{ij}}{\partial x_j}\, dV_s$$

This implies that

$$0 = \int\int\int_{V_s} \left[\rho \frac{Du_i}{Dt} - \rho \cdot f_i - \frac{\partial T_{ij}}{\partial x_j}\right] dV \Rightarrow \rho \frac{Du_i}{Dt} = \rho \cdot f_i + \frac{\partial T_{ij}}{\partial x_j} =$$
$$= \frac{\partial u_i}{\partial t} + u_j \frac{\partial u_i}{\partial x_j} = -\frac{\partial p}{\partial x_i} + \frac{1}{\rho}\frac{\partial T_{ij}}{\partial x_j}$$

The last term can be further expanded to obtain the equation found in chapter 2.1.

A2 - Compressible equations

A2.1 - Pressure

$$\frac{P_0}{P} = \left(1 + \frac{\gamma - 1}{2} M^2\right)^{\gamma/(\gamma-1)}$$

A2.2 - Temperature

$$\frac{T_0}{T} = 1 + \frac{\gamma - 1}{2} M^2$$

A2.3 - Density

$$\frac{\rho_0}{\rho} = \left(1 + \frac{\gamma - 1}{2} M^2\right)^{1/(\gamma-1)}$$

A2.4 - Ideal gas law

$$P = \rho R T$$

A3 - Turbulence

Turbulence is very important to consider since it is included in most engineering applications of flows. One can observe it everywhere (airplanes, smoke, nature etc.) but it is very difficult to understand. The state of the fluid motion that is characterized by random and chaotic three-dimensional vorticity is called turbulence. This means that velocity and all other flow properties vary in a random and chaotic way. Turbulence has a wide range of scales. Time and length scales of turbulence are represented by frequencies and wavelengths that are shown by a Fourier analysis of a turbulent-flow time history. Turbulence intensity is dominated by the large eddies, which is the energy containing scales. The small, dissipative, scales receive the energy from the big scales. This is actually the cascade process.

To deal with turbulence, it's preferable to decompose the instantaneous variables into a mean and a fluctuating part. The reason is due to solving the Navier-Stokes equations numerically efficiently, because it would require extremely fine resolution in time and space to resolve all turbulence scales.

The equation for the turbulent kinetic energy k is derived from the Navier-Stokes equation. That is relatively straightforward. When this is done, a number of new unknown terms are introduced. The production term, the turbulent diffusion term (pressure-velocity correlation and velocity correlation), viscous diffusion and the dissipation terms. The production term, P_k, is modelled as

$$P_k = \nu_t \left(\frac{\partial \bar{U}}{\partial y} \right)^2$$

where the Boussinesq assumption is used. The Boussinesq assumption is applied for eddy viscosity models, where the Reynolds stresses are linked to the velocity gradients via the turbulent viscosity. For the diffusion term, one uses a gradient hypothesis for the velocity correlations. One assumes that the term transports k from regions of high k to regions of low k. The pressure-velocity fluctuations are often negligible which has been proved by experiments.

The k-ε equation reads:

$$\frac{\partial}{\partial x_j}(\rho k U_j) = \frac{\partial}{\partial x_j}\left[\left(\frac{\mu_t}{\sigma_k} + \mu\right)\frac{\partial k}{\partial x_j}\right] + P_k - \rho\epsilon$$

$$\frac{\partial}{\partial x_j}(\rho \epsilon U_j) = \frac{\partial}{\partial x_j}\left[\left(\frac{\mu_t}{\sigma_\epsilon} + \mu\right)\frac{\partial \epsilon}{\partial x_j}\right] + \frac{\epsilon}{k}(c_1 P_k - c_2 \rho\epsilon)$$

where the convection term are to the left; diffusion, production and dissipation (transformation of mechanical energy into heat) to the right.

The advantage with the k-ε equation is that it's straightforward due to the use of an isotropic eddy viscosity, works quite well for many engineering applications and is relatively stable due to stabilizing second-order gradients in the mean-flow equation. One of the disadvantage is the isotropic assumption of the eddy viscosity, which implies that the normal stresses is not well predicted and consequently the model is not capable to account for curvature effects and stagnation flows.

The most common used turbulence model through this thesis work is the realizable k-epsilon model. With this model all normal stresses stays positive and the correlation coefficient for the shear stress does not exceed one. This is stated as:

$$\overline{u_i^2} \geq 0 \text{ for all } i$$

$$\frac{\overline{u_i u_j}}{\left(\overline{u_i^2}\,\overline{u_j^2}\right)^{1/2}} \leq 1 \text{ no summation over } i \text{ and } j,\ i \neq j$$

Further details about turbulence and its modelling can be found in [2] and [3].

A4 - Basic CFD

Discretization and second order upwind scheme

The capital letters, W, P, E, denotes nodal points in figure A1. W and E stands for west and east side. The dotted line corresponds to the discrete control volume. The boundaries for the cell are placed mid-way between the adjacent nodes.

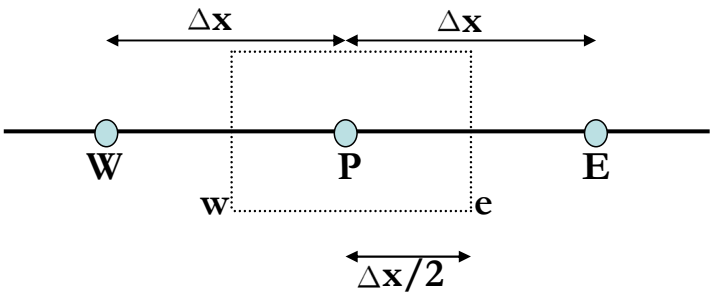

Figure A1: Control volume.

In the finite volume method one integrates over the control volume to yield the discretized equation at its nodal point, e.g. node P in the figure above. To obtain a second order accurate scheme one must use two nodes upstream and that the derivative between the nodes W and P is equal to that between node P and cell face e, i.e.:

$$\frac{T_P - T_W}{\delta x} = \frac{T_e - T_P}{\frac{1}{2}\delta x} \Rightarrow T_e \simeq \frac{3}{2}T_P - \frac{1}{2}T_W$$

where T denotes some property. We are interested to show that the convective term is second order accurate, i.e.

$$\frac{1}{\Delta x}\int \frac{dT}{dx}dx = \frac{T_e - T_w}{\Delta x}$$

Now it is quite obvious to show, with help of the Taylor expansion, that this term is second order accurate.

Basic parameters

y^+

y^+ is a non-dimensional scaled wall-normal:

$$y^+ = \frac{\rho u_\tau y_P}{\mu}$$

where $u_\tau = \sqrt{\tau_w / \rho}$ is the friction velocity, y_P denotes the distance between the wall and first node, ρ the density of the fluid and μ is the viscosity of the fluid at the first node. This parameter is very important since it is correlated with the near wall treatment one uses. Experiments have shown that the near wall-region can be divided into three different parts. These are the viscous sublayer, buffer region and the outer layer. In the viscous sublayer, $y^+ < 5$, the laminar viscosity is important since the no-slip condition must be fulfilled. In the outer region, $30 < y^+ < 300$, which is also called the fully turbulent layer, turbulence is dominating.

The most two common used approaches to model the near-wall region are the wall functions and the enhanced wall treatment. If one use the wall function approach the viscous sublayer and the buffer layer are not resolved. Instead one uses the laminar stress-strain relationship, i.e. $u^+ = y^+$. To use this approach the first node of the grid should be placed in the outer region, i.e. where the y^+ is between 10 and 300. The other approach,

the enhanced wall treatment, resolves all layers all way down to the wall. This approach is a method that combines the wall functions with a two-layer model. The y^+ values should be below 1 to use this approach.

Re-number

The Re number is a dimensionless parameter that yields the ratio between the inertia force and the viscous force, it reads:

$$\mathrm{Re} = \frac{\rho U L}{\mu}$$

where the ρ denotes the density, U the velocity magnitude, L the characteristic length and μ the viscosity.

A5 - Heat transfer

To obtain heat transfer between two media or in a media there should exists a temperature difference. One can actually say that the heat transfer is thermal energy in transportation due to a temperature difference. The three different types of modes of heat transfer are: conduction, convection and radiation.

Conduction

The interactions between particles (translations, rotational and vibrational motions of the particles) with different temperature yields conduction, that is to say transfer of energy from more energetic particles to less energetic ones.

Convection

The convective heat transfer depends on the details of the flow field and the properties of the fluid. The process occurs when a solid surface and a fluid with different temperature are in contact. The convective heat transfer is subdivided into forced, free and combined convection. The forced one is generated by external means. The free convection is generated by pressure gradients together with temperature gradients. Where both the forced and free convection exists simultaneously, the combined convection occurs. Close to the wall, the diffusion (convection) is the only convective heat transfer process. The heat flux from a surface to its surrounding fluid is described by Newton's law of cooling which reads:

$$\dot{Q} = h(T_s - T_\infty) \quad \left[W/m^2 \right]$$

Pr-number

The Pr-number is the ratio between the rate of diffusion of viscous effects to the rate of diffusion of heat and reads:

$$\mathrm{Pr} = \frac{\upsilon}{\alpha}$$

Nu-number

The Nu-number is another important parameter to consider. It's equal to the HTC multiplied with the characteristic length D and divided by the conductivity. One also

knows that the HTC is equal to the surface heat flux divided by the temperature difference between the bulk temperature and the temperature of the wall, i.e.

$$Nu = \frac{hD}{\lambda} = \frac{q_w D}{\lambda \Delta T}$$

Correlation	Eqn. number	Geometry	Conditions
$Nu_x = 0.332\,\mathrm{Re}_x^{1/2}\,\mathrm{Pr}^{1/3}$	[1] (7.23)	Flat plate	Laminar, local, T_f, $0.6 \le Pr \le 50$
$\overline{Nu_x} = 0.664\,\mathrm{Re}_x^{1/2}\,\mathrm{Pr}^{1/3}$	[1] (7.31)	Flat plate	Laminar, average, T_f, $0.6 \le Pr \le 50$
$Nu_x = 0.0296\,\mathrm{Re}_x^{4/5}\,\mathrm{Pr}^{1/3}$	[1] (7.37)	Flat plate	Turbulent, local, T_f, $Re_x \le 10^8$ $0.6 \le Pr \le 60$
$\overline{Nu_L} = 0.037\,\mathrm{Re}_L^{4/5}\,\mathrm{Pr}^{1/3}$	[1] (7.44)	Flat plate	Mixed, T_f, L >> Xc
$Nu_{L,turb} = \frac{0.037\,\mathrm{Re}_L^{4/5}\,\mathrm{Pr}}{1 + 2.443\,\mathrm{Re}_L^{-0.1}(\mathrm{Pr}^{2/3} - 1)}$	[Petukhov] [1]	Flat plate	Turbulent, local, T_f
$Nu_D = 0.023\,\mathrm{Re}_D^{4/5}\,\mathrm{Pr}^{1/3}$	[Colburn] [1] (8.59)	Pipeflow	Turbulent, fully developed, $0.6 \le Pr \le 160$, $Re_D \ge 10000$, $(L/D) \ge 10$, T_m
$Nu_D = 0.023\,\mathrm{Re}_D^{4/5}\,\mathrm{Pr}^{n}$	[Dittus-Boelter] [1] (8.60)	Pipeflow	Turbulent, fully developed, $0.6 \le Pr \le 160$ $Re_D \ge 10000$, $(L/D) \ge 10$, n=0.4 for $T_s > T_m$ and n=0.3 for $T_s < T_m$
$Nu_D = \frac{(f/8)\,\mathrm{Re}_D\,\mathrm{Pr}}{1.07 + 12.7(f/8)^{1/2}(\mathrm{Pr}^{2/3} - 1)}$	[Petukhov] [1] (8.62)	Pipeflow	Turbulent, fully developed, $0.5 < Pr < 2000$ $10000 \le Re_D \le 5 \times 10^6$, $(L/D) \ge 10$, T_m
$Nu_D = \frac{(f/8)(\mathrm{Re}_D - 1000)\,\mathrm{Pr}}{1 + 12.7(f/8)^{1/2}(\mathrm{Pr}^{2/3} - 1)}$	[1] (8.63)	Pipeflow	Turbulent, fully developed, $0.5 < Pr < 2000$ $3000 \le Re_D \le 5 \times 10^6$, $(L/D) \ge 10$, T_m
$Nu_D = 3.66 + \frac{0.0668\,\mathrm{Re}_D\,\mathrm{Pr}(D/L)}{1 + 0.04\left[\mathrm{Re}_D\,\mathrm{Pr}(D/L)\right]^{2/3}}$	[1] (8.56)	Pipeflow	Laminar, thermal entry length (Pr>>1 or an unheated starting length), uniform T_s

[1] Frank P. Incropera, David P. Dewitt, *Fundamentals of Heat and Mass Transfer,* 5th edition, (2002).

Table 1: Standard heat transfer correlations.

Appendix B – 2D Cases

B1 - Flat plate

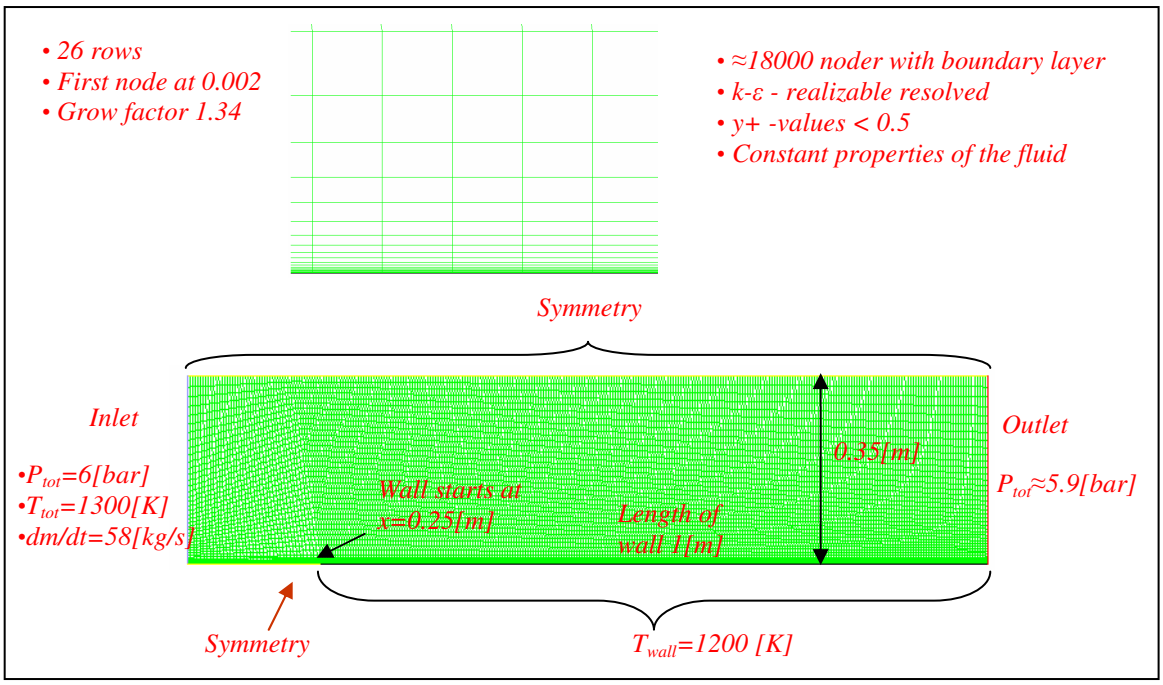

Figure 1: The flat plate settings. Mesh and BCs.

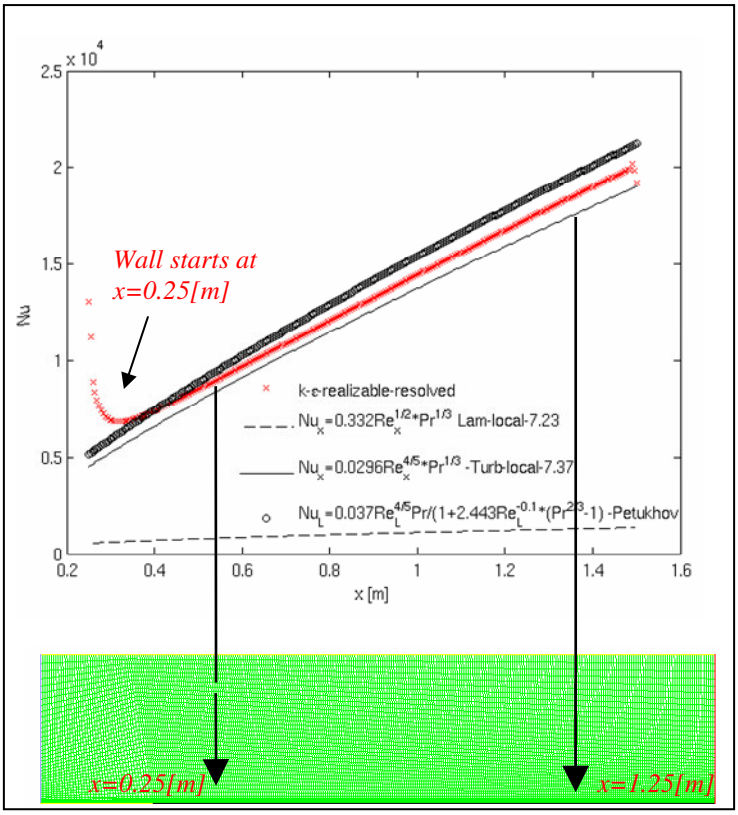

Figure 2: Nu number distributions for the flat plate, comparison CFD results and correlations.

B2 – Pipe flow

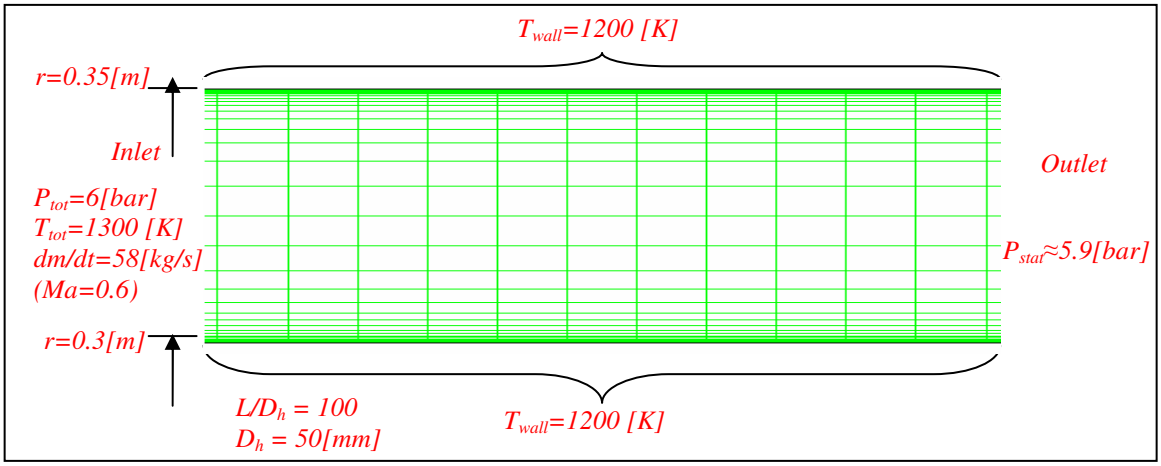

Figure 3: BC settings for the pipeflow / annular channel.

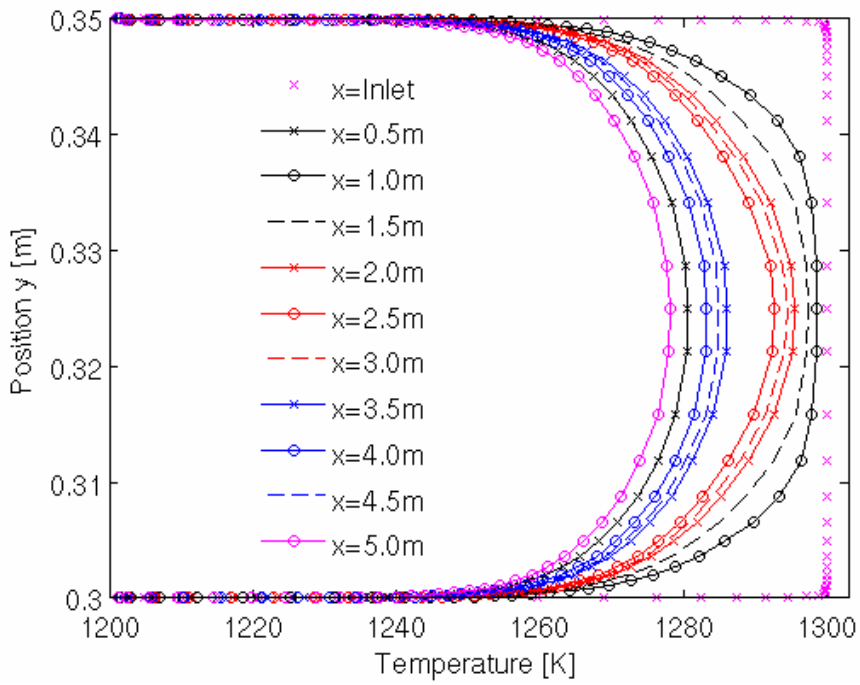

Figure 4: Total temperature profiles at different axial positions.

When one calculates the HTC, it is important to use the instantaneous temperature of the fluid. The temperature profile in figure 5 is used where a fourth order polynomial is fitted to the averaged radial temperature for different axial positions.

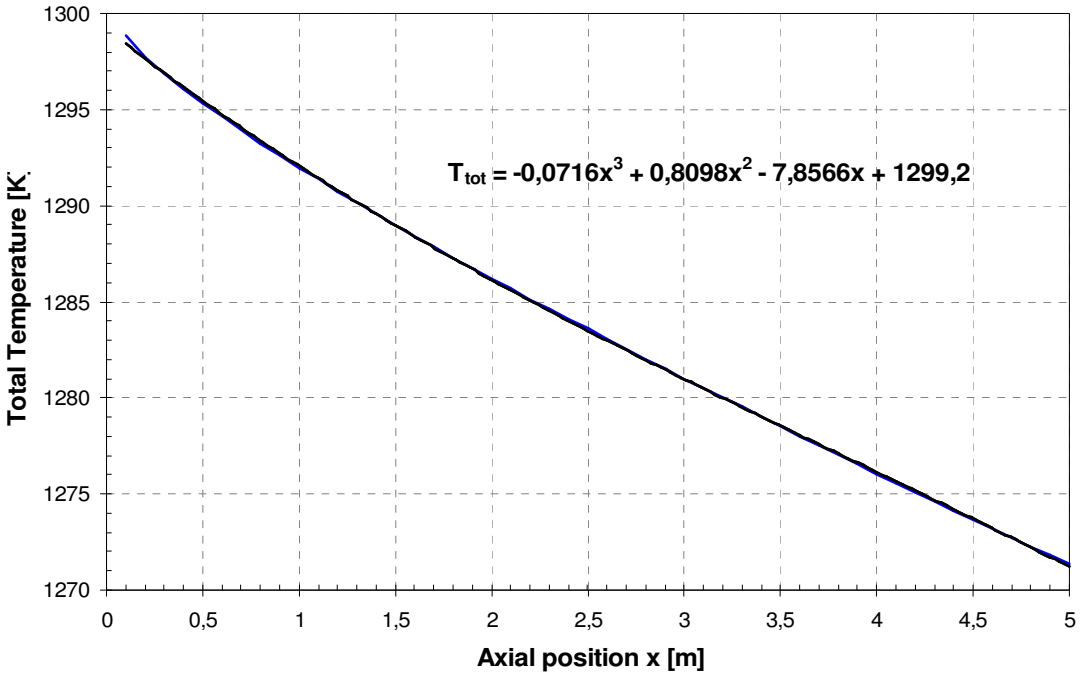

Figure 5: Average total temperature at different axial positions.

B3 – Diffusers

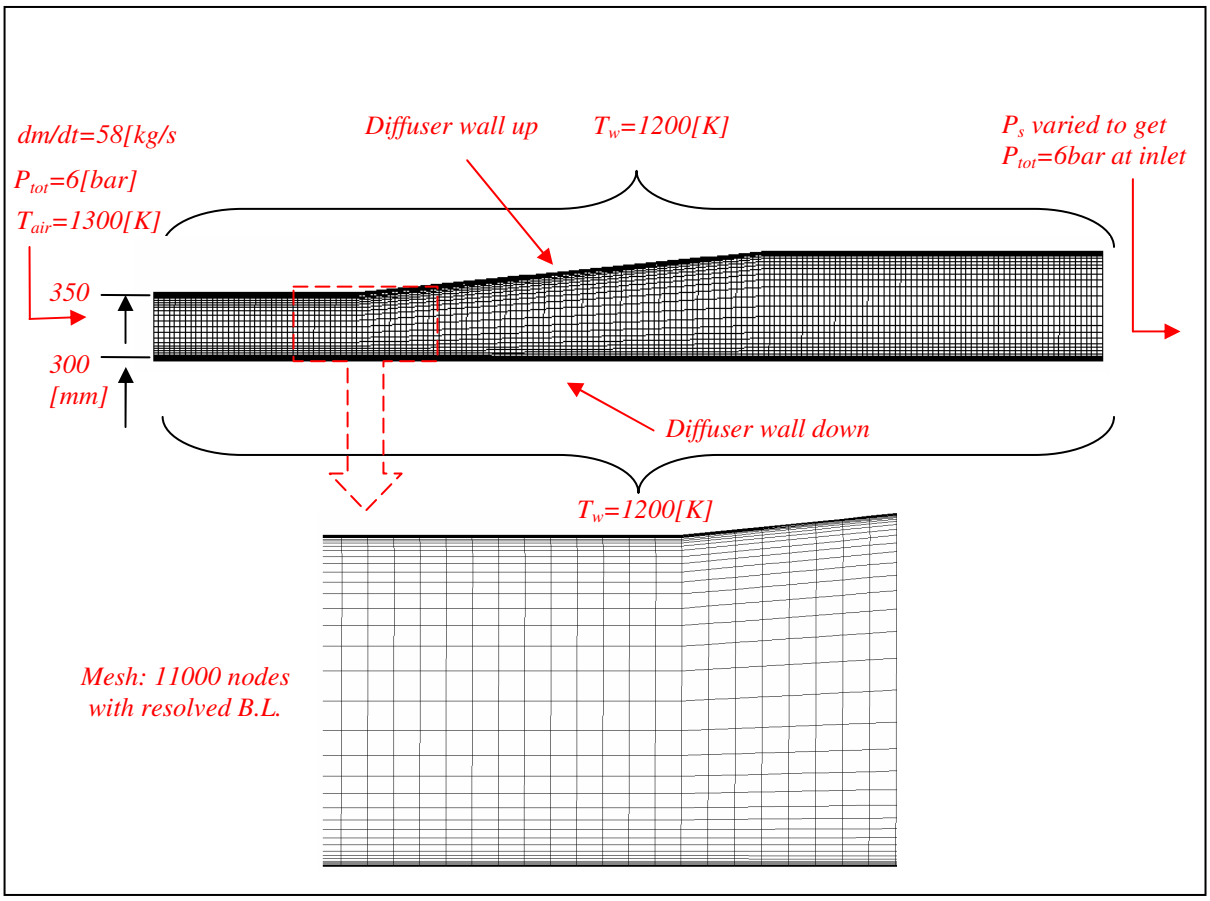

Figure 6: Mesh and BCs for the diffuser test case.

The results for the dependence on boundary layer thickness are presented below.

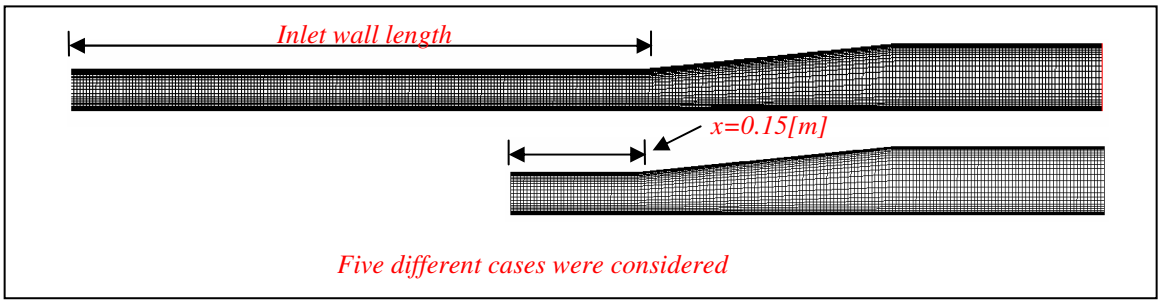

Figure 7: 15 and 3 channel heights as inlet wall length.

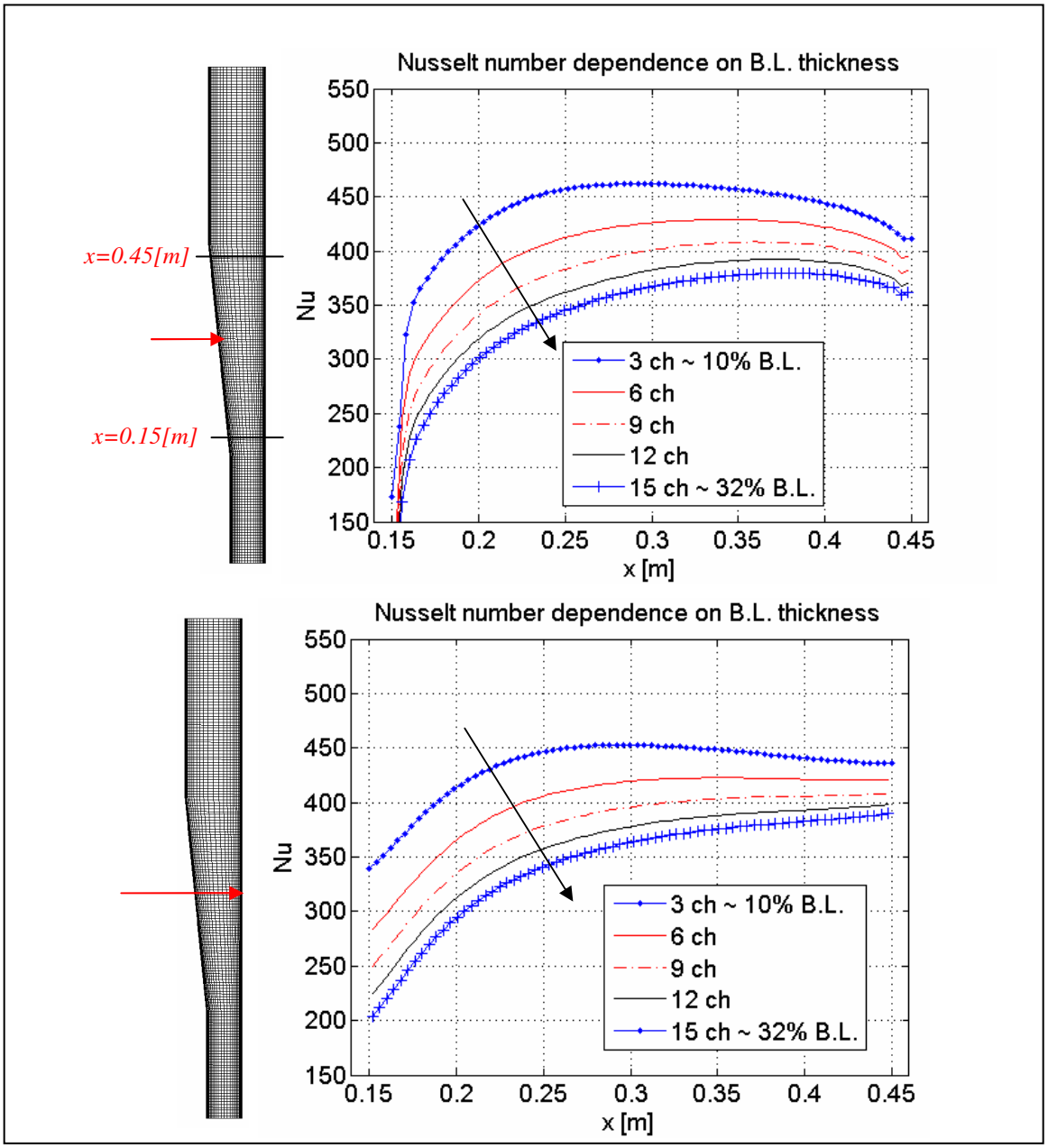

Figure 8: The Nu number distribution on lower and upper walls in the diffuser.

The dependence of diffuser angle on the Nu number distribution is presented below.

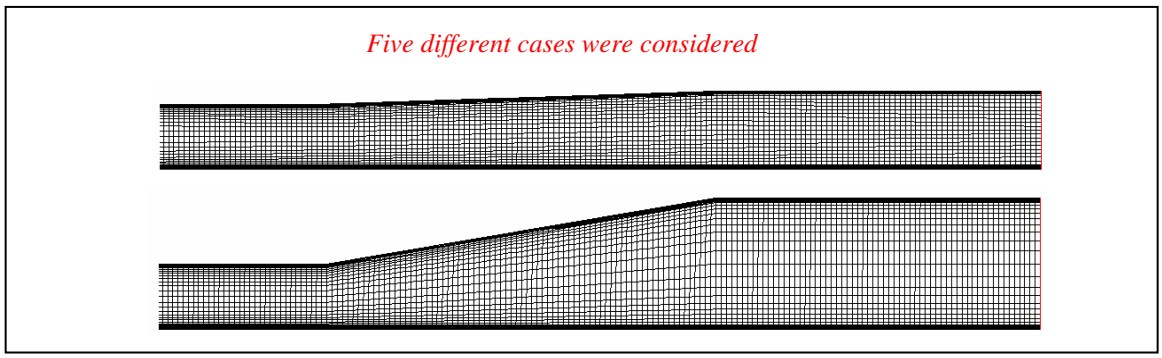

Figure 9: Two different ARs, the minimum AR=1.2 and the maximum AR=2.2.

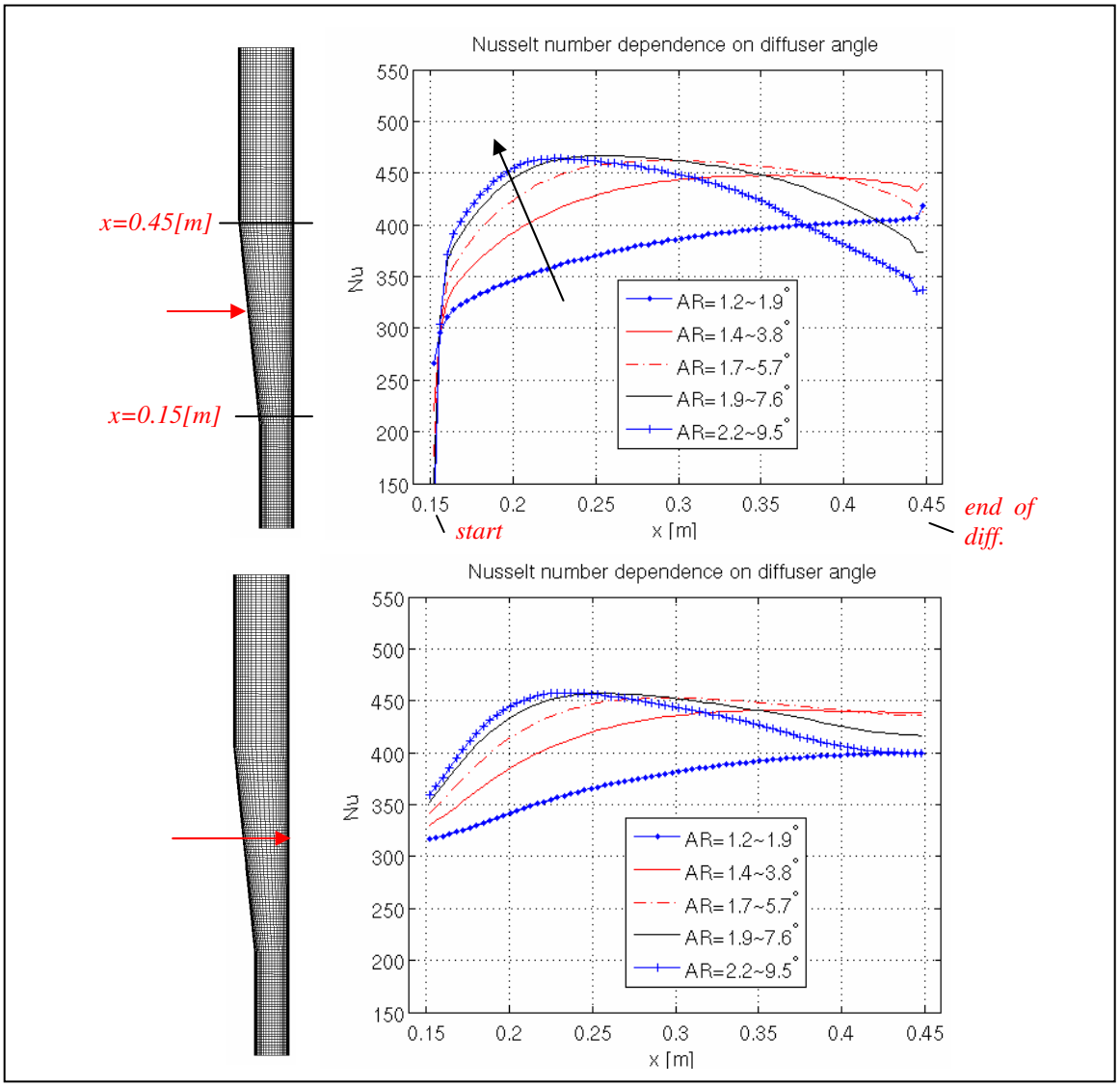

Figure 10: The Nu number distribution on different walls in the diffuser.

The investigation of the dependence of turbulence models on the Nu number distribution is presented below.

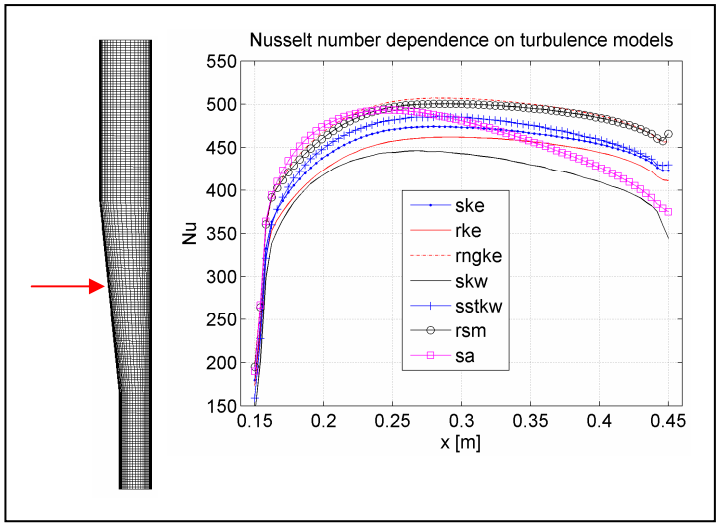

Figure 11: The Nu number distribution on different walls in the diffuser.

B4 – 2D-AITEB2 duct flow

B4.1 – Low speed (CTH)-condition

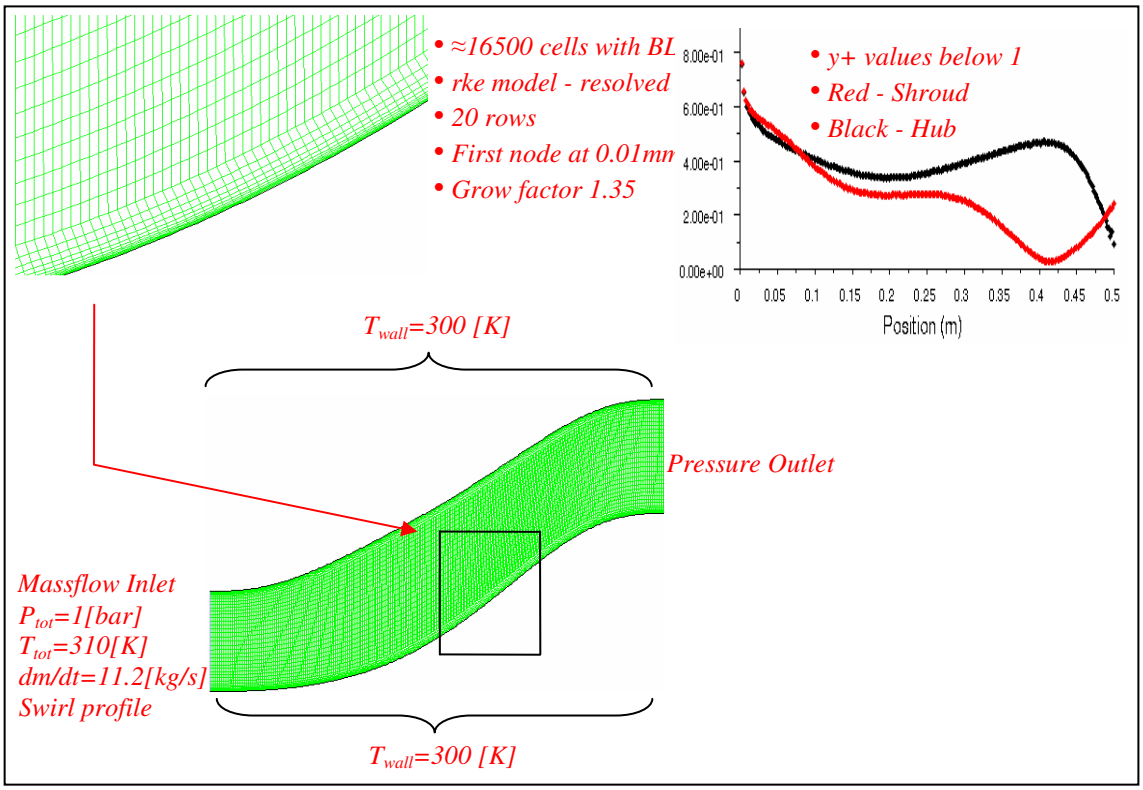

Figure 12: The above figures shows the grid, the y^+ values distribution and the BCs used.

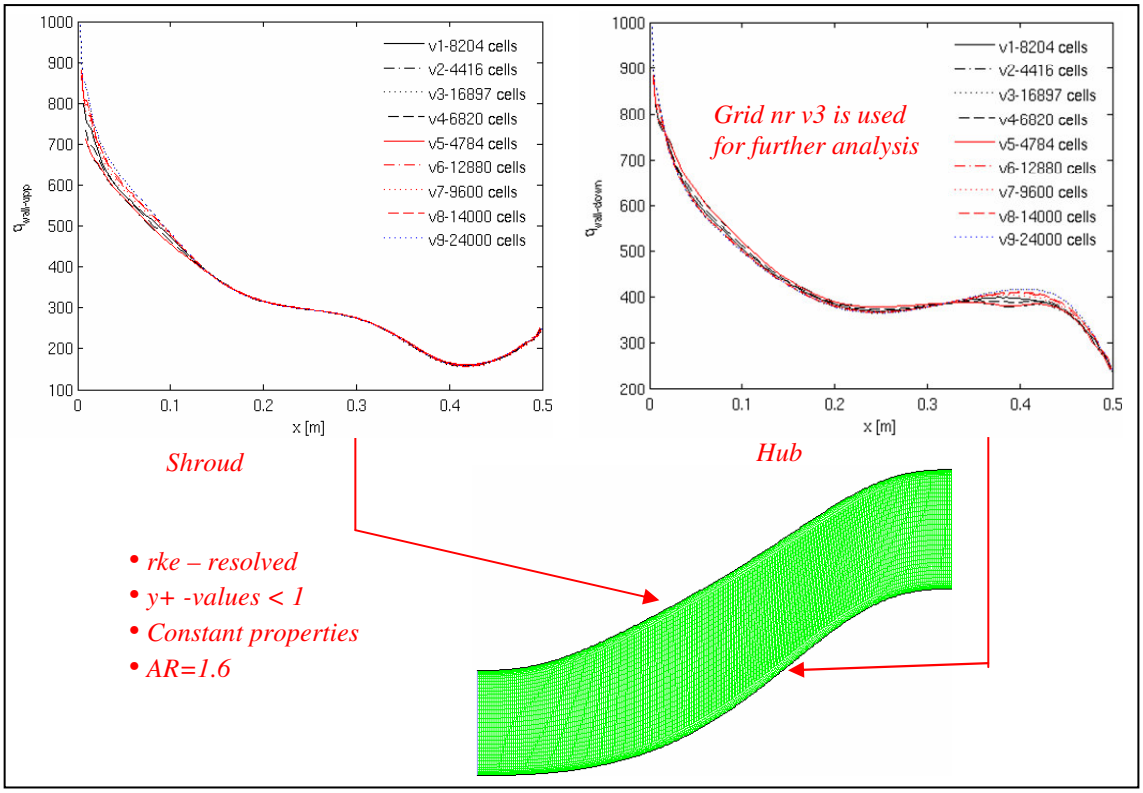

Figure 13: Investigation of the grid dependence due to resolved boundary layer.

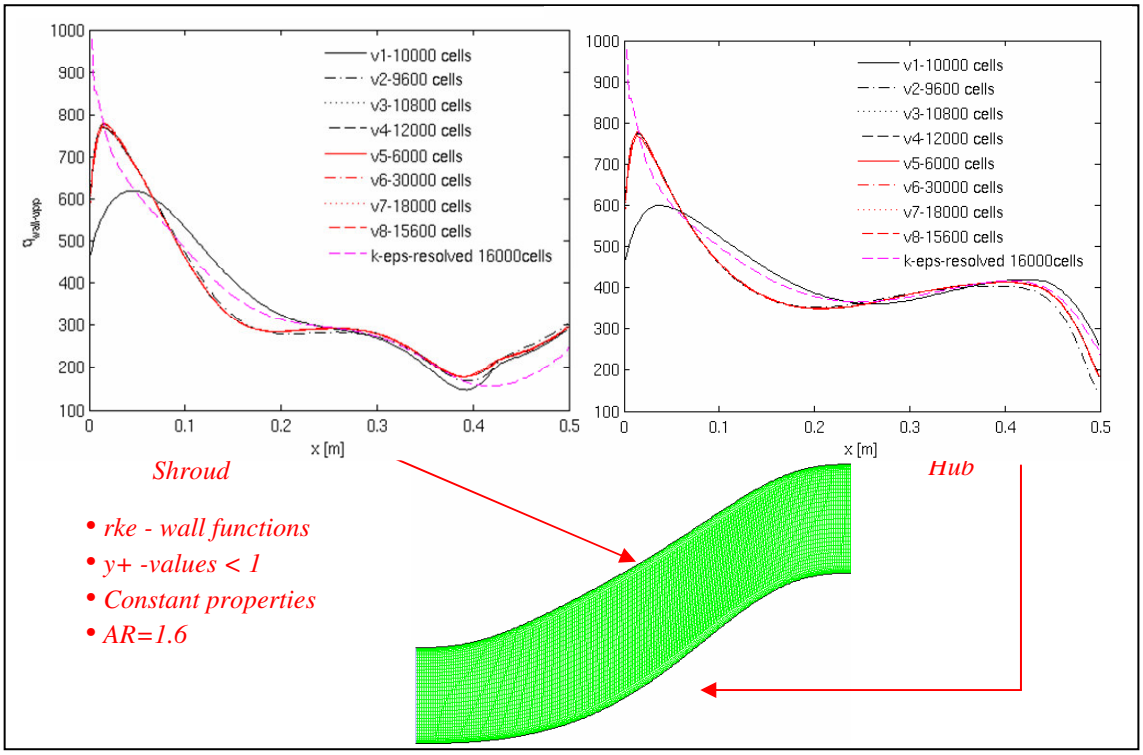

Figure 14: Investigation of the grid dependence due to wall functions.

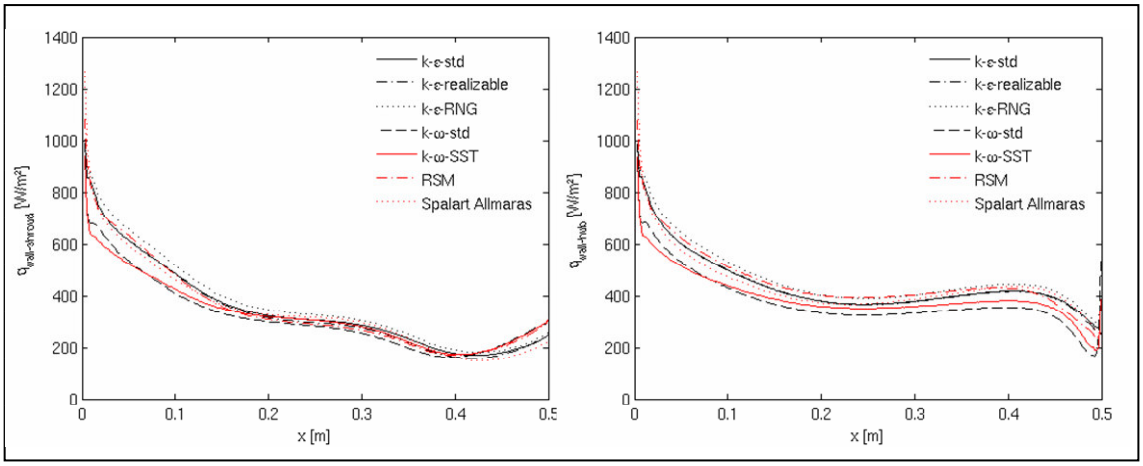

Figure 15: Plot of heat flux for different turbulence models.

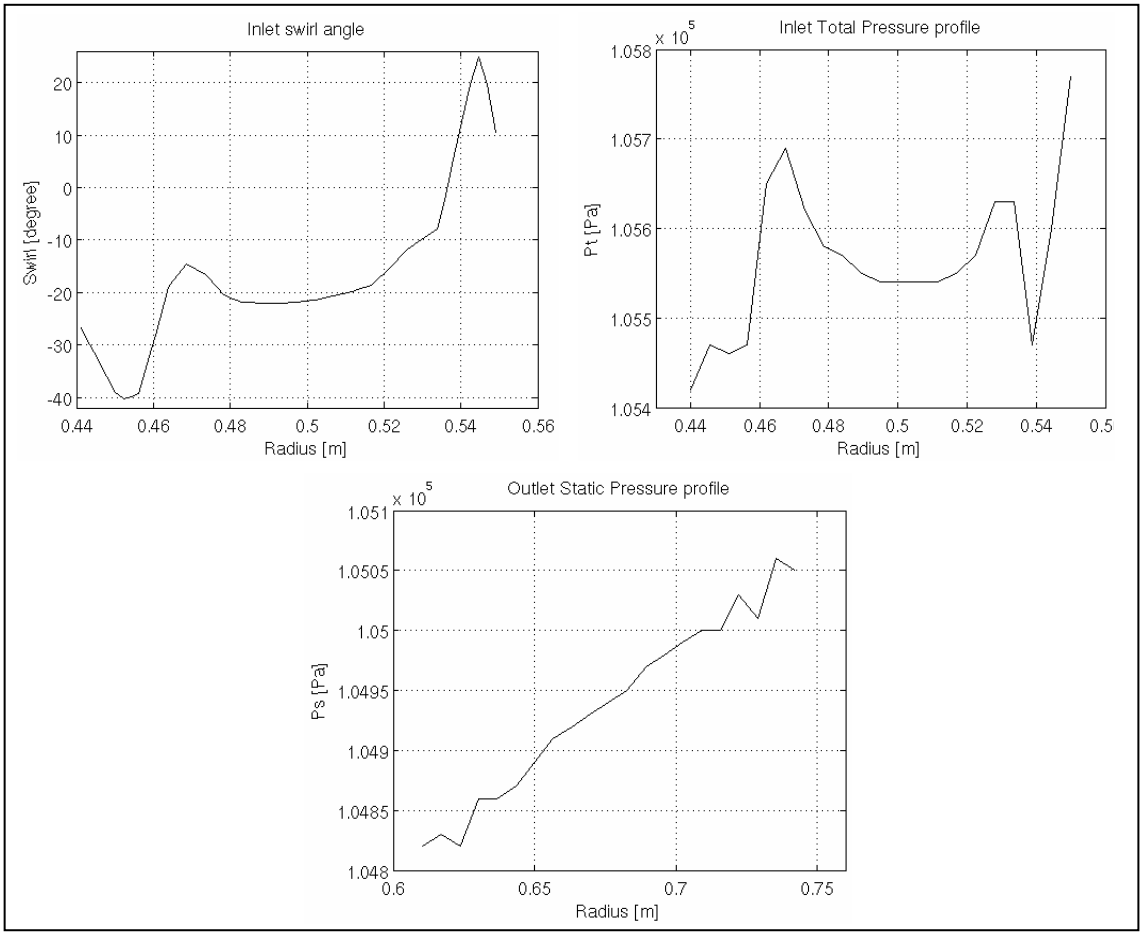

Figure 16: Inlet swirl, inlet total pressure and outlet static pressure profiles.

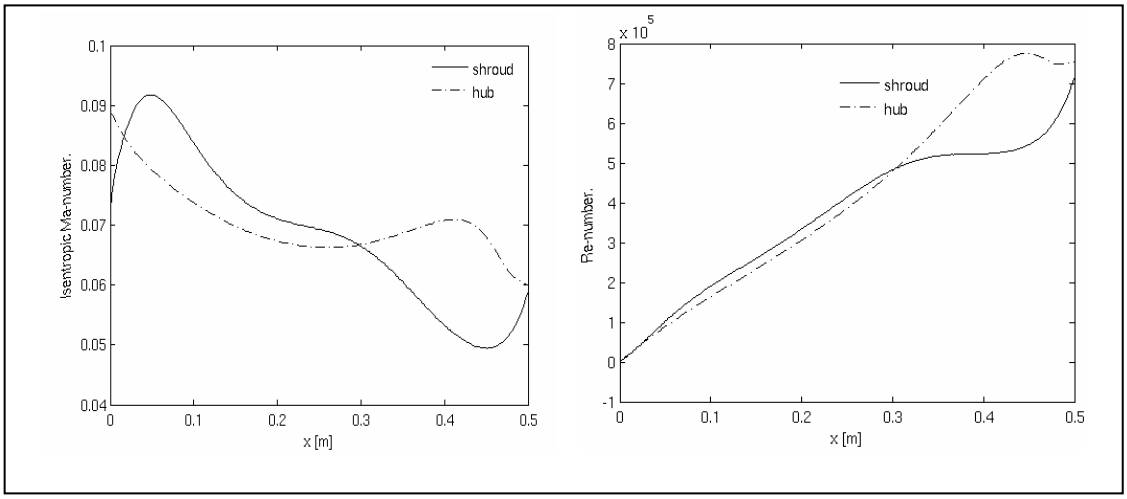

Figure 17: Isentropic Ma number and Re number profiles at different axial positions.

Figure 17 shows the isentropic Ma-number to the left and the local Re number to the right. The isentropic Ma number is computed from the formula A2.1. The Re number is computed through the ordinary formulation: $\mathrm{Re} = UL/\upsilon$ where U is obtained through the local isentropic Ma number and L the surface length along hub and shroud curve.

B4.2 – Real-condition

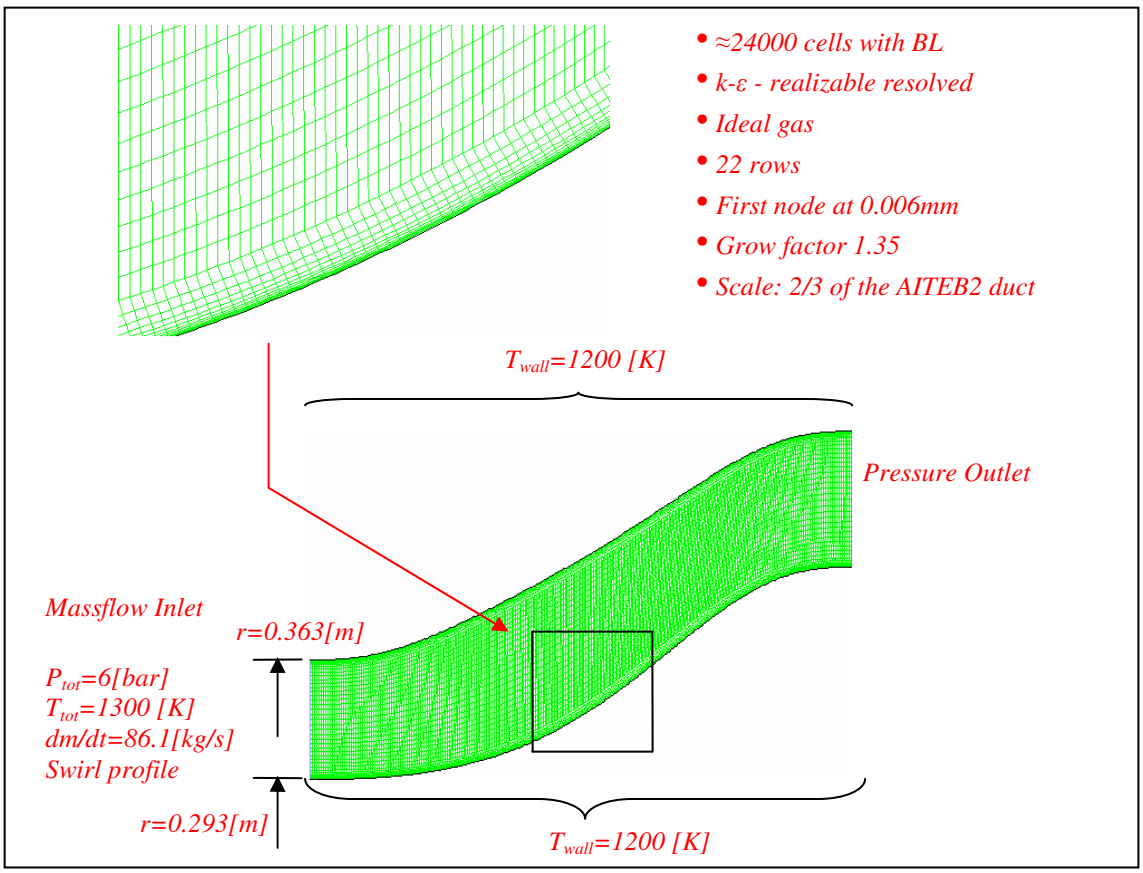

Figure 18: The grid and the BCs.

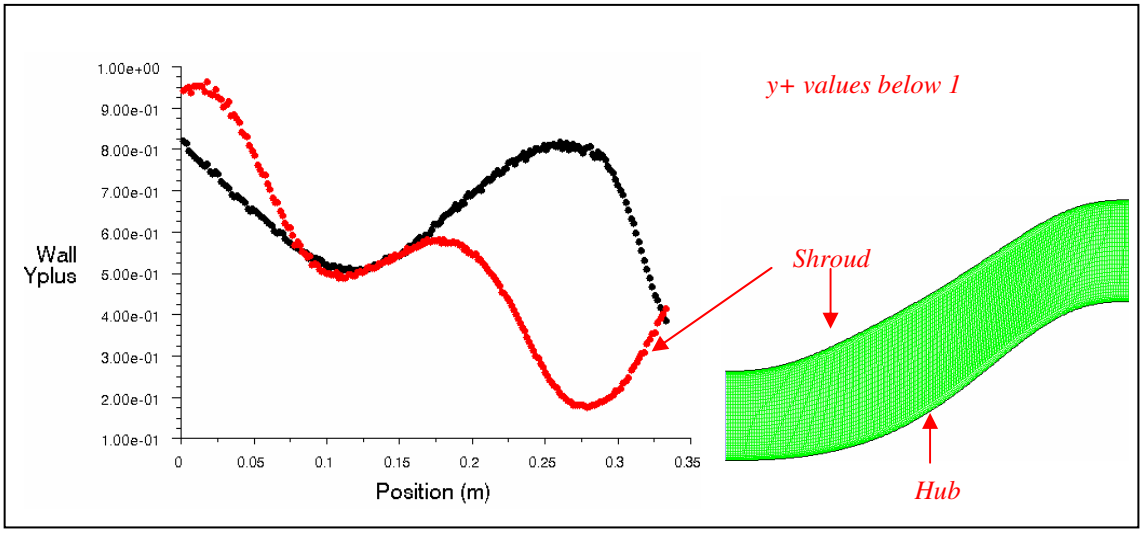

Figure 19: The y^+ distribution along the hub and the shroud surfaces

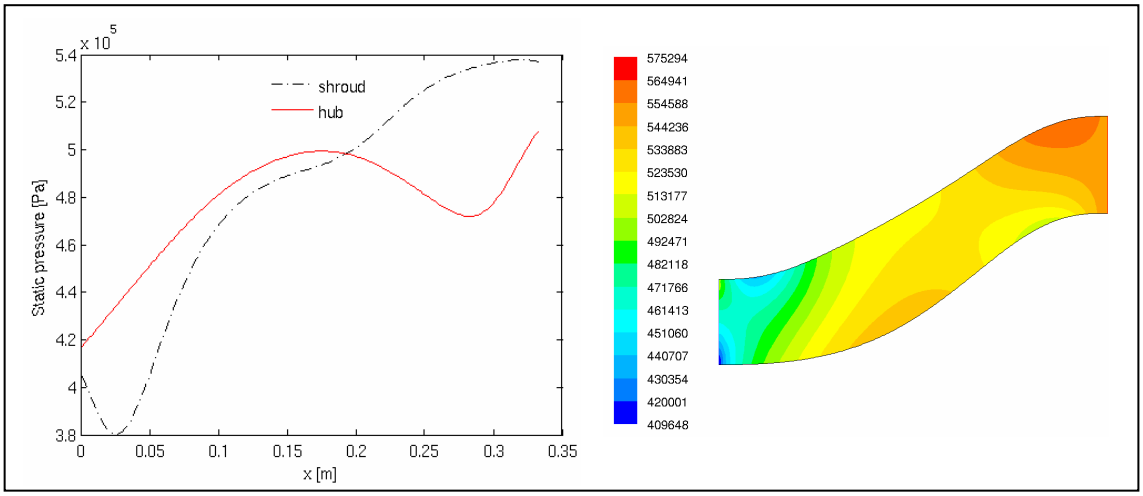

Figure 20: The static pressure profiles and contour plot of the static pressure [Pa].

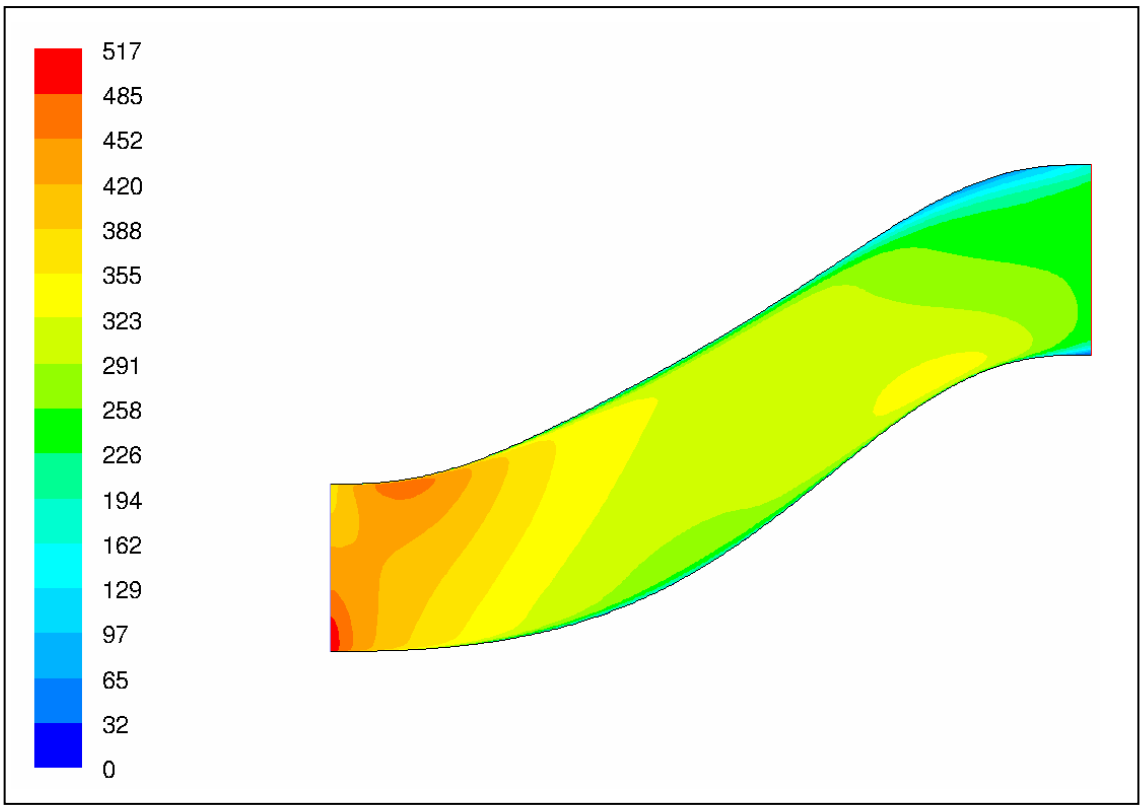

Figure 21: Contour plot of the velocity magnitude [m/s] .

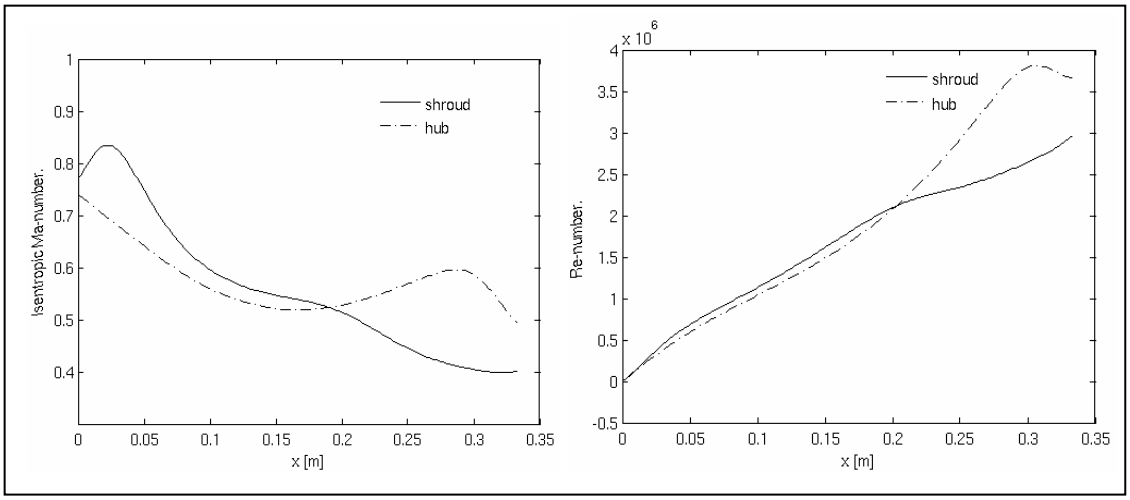

Figure 22: The Isentropic Ma number and Re number profiles

Figure 22 shows a plot representing the isentropic Ma number and the other one showing the Re number. The isentropic Ma number and the Re number is computed as mentioned earlier.

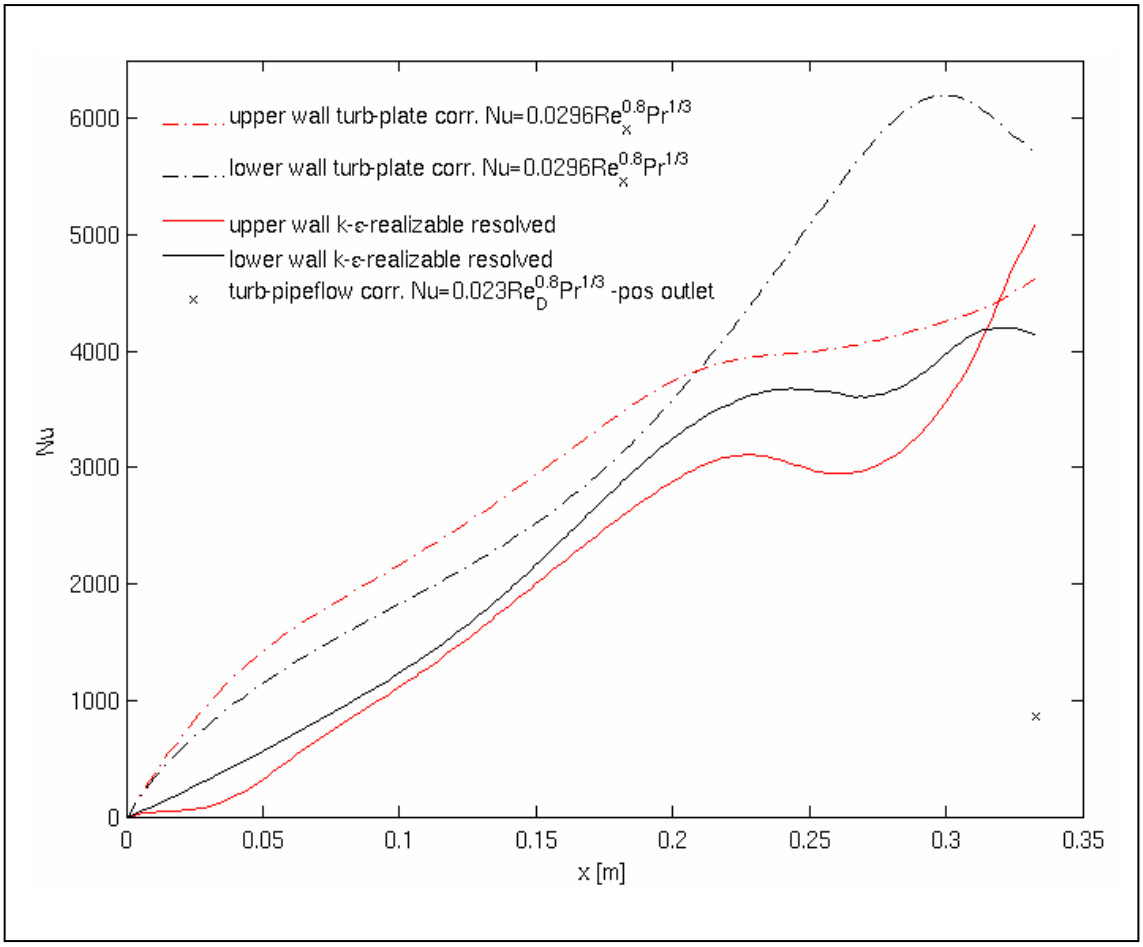

Figure 23: The Nu number distribution compared with correlations.

$$pressure\ \ losses = \frac{\Delta P_0}{P_{dyn-inlet}} = \frac{4996[Pa]}{125013\,[Pa]} \sim 4.0\%$$ Based on the dynamic pressure

Appendix C – 3D cases

C1 – 3D-AITEB2 duct flow

C1.1 – Low speed (CTH)-condition

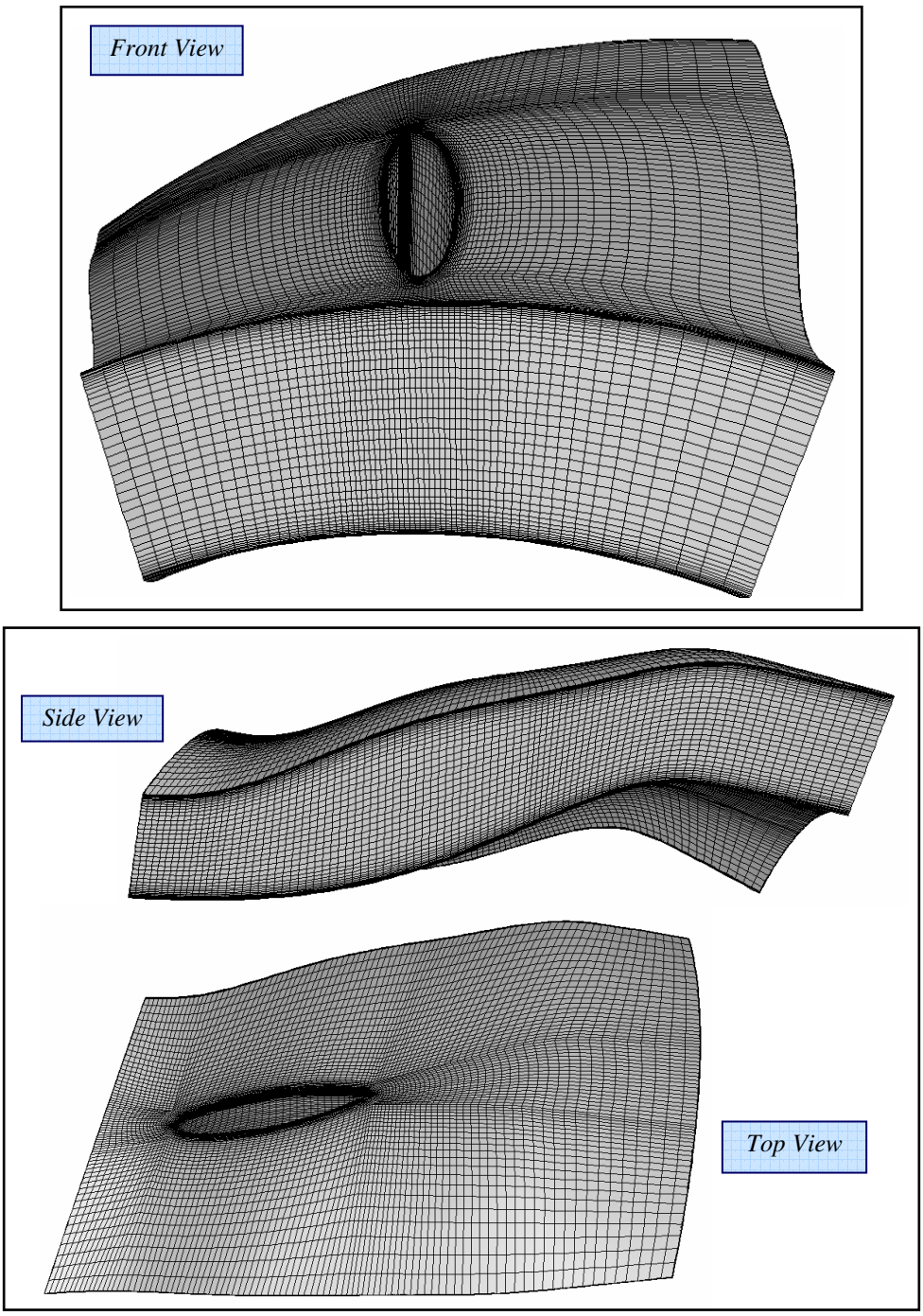

Figure 24: Three different views of the grid: front-, top- and side view.

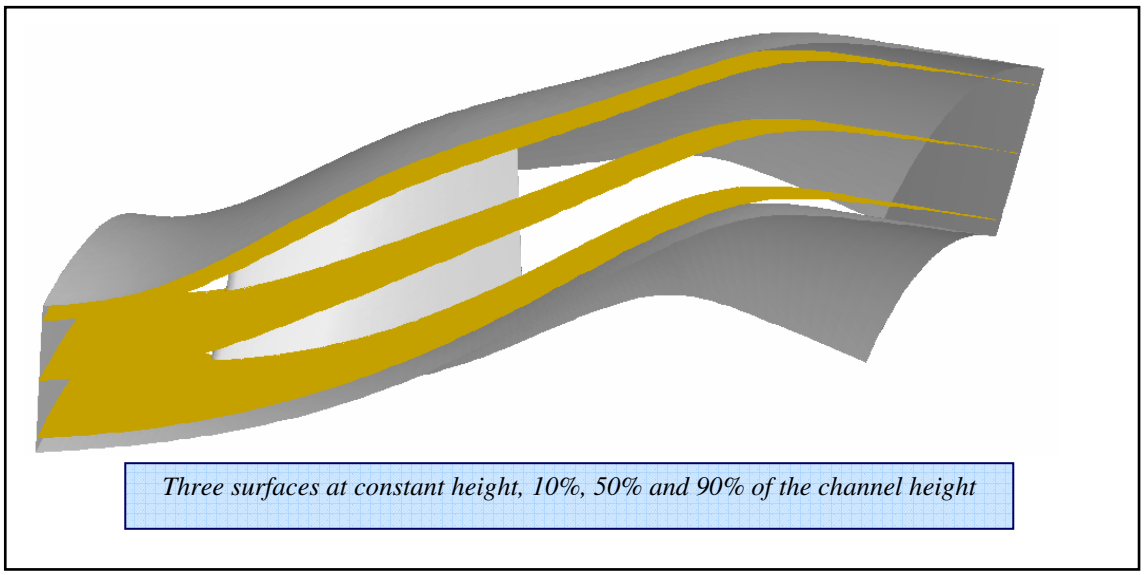

Figure 25: Evaluation surfaces at three different heigths.

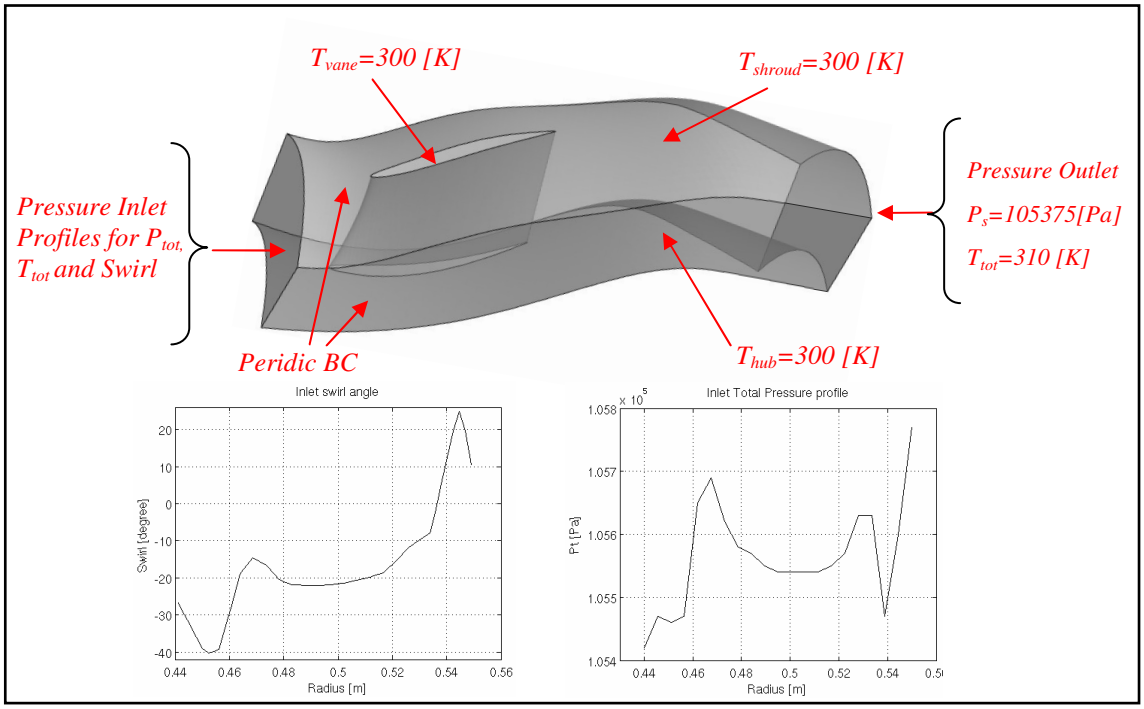

Figure 26: 3D-duct gemetry with the corresponding BCs.

Figure 27 shows the results from the turbulence model investigation. The first column shows the pressure losses. These are based on the difference between the total pressure of the inlet and the outlet, divided by the dynamic pressure of the inlet. The third column shows the mass flow rate through the duct. The problem here is that one needs to iterate, through manipulating the static pressure of the outlet, to achieve the correct mass flow rate.

Case	dPo/Pdyn inlet [%]	Outlet Swirl [deg]	dm/dt [kg/s]	Ma number inlet	Ma number outlet
rke	7,239	-12,65	1,1203	0,0729	0,0446
rngke	6,184	-11,99	1,1128	0,0733	0,0449
ske	7,066	-12,74	1,1124	0,0733	0,0447
skw	7,781	-10,68	1,1075	0,0729	0,0446
sstkw	7,733	-11,52	1,0946	0,0721	0,0441
RSM	6,489	-13,03	1,1051	0,0728	0,0446

Outlet plane axially located at one channel height upstream from outlet (x = 0.505752m)
Mass averaged pressure
Area averaged swirl and Mach number

Table 2: Results of different turbulence models.

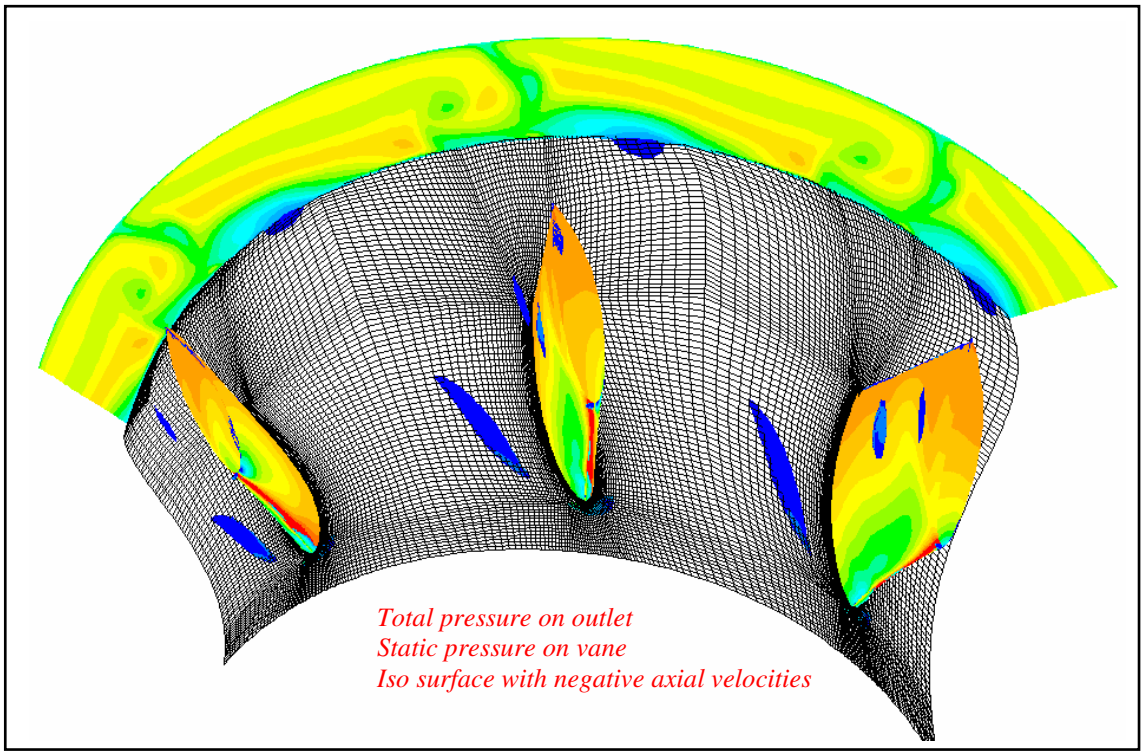

Figure 27: Three sectors contour plot.

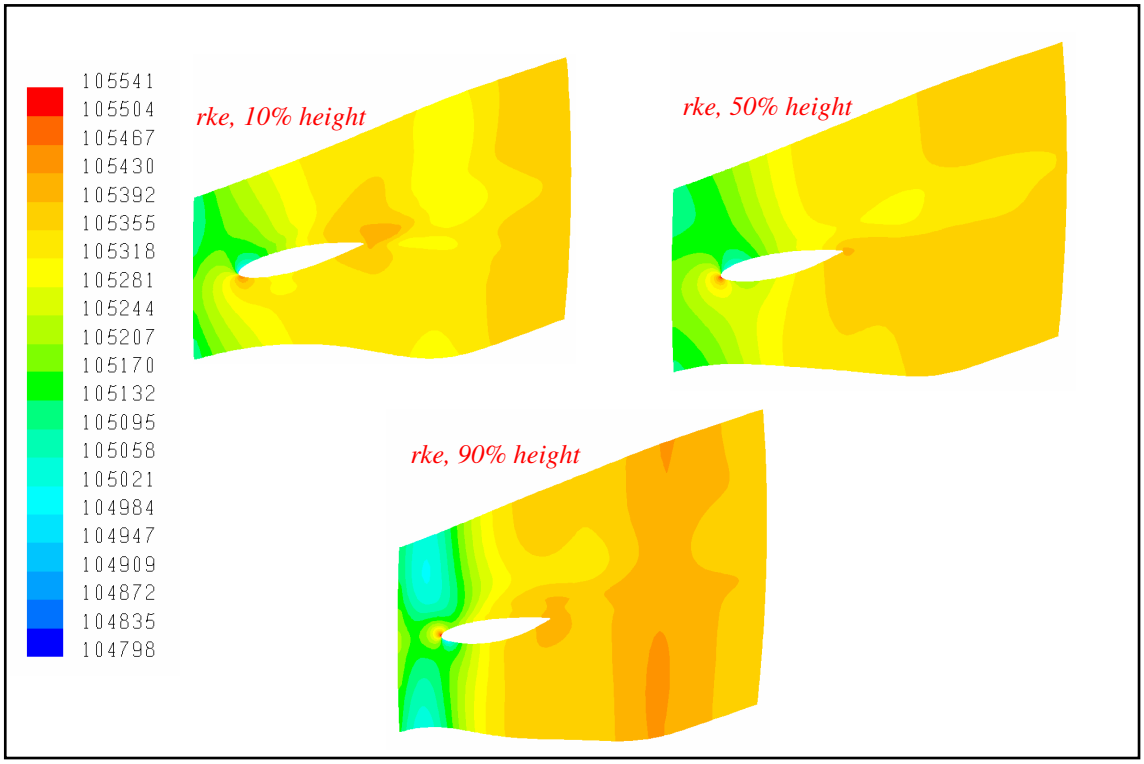

Figure 28: Contours of the static pressure [Pa] at three different channel heights.

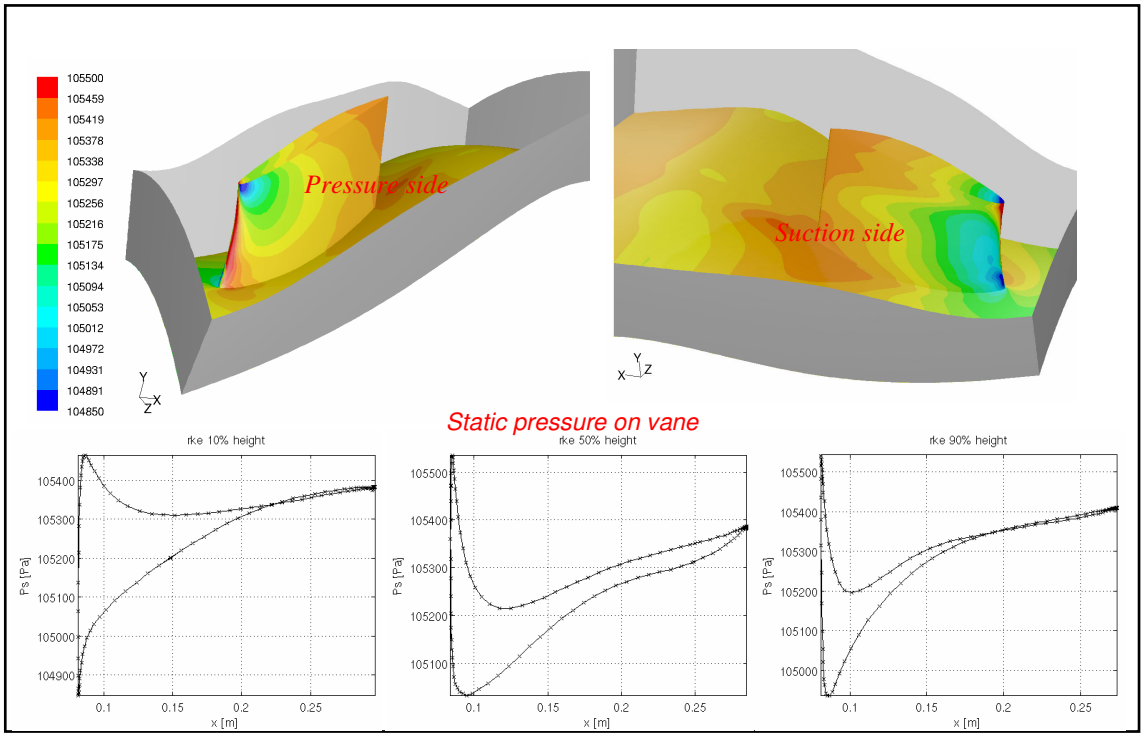

Figure 29: Upper plots: Contours of the static pressure [Pa], Lower figures: Static pressure profiles at three different positions- 10%, 50% and 90% of the channel height.

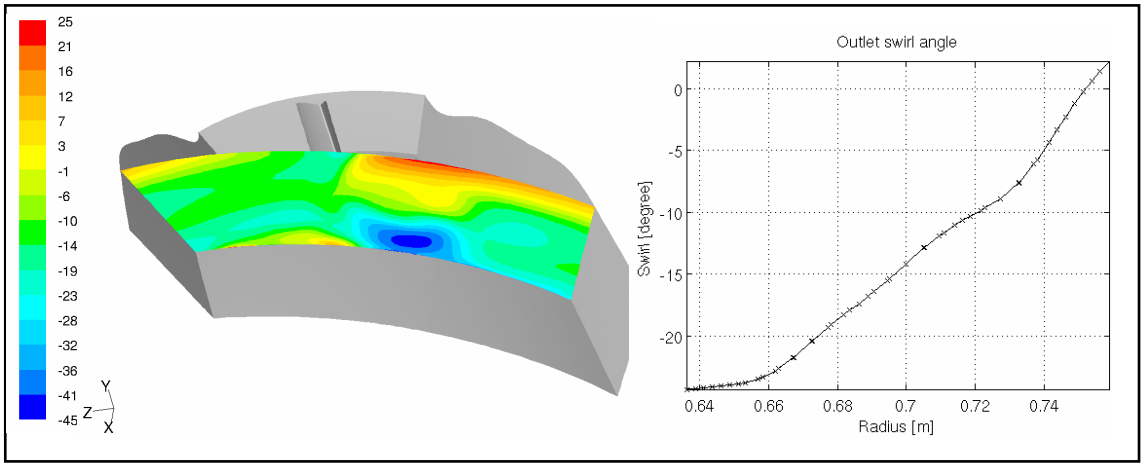

Figure 30: Contour plot and radial average profile of the outlet swirl angel [deg].

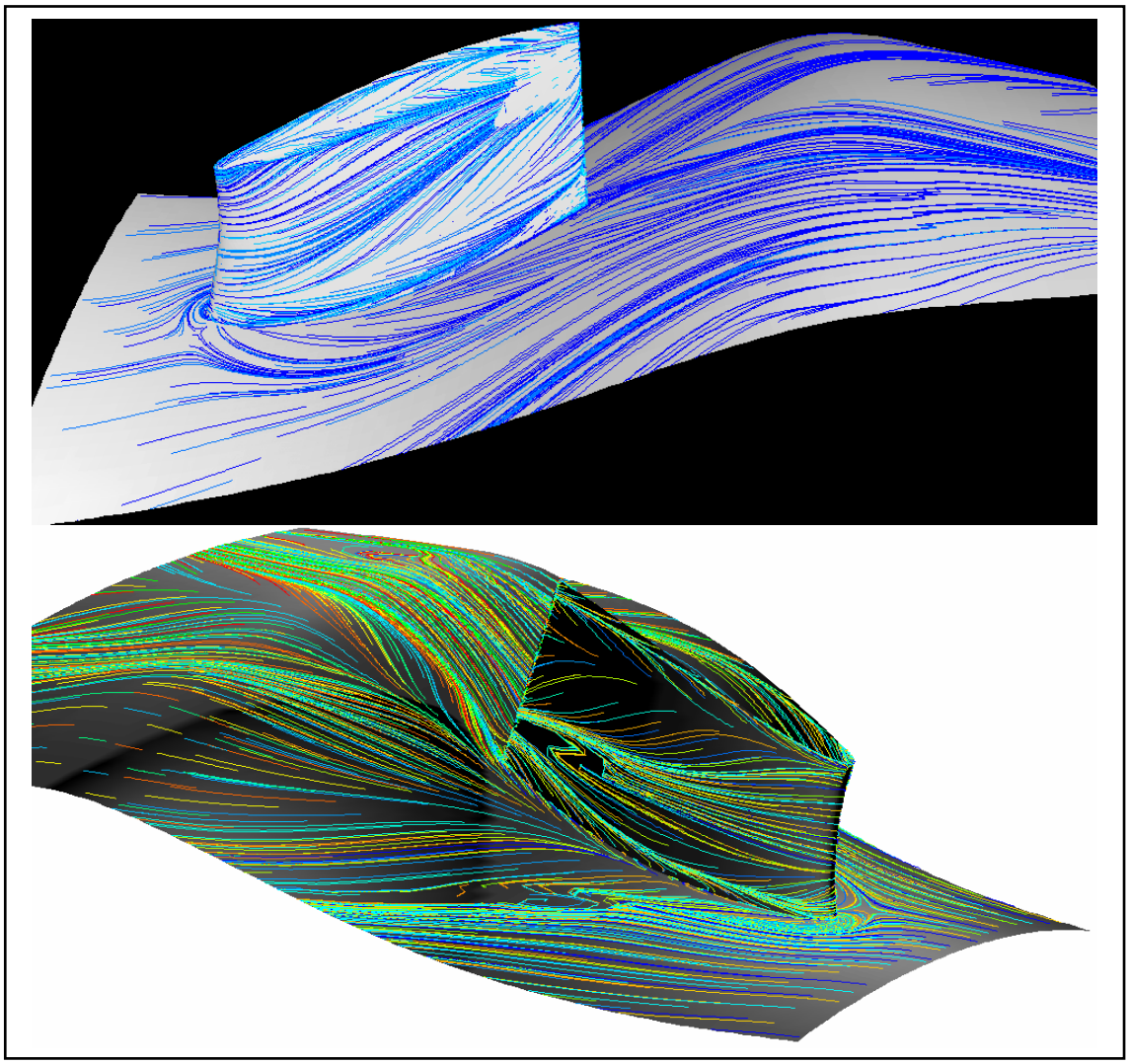

Figure 31: Pathlines along the hub and the vane.

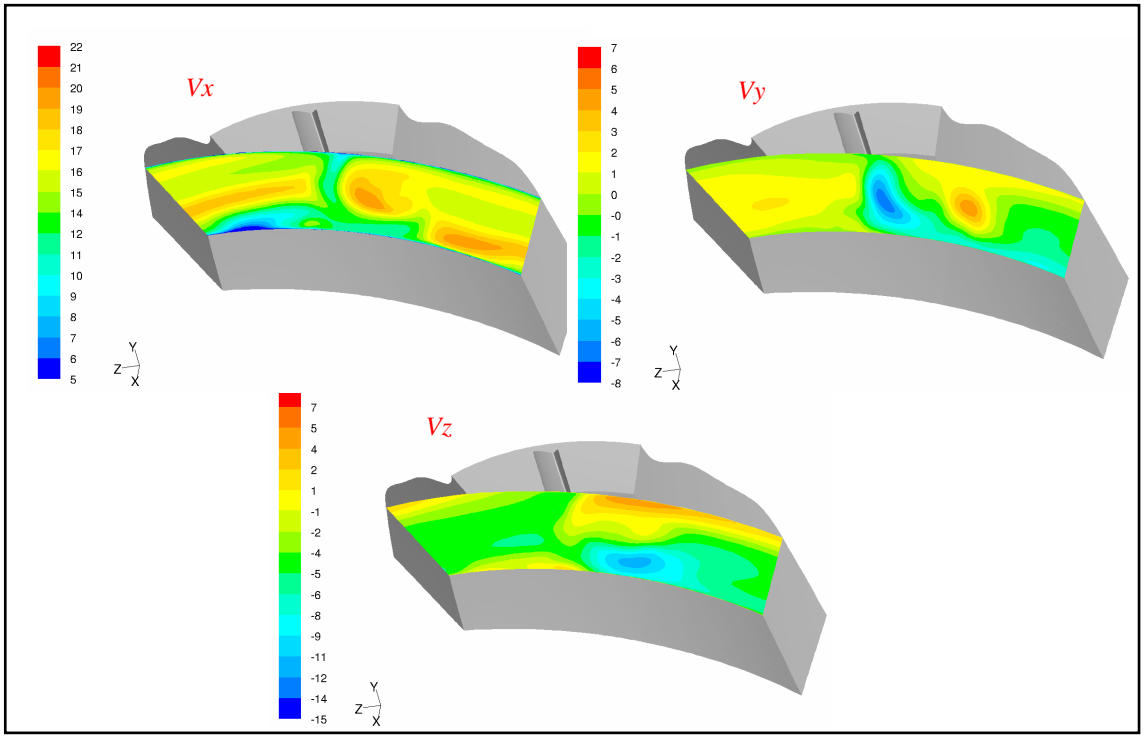

Figure 32: Outlet velocities for the three velocity components [m/s].

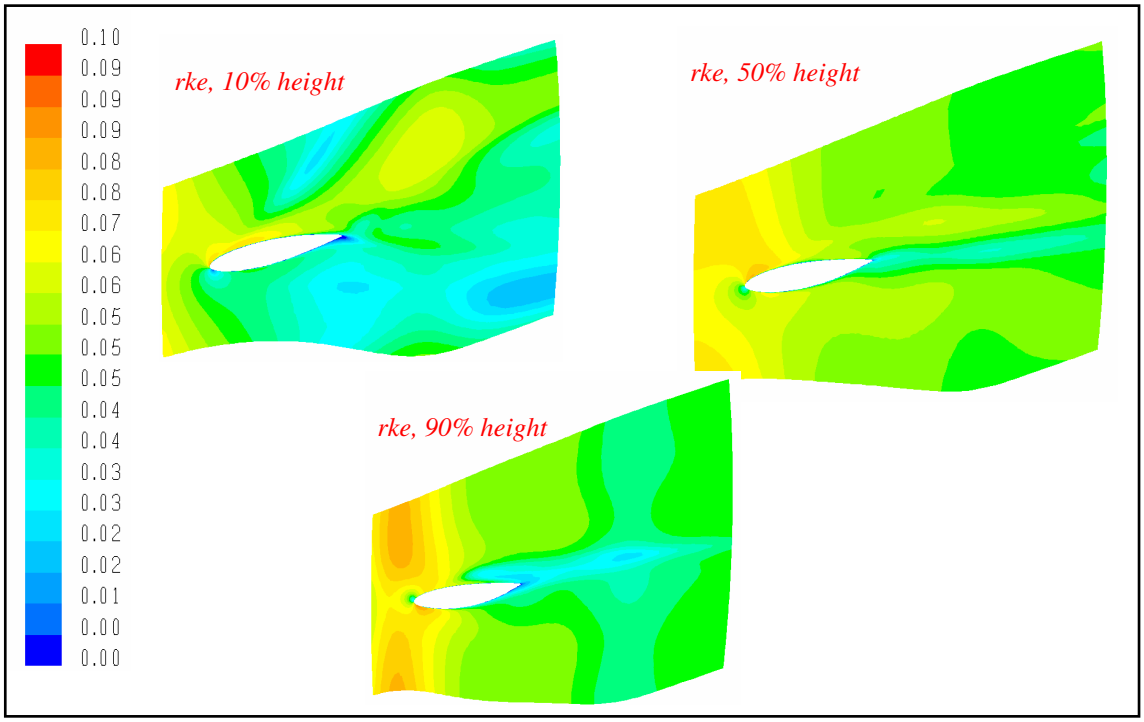

Figure 33: Contours of the Ma number at different heights.

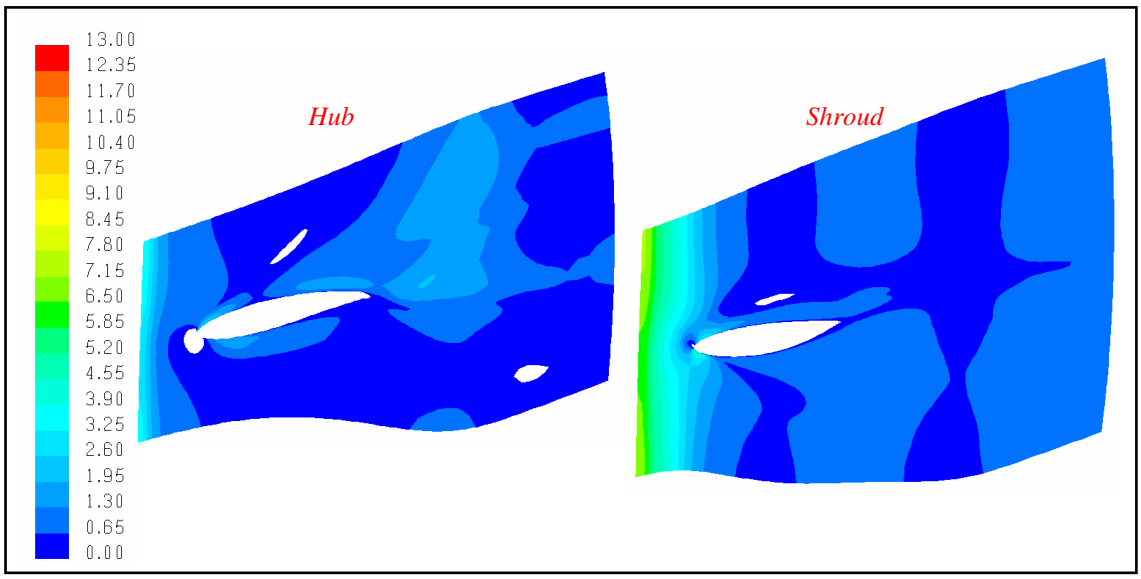

Figure 34: Wall shear x-direction [Pa].

C1.2 - Real-Condition

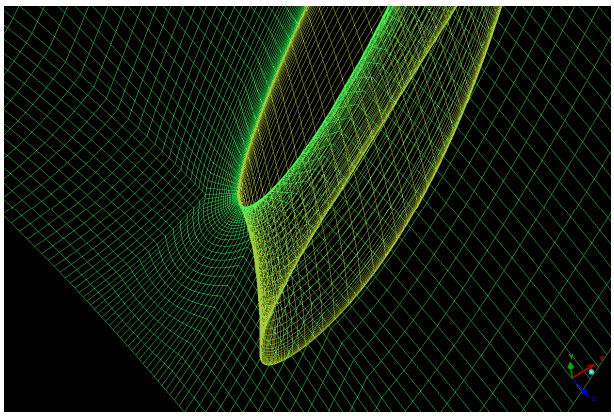

- *scale: 2/3 of the AITEB2 duct*
- *≈1.277.000 cells*
- *k-ε - realizable wf*
- *Ideal gas*
- *y+ values between 10 and 100*
- *hexmesh was done in ICEM CFD*
  - *Min angel>25*
  - *Determinant>0.6*

Figure 35: Mesh settings.

Figure 36: 3D-duct geometry with the corresponding BCs.

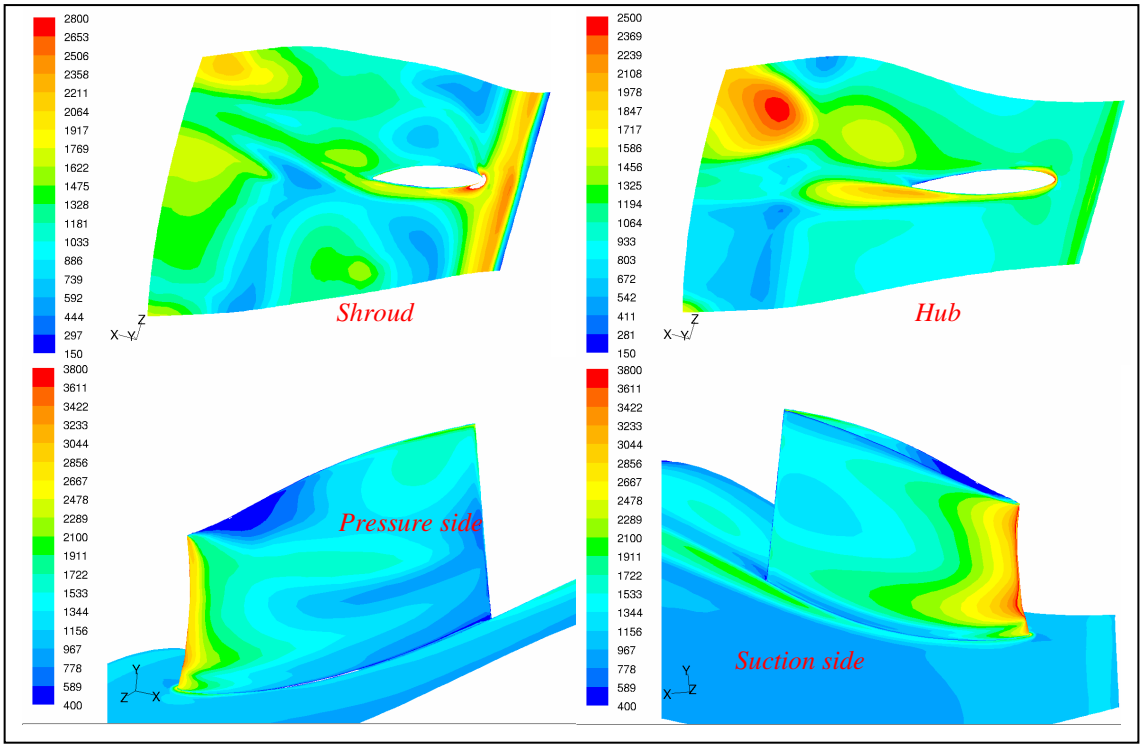

Figure 37: The HTC [W/m^{2}K] for different surfaces

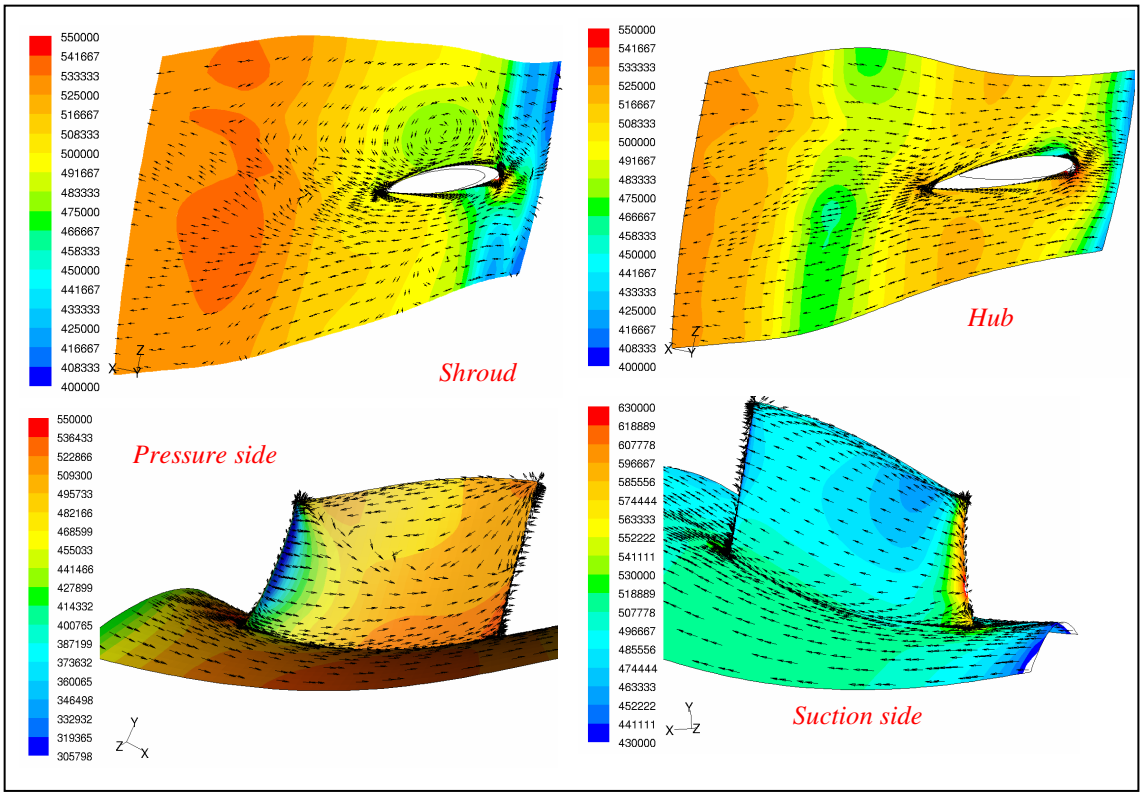

Figure 38: The static pressure [Pa] for different surfaces.

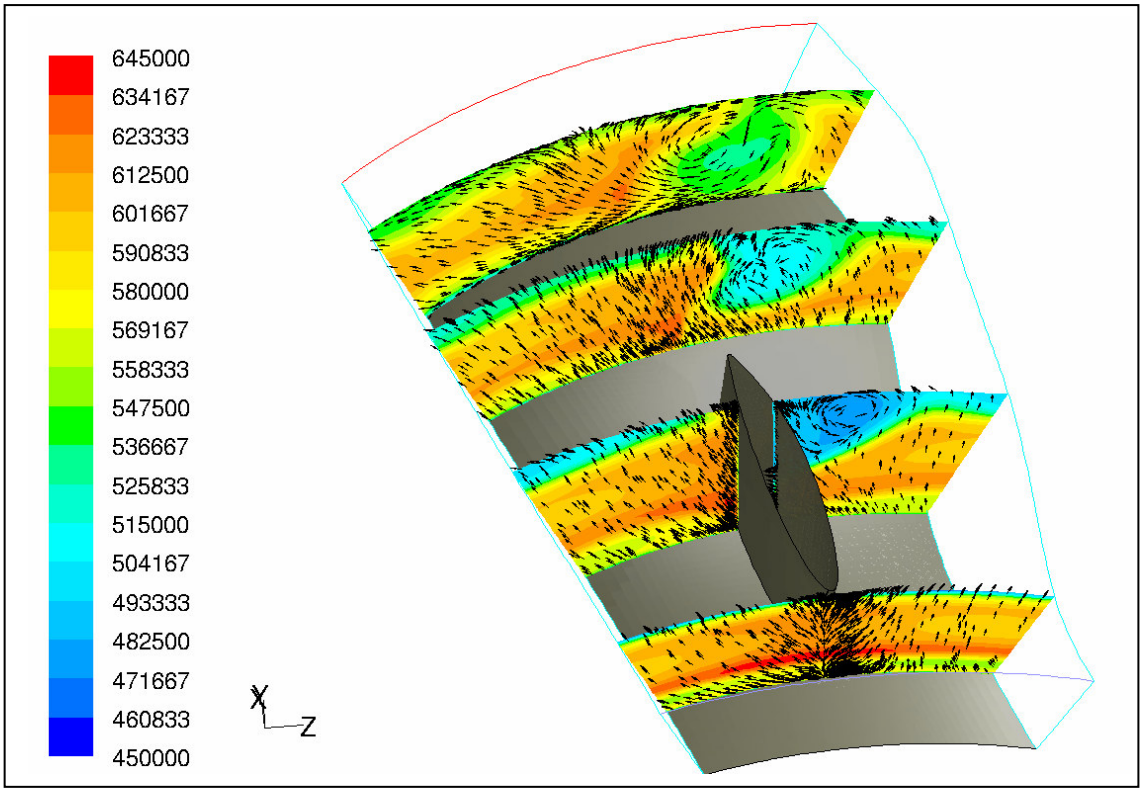

Figure 39: Total pressure [Pa] and velocity vectors at different axial positions

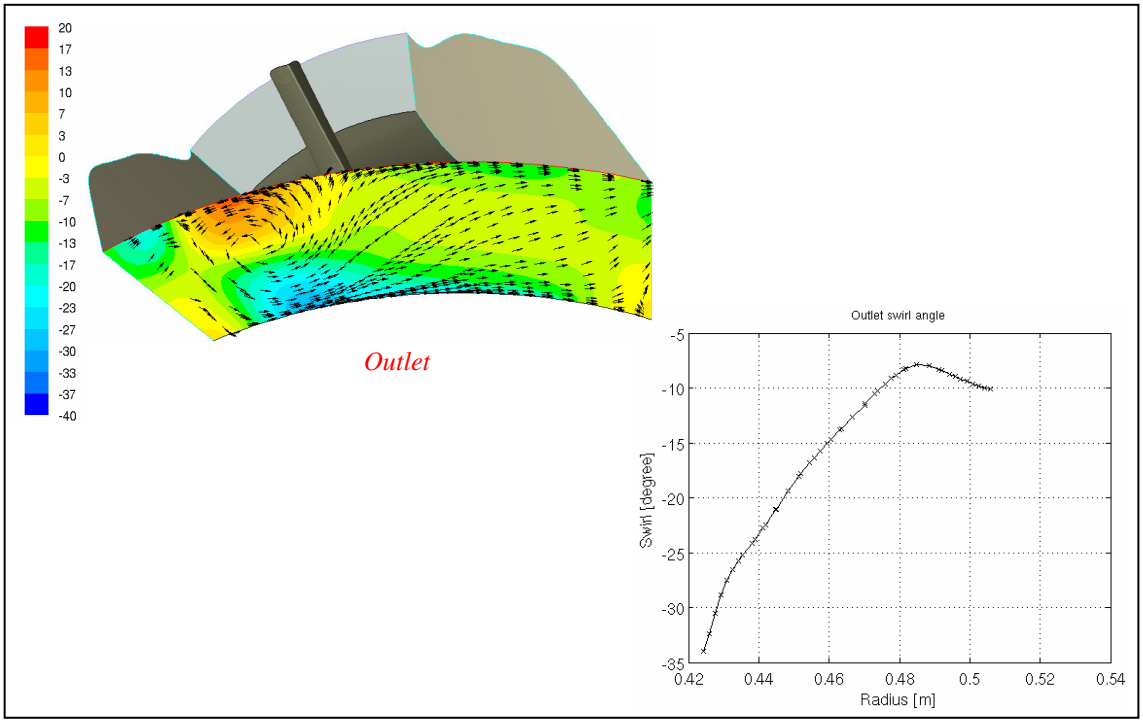

Figure 40: Contours and profile of the outlet swirl angle [deg].

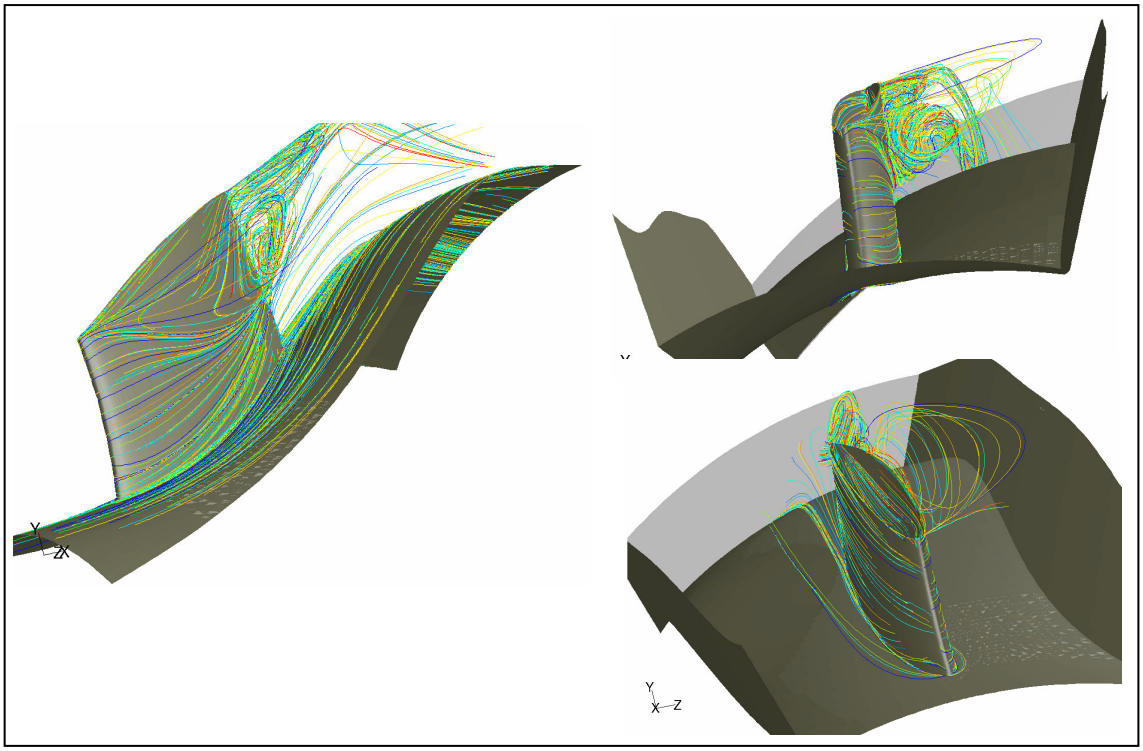

Figure 41: Pathlines released from the leading edge.

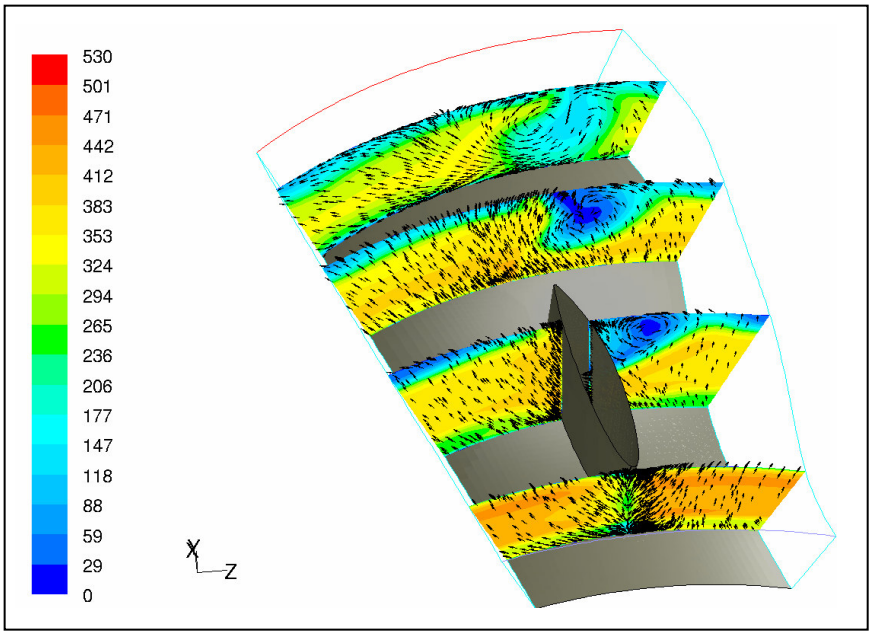

Figure 42: Velocity magnitude [m/s] and velocity vectors at different axial positions.

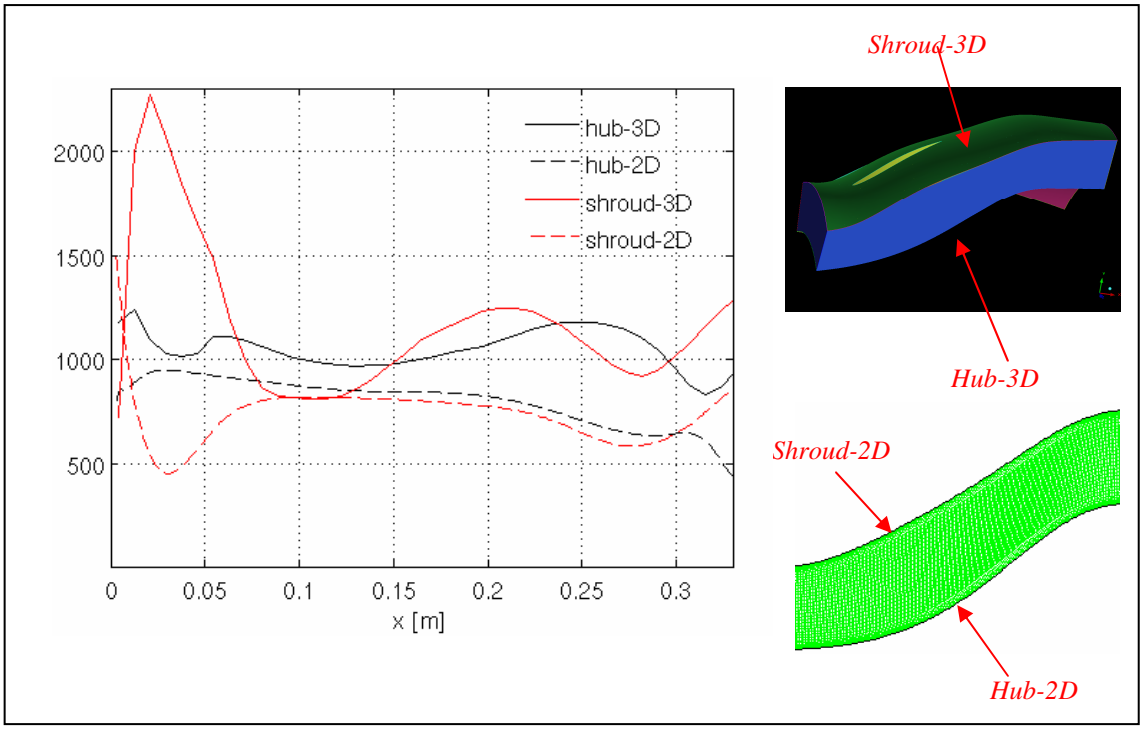

Figure 43: The HTC [W/m^{2}K] for 2D and 3D duct that are averaged in circumferential direction.

$$pressure\ losses = \frac{\Delta P_0}{P_{dyn-inlet}} = \frac{15430[Pa]}{133504[Pa]} \sim 11.56\%$$ Based on inlet dynamic pressure

C2 - Internal cooling- Mesh sensitivity study

The mesh study of the internal cooling configuration is performed in order to check the sensitivity of the used mesh on the obtained solution. The mesh size is however saved a lot using the structured approach. The cooper tool sweeps an unstructured hex-mesh over a desired volume. This gives a qualitative mesh. The mesh study consists of two parts. One that considers fluid flow and the other considers heat transfer. These are then checked both globally and locally. Below is an overview of the mesh study preformed.

1. According to FLUID FLOW
    a. Global consideration – Mass flow at outlets in percentage of inlet mass flow.
    b. Local consideration – Contour plots of velocities in the sectors.

2. According to HEAT TRANSFER
    a. Global consideration
        i. Total surface heat flux (Area average)
        ii. Heated inlets and outlets
        iii. Average bulk temperature at evaluation surfaces
    b. Local consideration – Contour plots of Total surface heat flux at the walls.

The different meshes included in the study are presented below.

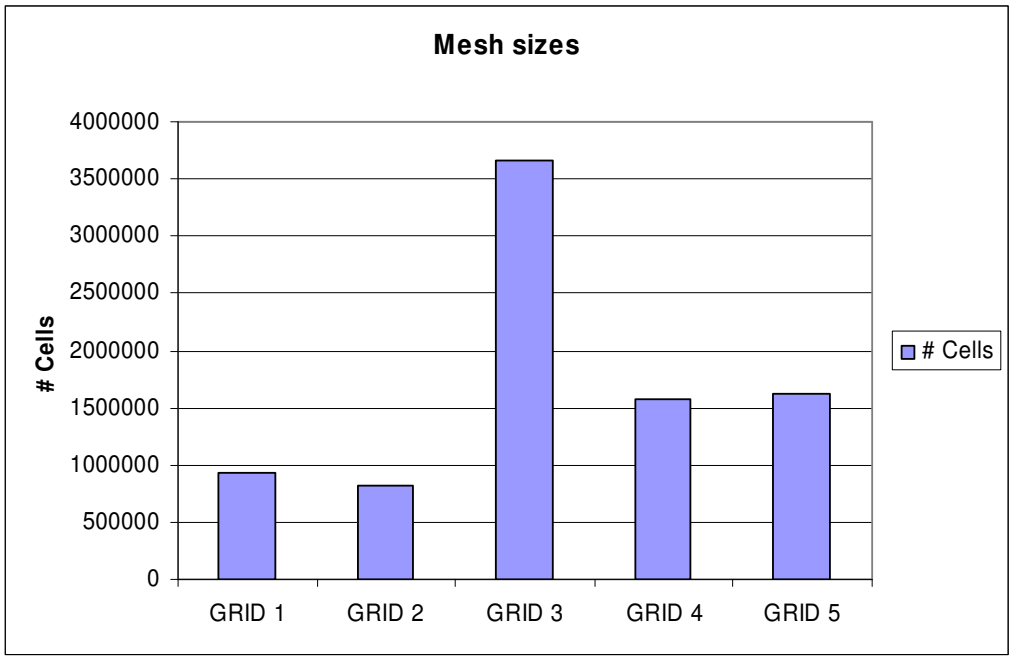

Figure 44: The meshed used and their sizes.

One mesh that is not included above is GRID 6 which is a copy of GRID 5 but have slightly more intensive sizing function on the hub in order to check any wall effects.

Fluid flow

Global consideration

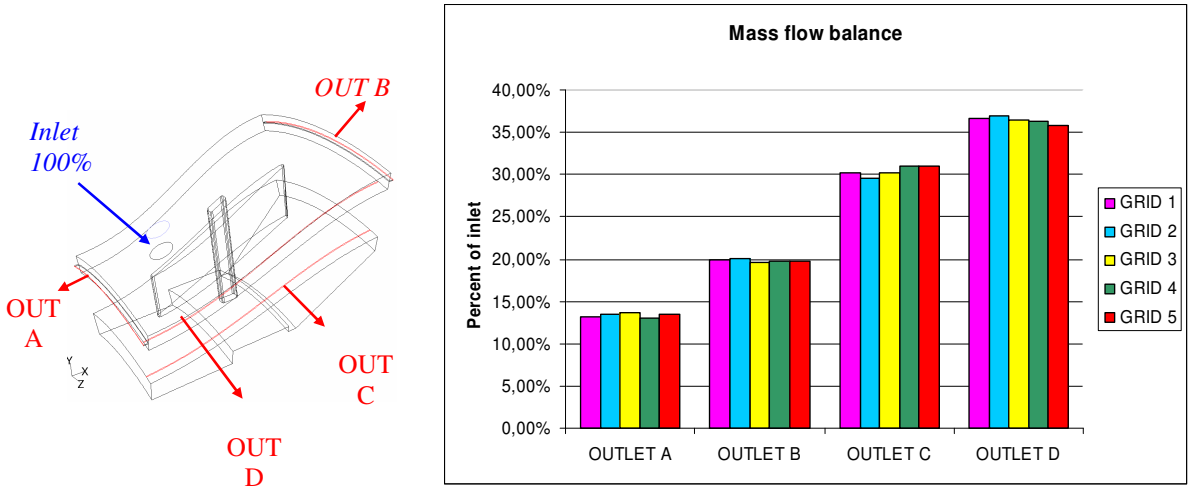

Figure 45: Mass flow at outlets in percentage of inlet mass flow.

The global consideration of fluid flow is grid independent as shown above.

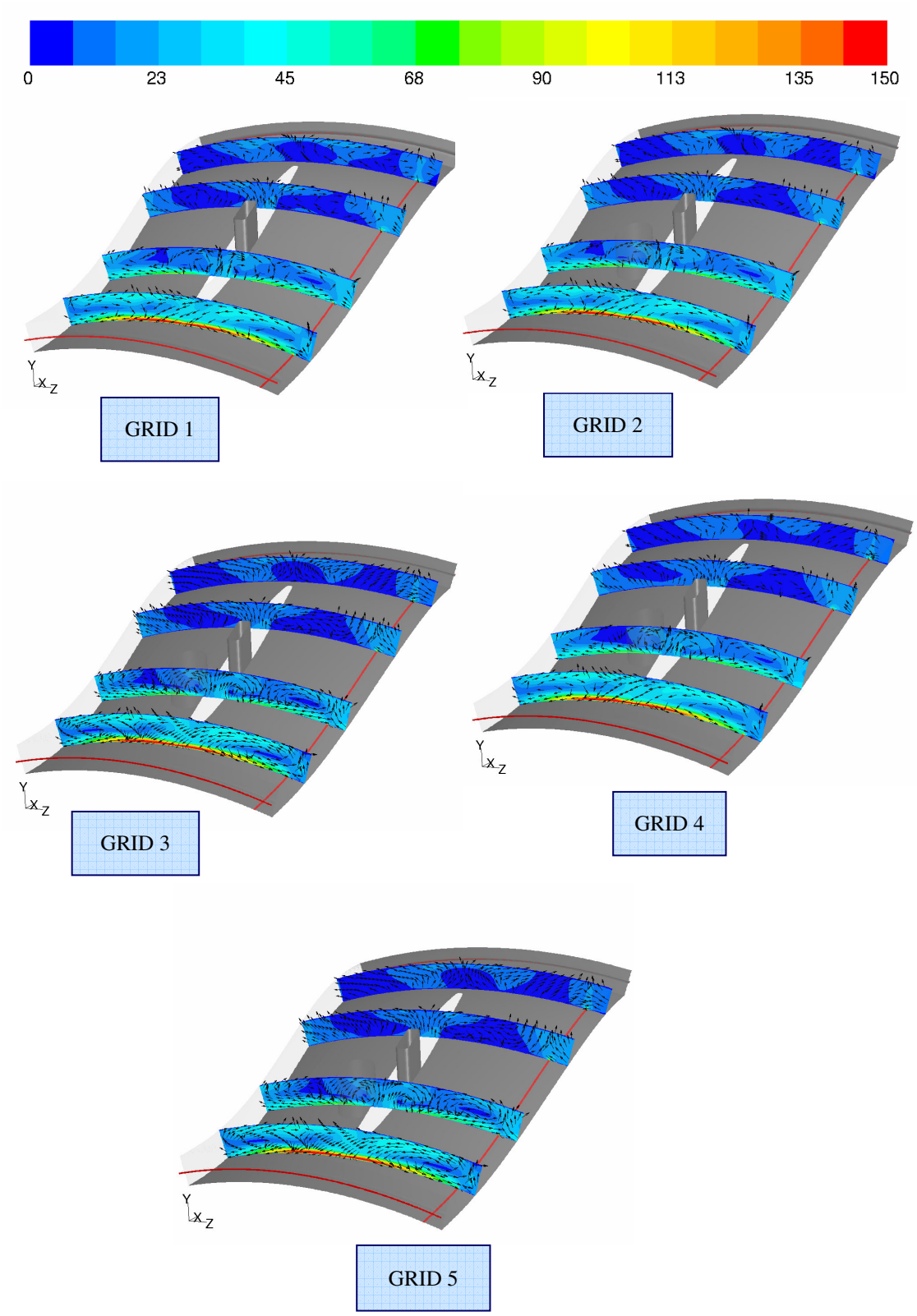

Figure 46: Velocity contours [m/s] at different positions in the outer cavity of the TMS.

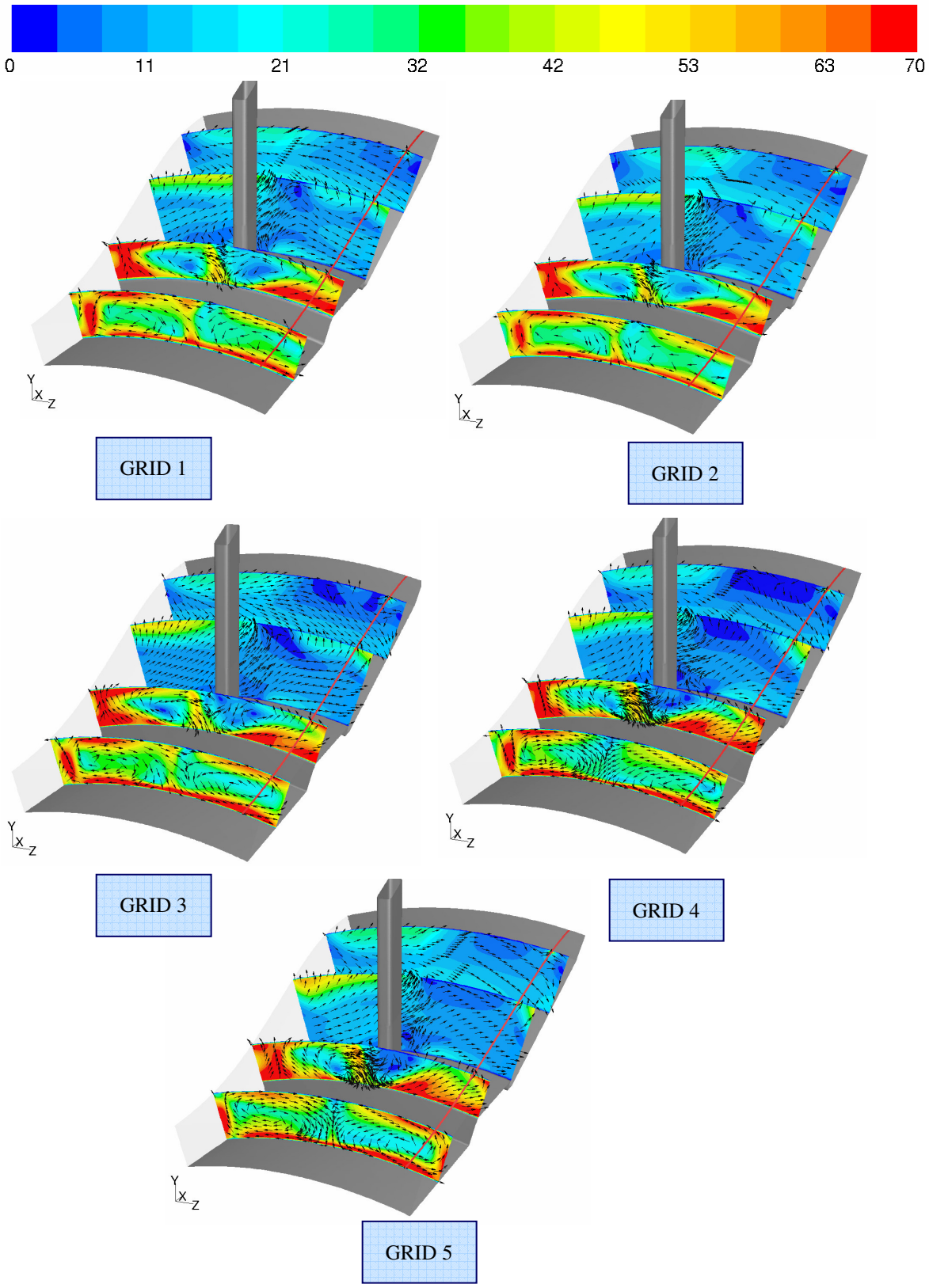

Figure 47: Velocity contours [m/s] at different positions in the inner cavity of the TMS.

Heat transfer

Global consideration

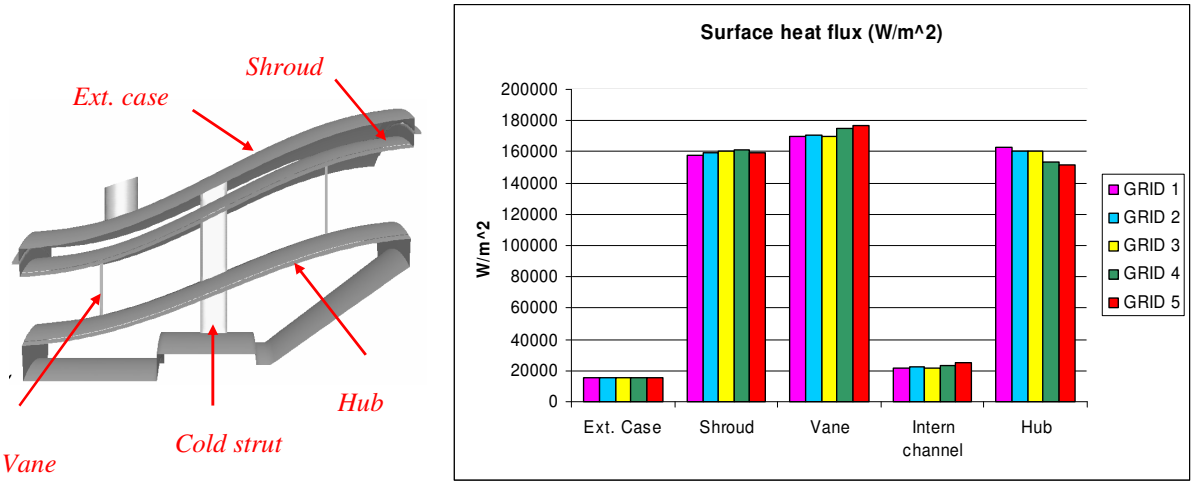

Figure 48: Total surface heat flux (area average).

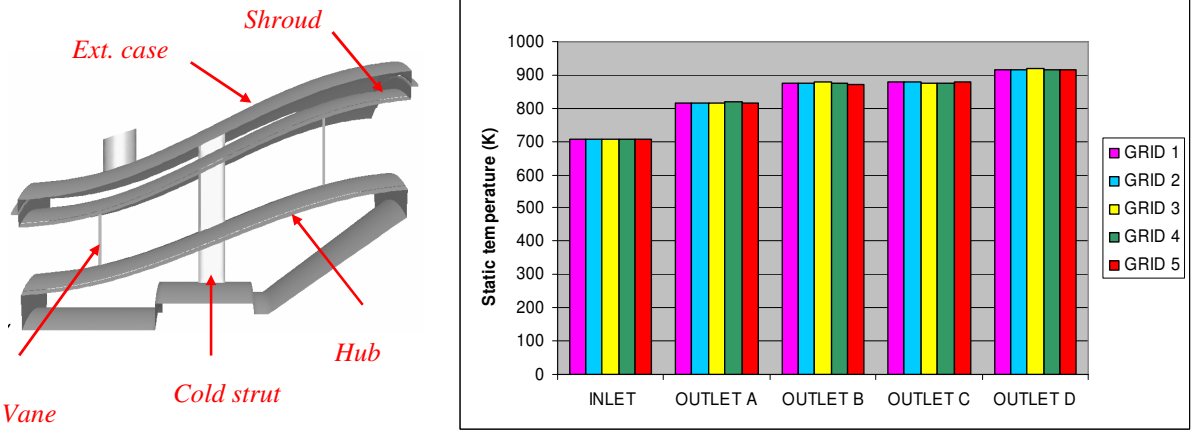

Figure 49: Heated inlet and outlets.

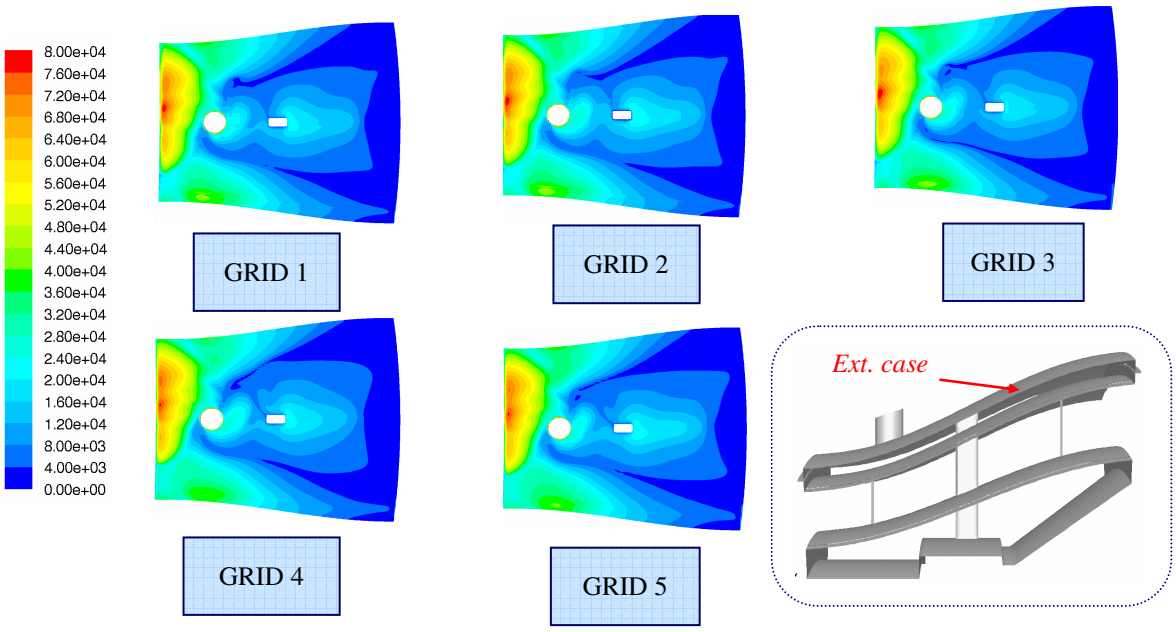

Figure 50: Contour plots of total surface heat flux [W/m^2] at the ext. case.

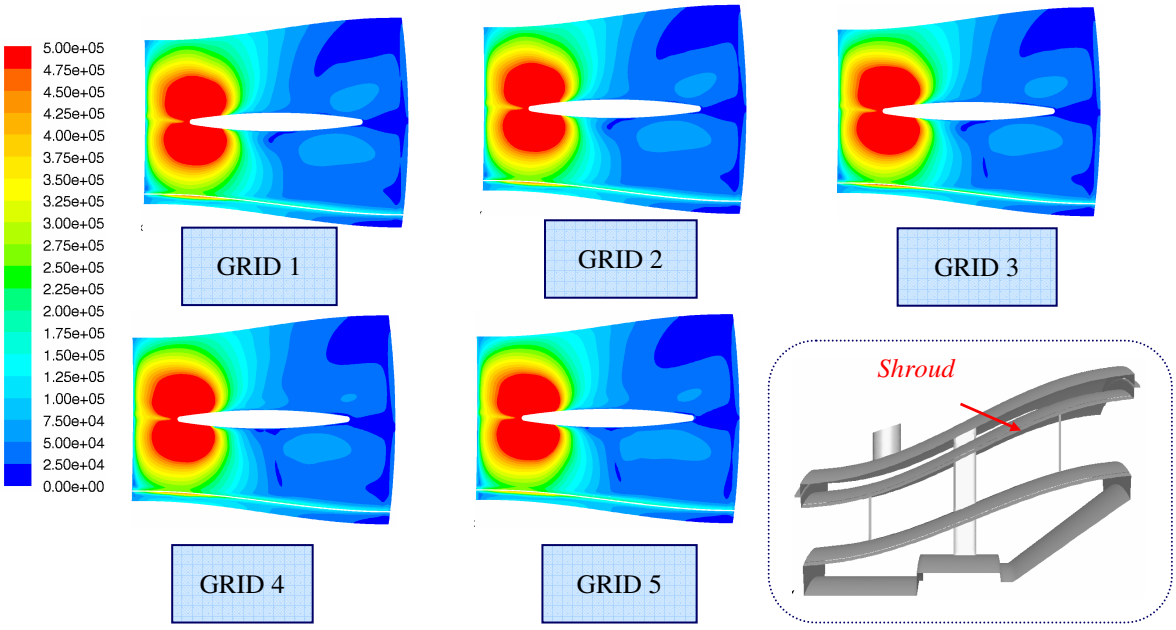

Figure 51: Contour plots of total surface heat flux [W/m^2] at the shroud

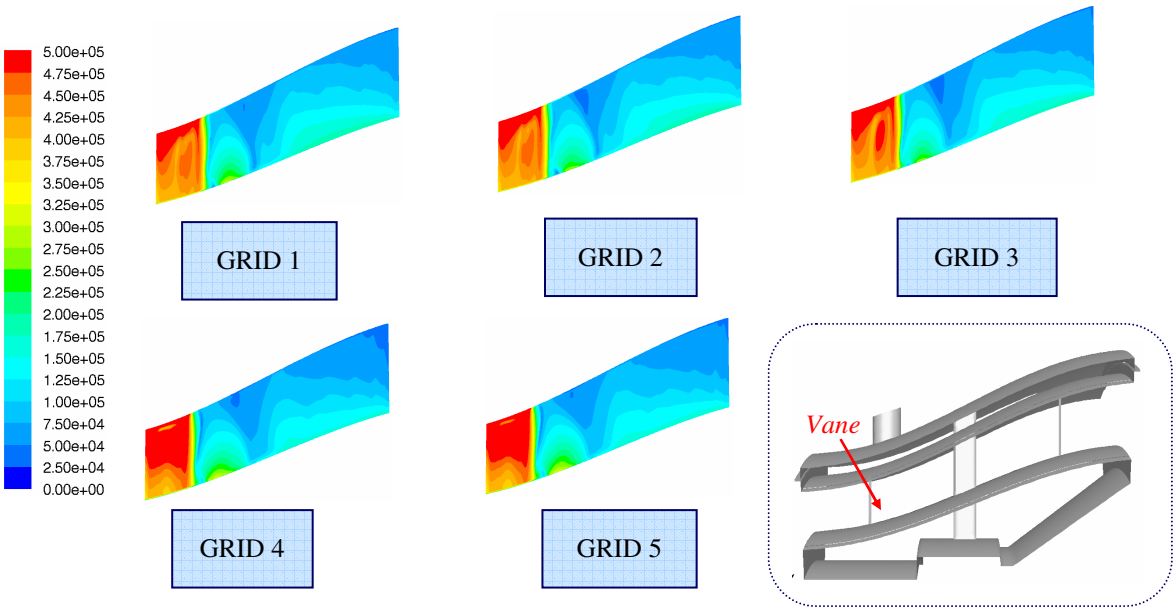

Figure 52: Contour plots of total surface heat flux [W/m^2] at the vane

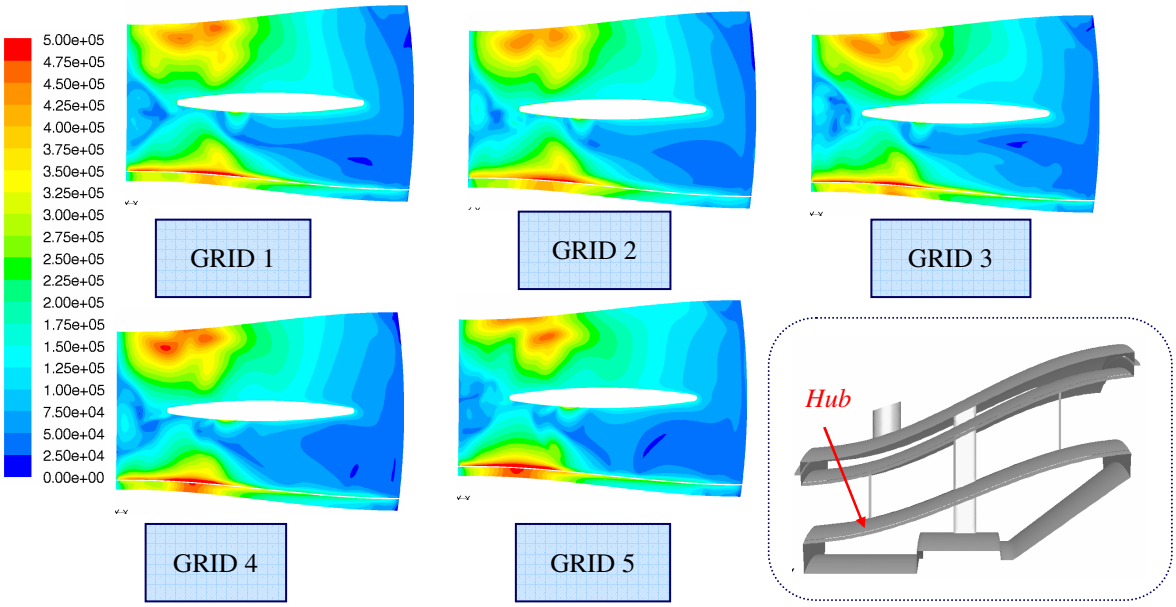

Figure 53: Contour plots of total surface heat flux [W/m^2] at the hub

The check of sizing near a wall is presented below. Wall functions versus enhanced wall treatment and sizing function of 1mm versus 0.5mm

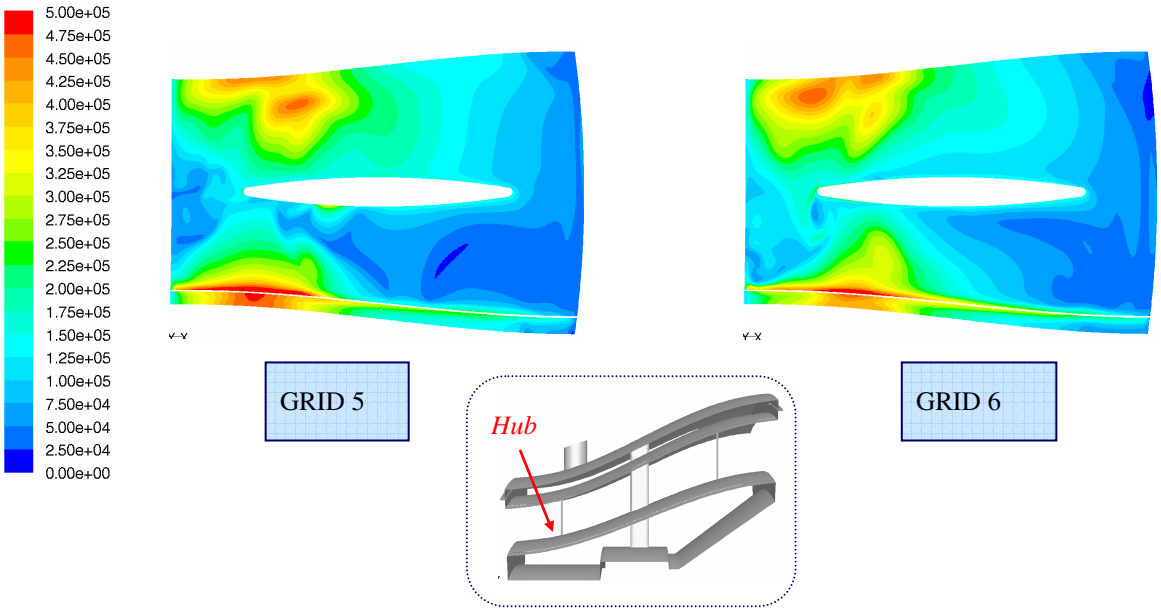

Figure 54: Contour plots of total surface heat flux [W/m^2] at the hub, different sizing func.

C3 - Conjugated model

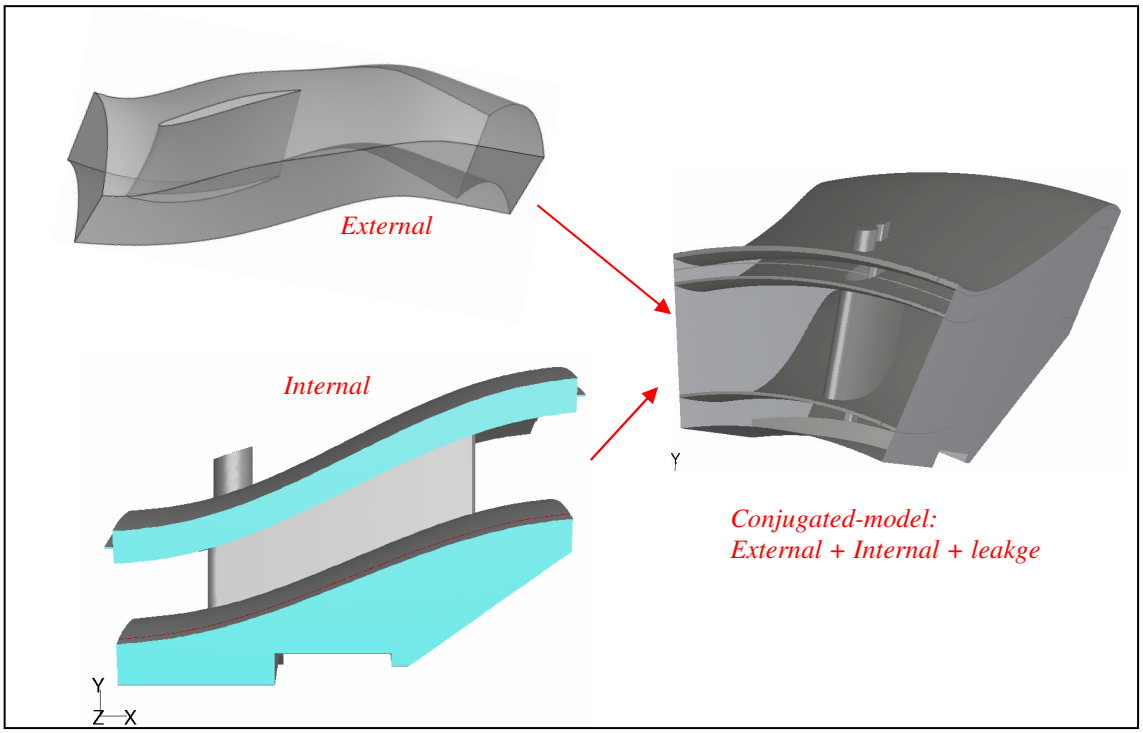

Figure 55: Conjugated model building.

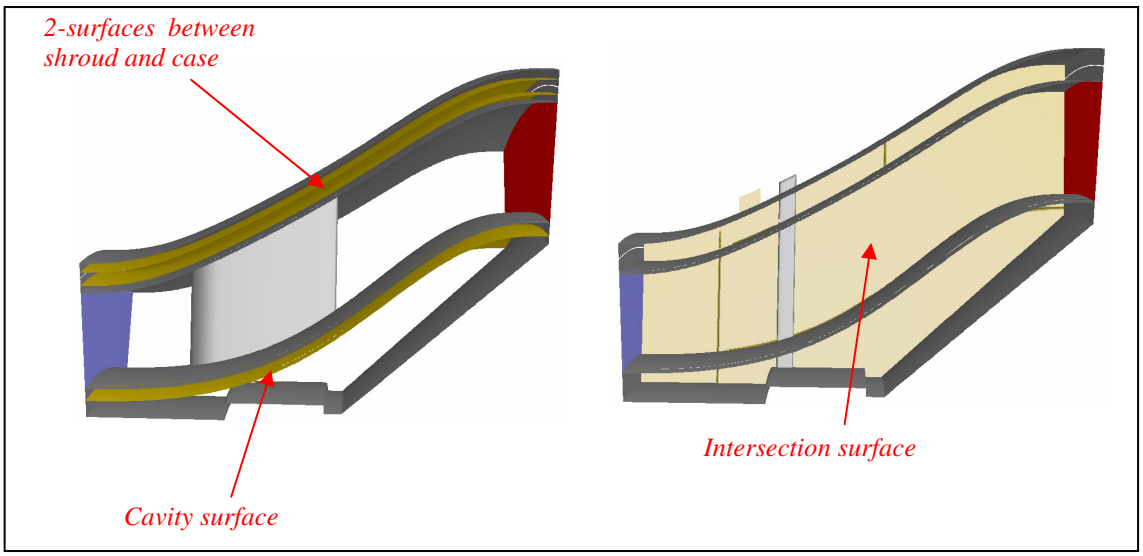

Figure 56: Evaluation surfaces.

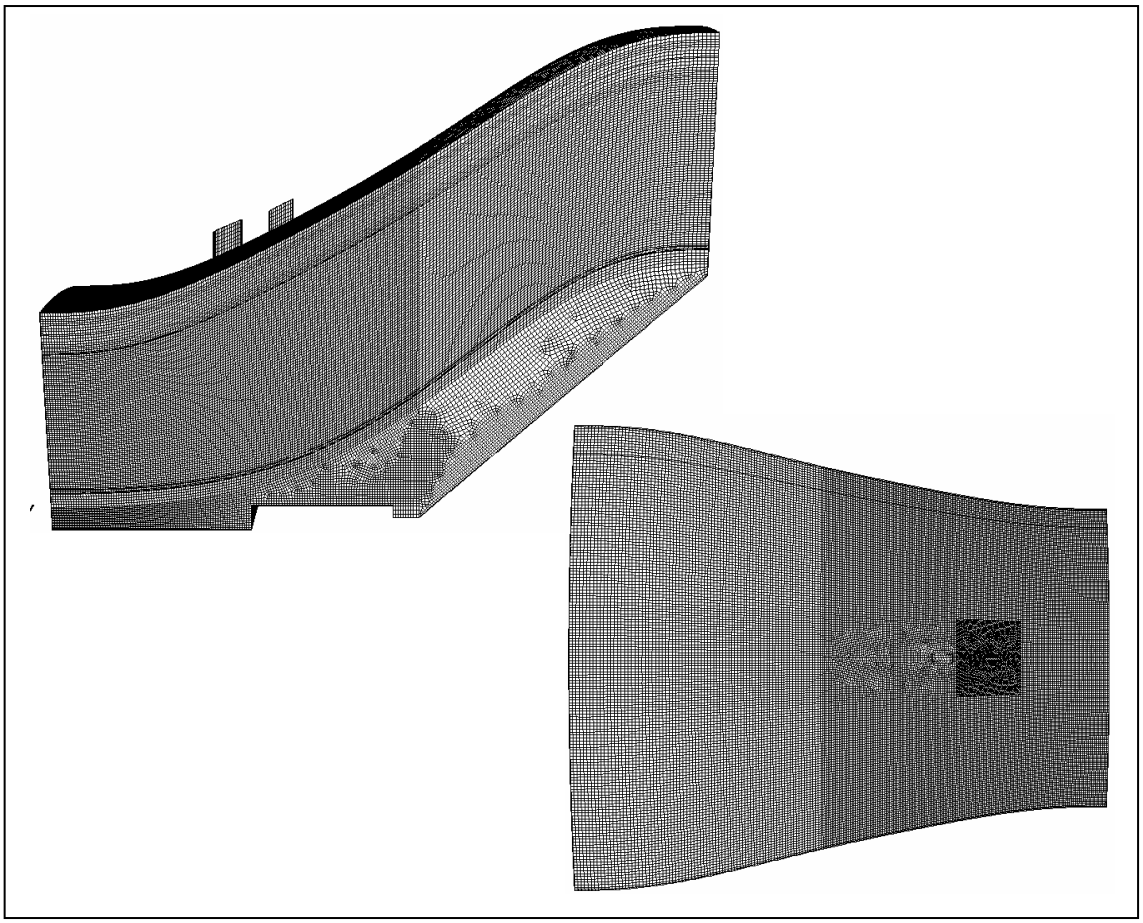

Figure 57: Different views of the mesh.

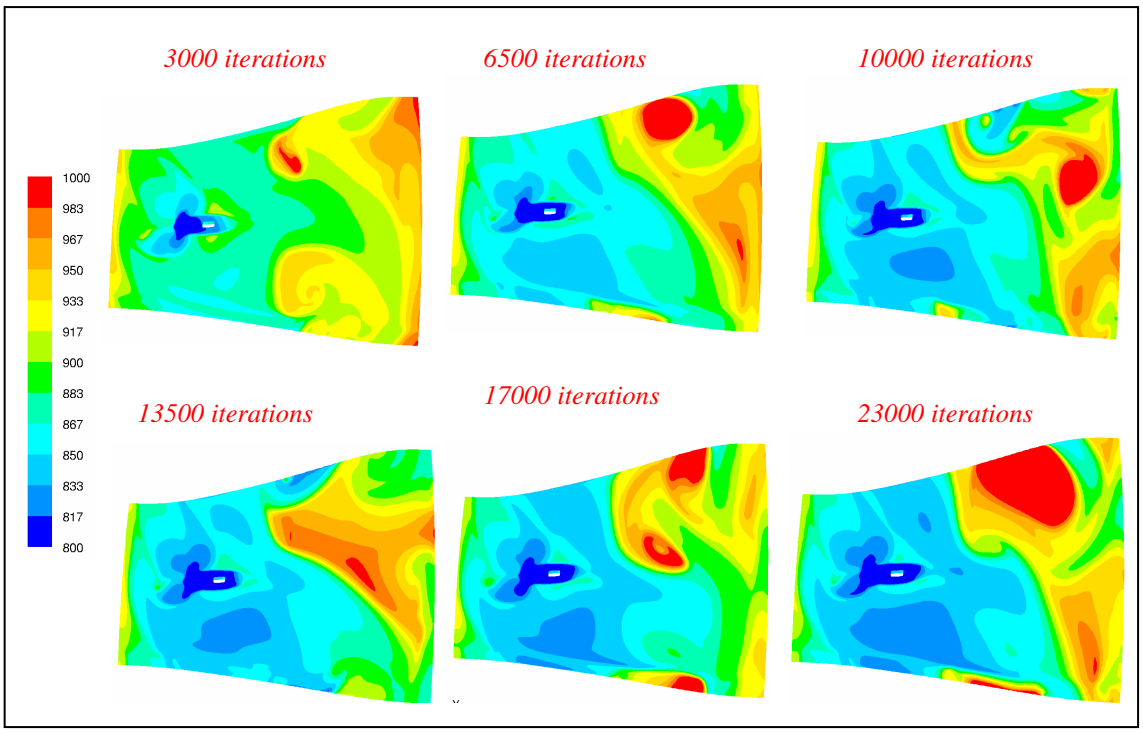

Figure 58: Air temperature [K] above the shroud (evaluation surface) .

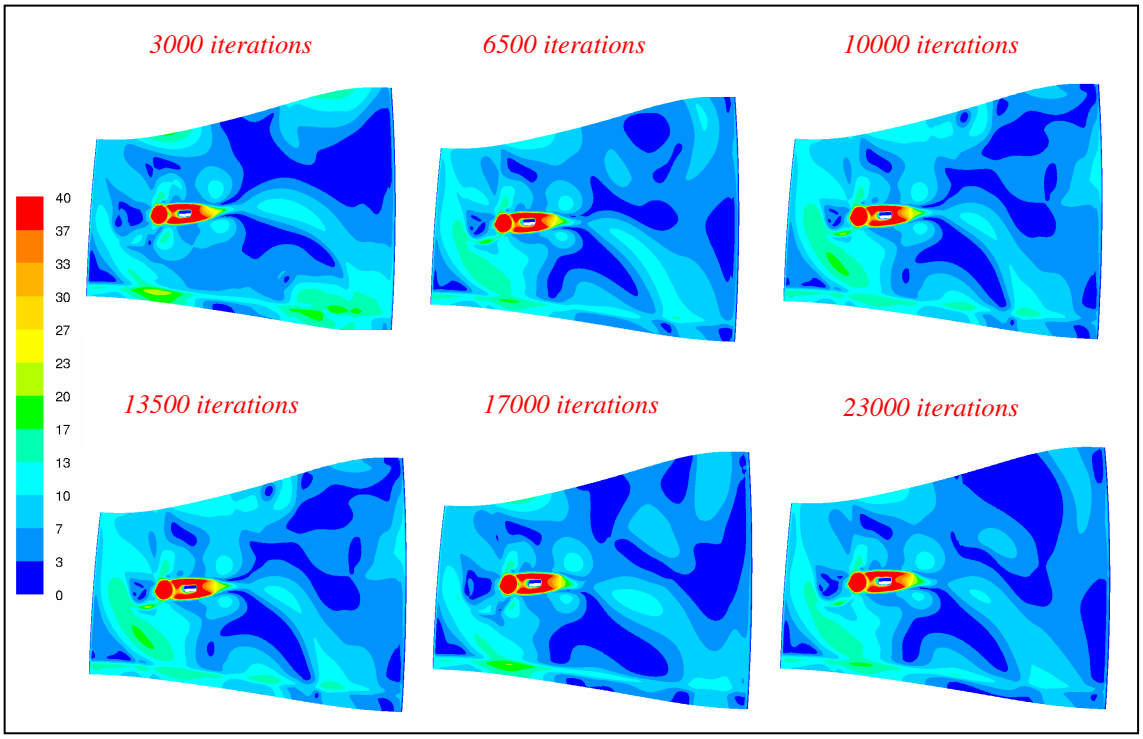

Figure 59: Velocity magnitude [m/s] above the shroud (evaluation surface) .

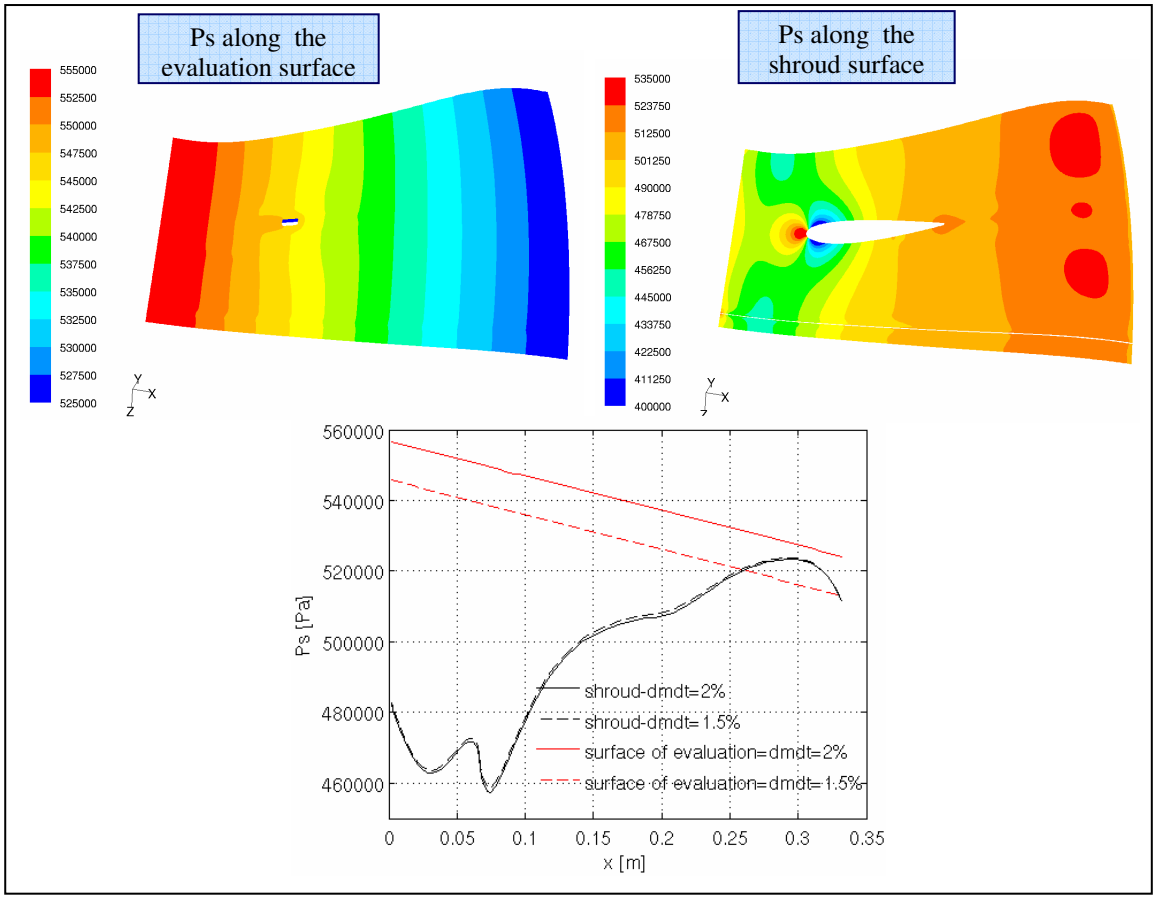

Figure 60: Static pressure [Pa] along the shroud and at the evaluation surface.